Geophysical Evolution of Planetary Interiors and Surfaces: Moon & Mars

by

Alexander Joseph Evans

B.S.E., University of Michigan (2006)

Submitted to the Department of Earth, Atmospheric and Planetary Sciences
in partial fulfillment of the requirements for the degree of

Doctor of Philosophy

at the

MASSACHUSETTS INSTITUTE OF TECHNOLOGY

September 2013

Author .....
Department of Earth, Atmospheric and Planetary Sciences
September 6, 2013

Certified by .....
Maria T. Zuber
E. A. Griswold Professor of Geophysics
Thesis Supervisor

Accepted by .....
Robert D. van der Hilst
Schlumberger Professor of Earth Sciences
Head, Department of Earth, Atmospheric and Planetary Sciences

Geophysical Evolution of Planetary Interiors and Surfaces: Moon & Mars

by

Alexander Joseph Evans

Submitted to the Department of Earth, Atmospheric and Planetary Sciences
on September 6, 2013, in partial fulfillment of the
requirements for the degree of
Doctor of Philosophy

Abstract

The interiors and surfaces of the terrestrial planetary bodies provide us a unique opportunity to gain insight into planetary evolution, particularly in the early stages subsequent to accretion. Both Mars and the Moon are characterized by well-preserved and ancient surfaces, that preserve a record of geological and geophysical processes that have operated both at the surface and in the interior. With accessibility to orbital and landed spacecraft, the Moon and Mars have a unique qualitative and quantitative role in understanding and constraining the evolution of solid planets in our Solar System, as well as the timing of its many major events. In this thesis I use gravity and topography data to investigate aspects of the surface and interior evolution of the Moon and Mars that include aspects of major processes: impact, volcanism, erosion and internal dynamics.

Thesis Supervisor: Maria T. Zuber
Title: E. A. Griswold Professor of Geophysics

Acknowledgments

This dissertation would not have been possible without the continuous support I received from my family, fellow researchers, and friends. I am extremely privileged to have been a part of the Planetary Geodynamics group at MIT. To my adviser, Professor Maria Zuber, I am indebted for her continual guidance throughout my six years of graduate school. I am honored and extremely appreciative for the opportunities that Professor Zuber has extended to me, along with her other advisees, and I am grateful for her unwavering support of our individual goals and aspirations.

It has been a truly humbling experience to work alongside such brilliant and hard-working individuals: Peter James, Mike Sori, Anton Ermakov, ZhenLiang Tian, pilot Frank Centinello, and Yodit Tewelde. I am especially appreciative for the friendship and mentorship of my fellow group mates who graduated before me: Dr. Erwan Mazarico, Dr. Ian Garrick-Bethell, Dr. Wes Watters, and Dr. Sarah Stewart-Johnson.

Also, I am incredibly thankful for my many friends, who without them, I would not have been able to maintain stability in aspects of my life outside of graduate school. I owe special thanks to my friend, Dr. Julia Mortyakova for her guidance and emotional support. I could not imagine going through my graduate experience without the support and friendship of Dakotta Alex, Brianna Ballard, Jeff Parker, Owen Westbrook, Dr. Anita Ganesan, Dr. Jon Woodruff, Dr. Oaz Nir, Dr. Kevin McComber, Alejandra Quintanilla Terminel, Ruel Jerry, Dr. Diane Ivy, Dr. Laura Meredith, Sonia Tikoo, Gabi Melo, Marie Giron, and Sharon Newman.

I would especially like to thank Dr. Jeffrey Andrews-Hanna and Dr. Jason Soderblom for their insightful discussions and guidance that helped me grow as a scientist and their indulgence in my numerous and prolonged unscheduled visits to their office to discuss my research. I also owe my deepest gratitude to Roberta Allard, Margaret Lankow, and Will Hodkinson for the many favors and their great problem-solving abilities. Of course, the opportunities that I have been afforded at MIT would not have been possible without the financial support from MIT and NASA funding sources.

Without qualification, I would like to thank my long-time friends Brian Kitchen and Dr. Crystal Thrall; I owe you a great many thanks for providing a safe place to complain and a haven in my spontaneous, yet therapeutic sabbaticals from Boston.

Finally, I would to thank my thesis committee Professors Jeffrey Andrews-Hanna, Tanja Bosak, Timothy Grove, Taylor Perron, and Maria Zuber for their time, dedication, advice, and support.

Contents

List of Figures

List of Tables

Chapter 1

Introduction

For most of history, humans gazed upward to the great unknown and wondered what mysteries lie beyond. Over four centuries ago, pioneers of the scientific revolution such as Galileo Galilei and Sir Isaac Newton embarked on the arduous task of unraveling the mysteries of the Universe. Now, over 400 years later, with spacecraft, new technologies, and the capability to send humans into space, the arduous task of unraveling the mysteries of the Universe continues. In this thesis, I examine a few of the many current mysteries and attempt to provide a unique perspective on unanswered questions within the inner Solar System.

Starting with the ancient terrain of Arabia Terra region of Mars, an area of $\sim 1 \times 10^7$ km^2 lying south of the hemispheric dichotomy boundary, I use altimetry data returned by the Mars Orbiter Laser Altimeter (MOLA) on the Mars Global Surveyor (MGS) along with gravity data from the Mars Reconnaissance Orbiter (MRO) to constrain the volume of material removed by aqueous and aeolian processes. Constraining material removed from this unique physiographic province, which possesses topography and crustal thickness intermediate between those of the southern highlands and northern lowlands, will provide insight into the formation of the Martian hemispheric topographic and crustal dichotomy. I employ a multi-taper, spatio-spectral localization approach to gravity-topography admittance estimates and find a best-fit elastic thickness estimate that may be used to constrain surface

loading in the region. I find the elevation difference between Arabia Terra and the southern highlands would require up to 25-km erosion in order to reproduce the elevation and crustal thickness deficit of Arabia Terra. Such a large amount of erosion would result in exterior flexural uplift surpassing 1 km and gravity anomalies exceeding observations by $\sim$60 mGal. Consequently, it is unlikely that Arabia Terra was formed from surface erosion alone. I determine that no more than 3×10^7 km^3 of material could have been removed from Arabia Terra, while 1.7×10^8 km^3 of erosion is required to explain the observed crustal thickness.

Given the canonical model of lunar formation from a giant impact of a Mars-sized body with the Earth, understanding the evolution of the Moon has direct consequences for Earth. Recent re-analyses of Apollo-era lunar samples indicate the Moon contained regions with water concentrations of at least 260 ppm in the deep lunar interior prior to 3 billion years ago and the Moon had a convective core dynamo from at least 4.2-3.56 billion years ago (Gya). Past investigations of lunar convective dynamos with a generally homogeneous and relatively dry Moon have been unable to yield adequate heat flux at the core-mantle boundary to sustain core convection for such a long time. Using a finite-element model, I investigate the possible consequences of a heterogeneously wet and compositionally stratified lunar interior for the evolution of the lunar mantle. I find that a compositionally-stratified mantle could result in a core heat flux sufficiently high to sustain a dynamo through 2.4 Ga and a maximum surface magnetic field strength of 5.1μT. Further, I find that if water was transported or retained preferentially in the deep interior, even in small amounts ($\leq$20 ppm), it would have played a significant role in transporting heat out of the deep interior and reducing the lower mantle temperature. Thus, water, if enriched in the lower mantle, could have influenced core dynamo timing by up to 1.0 billion years (Gyr) and enhanced the vigor of a lunar core dynamo. My results demonstrate the plausibility of a convective lunar core dynamo even beyond the period currently indicated by the Apollo samples. Near the surface, a water-enriched region of the Moon that retains a non-negligible portion of radioactive material at the base of the crust could diminish the surface expression of impact basins in excess of 30% via viscoelastic relaxation. Without a near-surface radioactive material layer, water alone may have caused non-negligible relaxation of surface features

older than 4.1 Gya.

With newly acquired data by the dual Gravity Recovery and Interior Laboratory (GRAIL) spacecraft, I find over 100 quasi-circular mass anomalies on the lava-flooded region of the Moon. As impact craters are the most ubiquitous circular features on the Moon, I interpret these mass anomalies as gravity signatures of buried impact craters. I use this buried crater population to investigate the thickness, volume, and density of cooled lava (basalt) emplaced on the lunar nearside. My analyses suggest that nearside lunar basalts have a density contrast of 800 kg/m^3 relative to the lunar crust and at least 2×10^7 km^3 of basalt was emplaced on the lunar surface. The existence of such a large quantity of buried craters indicates that there is a heterogeneous distribution of lunar basalt across the lunar nearside, with craters and rims requiring burial by more than 5 km of basalt. In concert with 80 anomalously shallow lunar nearside craters, I find the lunar maria may have a density contrast of 800 kg/m^3 with the anorthositic highlands crust, indicating an average density of lunar maria 3300$\pm$200 kg/m^3.

With this thesis, I hereby contribute the results of my investigations to the body of knowledge for the formation and evolution of our Solar System and the Universe.

Chapter 2

Geophysical Limitations on the Erosion History within Arabia Terra

This chapter has been published and can be referenced as: *Evans, A. J., Andrews-Hanna, J. C., & Zuber, M. T. (2010). Geophysical limitations on the erosion history within Arabia Terra. Journal of Geophysical Research-Planets, 115(E5). doi:10.1029/2009JE003469.*
 0148-0227/10/2009JE003469.

2.1 Introduction

Arabia Terra, with an area of 1×10^7 km^2 centered at (25E, 5N), is an anomalous region along the Martian dichotomy boundary. Traditionally considered part of the ancient southern highlands (e.g., (2; 3; 4; 5)), Arabia Terra provides a more gradual transition from the southern highlands to the northern lowlands in both topography (6; 7) and crustal thickness (8; 9). While the geological processes leading to the formation of the region have not been clearly identified (e.g., (10)), Arabia Terra contains morphological evidence indicative of surface erosion including isolated mesas (11; 12) and partially degraded craters (13). Though surface modification has been suggested for the entirety of the highlands (e.g., (14)), the anomalous nature of Arabia Terra and its geomorphology may indicate preferen-

tial erosion of the region. The amount of erosion may have generated a significant volume of sediment, possibly contributing to the resurfacing of the northern lowlands.

Though previous workers have attempted to constrain the amount of erosion for Arabia Terra and the southern highlands in general, much of the analyses have been based on crater degradation with anywhere between 200 m to 2300 m of material being eroded, as put forth by (14). (11) approached the problem from an alternative geomorphic perspective: using the height of local elevation maxima (isolated mesas) in concert with the mapping of geological units. Their analysis indicates that a minimum of 1000 m of material was removed from the Arabia Terra region in the late Noachian. Recent analysis of data from the Mars Exploration Rover landing site at Meridiani Planum within Arabia Terra suggests smaller amounts of erosion have occurred since $\sim$3.0 Ga, though evidence for this erosion is found on sedimentary deposits that lie above the original surface and thus does not constitute net loss (15). It has generally been suggested that erosion during the Noachian and early-mid Hesperian may have been greater due to a warmer and wetter environment (14; 15). Widespread layered deposits across the region suggest an early period of deposition as well (16; 17).

Prior analyses of erosion in Arabia Terra (e.g., (11)) relied on the geomorphology of the terrain and craters. In this paper, we present our constraints for the erosion of Arabia Terra based on geodynamical modeling coupled with limitations established from topography and gravity data returned by the Mar Orbiter Laser Altimeter (MOLA) (18; 6) on the Mars Global Surveyor (MGS) (19) and the gravity field investigation on the Mars Reconnaissance Orbiter (MRO) (20), respectively. By comparing the expected flexural response and gravitational signature (21) of various erosional loads to the observational data, we establish an upper limit on the amount of material that could have been removed from within Arabia Terra. We employ a lithospheric flexure model to attain the flexural rebound and gravitational signature associated with a given erosional load. Exploiting recent advances in spherical harmonic localization techniques (22; 23), we better constrain the elastic lithosphere thickness (24) – a crucial parameter in resolving the flexural response to erosion. Our flexure model, based upon the thin elastic shell method of (21), estimates the mem-

brane and bending stresses for a load supported by an elastic lithosphere underlain by a fluid-like medium. We test the viability of several erosional scenarios, including loads capable of reproducing the unique topography and crustal structure of Arabia Terra from an initial, highlands-like terrain.

2.2 Methodology

2.2.1 Spherical Harmonic Localization

Any square-integrable function defined on a spherical surface, $f(\Omega)$, can be expanded as a linear combination of spherical harmonics (25) by

$$f(\Omega) = \sum_{l=0}^{\infty} \sum_{m=-l}^{l} f_{lm} Y_{lm}(\Omega), \tag{2.1}$$

and

$$f_{lm} = \int_{\Omega} f(\Omega) Y_{lm}(\Omega) d\Omega, \tag{2.2}$$

where Ω is the solid angle, Y_{lm} is the spherical harmonic basis function of degree l and order m, and f_{lm} are the corresponding spherical harmonic coefficients.

We apply a method for spatio-spectral localization on a sphere, in which data is localized to an arbitrarily-shaped region of interest by applying a family of orthogonal spherical harmonic tapers (26; 22). Ultimately, we apply this localized spectral analysis within Arabia Terra to attain the regional elastic thickness at the time of formation. To spatially concentrate a band-limited function, $f(\Omega)$, within an arbitrarily-shaped region, R, we maximize the energy concentration, λ, according to

$$\lambda = \frac{\int_R f(\Omega)^2 d\Omega}{\int_{\Omega} f(\Omega)^2 d\Omega} = \text{maximum}, \tag{2.3}$$

within the region, R, where $0 \leq \lambda \leq 1$. By use of Eq. (5.2), we can rewrite (5.3) as

$$\lambda = \frac{\sum_{l=0}^{L_{win}} \sum_{m=-l}^{l} f_{lm} \sum_{l'=0}^{L_{win}} \sum_{m'=-l'}^{l'} D_{lm,l'm'} f_{l'm'}}{\sum_{l=0}^{L_{win}} \sum_{m=-l}^{l} f_{lm}^2}, \tag{2.4}$$

where

$$D_{lm,l'm'} = \int_R Y_{lm}(\Omega) Y_{l'm'}(\Omega)\, \mathrm{d}\Omega, \tag{2.5}$$

and L_{win} is the bandwidth of the localization (window). Each degree, l, receives contributions from across the range $l - L_{win} \leq l \leq l + L_{win}$. Hence, our choice for the window bandwidth restricts the resulting localization, such that the following inequality holds for all degrees, l_{loc}, of the windowed field, $L_{win} \leq l_{loc} \leq L_{obs} - L_{win}$, where L_{obs} is the maximum expansion degree of the data set being considered.

As shown by (22), Equation (5.4) reduces to a matrix eigenvalue equation where the eigenfunctions of a kernel given by $D_{lm,l'm'}$ are spherical harmonic coefficients of the space concentrated tapers (e.g., (23). The result of this reduction in full index notation is,

$$\sum_{l'=0}^{L_{win}} \sum_{m'=-l'}^{l'} D_{lm,l'm'} f_{l'm'} = \lambda f_{lm}. \tag{2.6}$$

The number of eigenfunctions optimally-concentrated within the region of interest can be obtained by calculating the Shannon number, N,

$$N = \sum_{n=1}^{(L_{win}+1)^2} \lambda_n = (L_{win}+1)^2 \frac{Area}{4\pi}. \tag{2.7}$$

We use the N optimally-concentrated eigenfunctions to localize the region, similar to the method prescribed by (23).

2.2.2 Loading Model

Thin Elastic Shell Adaptation

In order to represent the effects of erosion in Arabia Terra, we account for the resultant flexure and gravity signature of the erosional load. We establish limits on the extent of regional erosion by analyzing these resultant signatures and comparing to observational data.

We employ an adapted version (27) of the thin elastic lithosphere (shell) model outlined by (21). Following (21), we introduce the dimensionless parameters,

$$\tau = \frac{ET_e}{R^2 g \Delta\rho}, \tag{2.8}$$

and

$$\sigma = \frac{D}{R^4 g \Delta\rho}, \tag{2.9}$$

where E is Young's modulus, T_e is the elastic lithosphere thickness at the time of loading, R is the mean radius of the shell, g is the Martian gravitational acceleration, and $\Delta\rho$ is the density contrast between continua below and above the shell. The mean shell radius, R, and flexural rigidity, D, can be represented as $R = R_p - T_e/2$ and $D = ET_e^3/12(1-\nu^2)$, where ν is Poisson's ratio and R_p is the equatorial planetary radius. The independent parameters that we use for the loading model are listed in Table 2.1.

We use spherical harmonic representations of the load thickness h, the resulting deflection w, and the equipotentially-referenced, final topography $\widehat{h}$. Relating the load thickness and flexure in the spectral domain yields the relationship,

$$w_{lm} = -\frac{\rho_L}{\Delta\rho}\alpha_l h_{lm}, \tag{2.10}$$

where ρ_L is the load (crustal) density and the transfer function,

$$\alpha_l = \left[1 - \frac{3\rho_m}{(2l+1)\overline{\rho}}\right]\left[\frac{1}{\zeta_l} - \frac{3\rho_m}{(2l+1)\overline{\rho}}\right]^{-1}, \tag{2.11}$$

with $\overline{\rho}$ as the mean Martian density and

$$\zeta_l = \frac{-[l(l+1)-(1-\nu)]}{\sigma[-l^3(l+1)^3+4l^2(l+1)^2-4l(l+1)]+\tau[-l(l+1)+2]+[-l(l+1)+(1-\nu)]}. \tag{2.12}$$

This formalism allows us to solve for a final topography where $\widehat{h} = h + w$; additionally, an analogous relation to Equation 2.10 for the final topography and flexure may be used to explicitly solve for the associated erosional load (i.e. Equation 21 of (21)).

Geoid Solution

We define a spherical harmonic representation of topography, H, similar to (24), as

$$H(\Omega) = \hat{S}(\Omega) - A(\Omega), \tag{2.13}$$

where $\hat{S}$ is the planetary shape and A is the Martian reference geoid. We choose the mean planetary radius, 3389.5 km (7) as the first term of a spherical harmonic expansion of the radius similar to (28) and approximate the deviation of the geoid from the mean planetary radius as,

$$A(\Omega) = 0.95\hat{S}_{2,0}. \tag{2.14}$$

For our erosional model, a degree-1 term is included in Eq. (2.14) to account for the center-of-mass offset resulting from the erosional load. Referencing the topography with respect to the geopotential accounts for the self-gravitation of (21) (e.g., (24)), allowing us to apply the gravity calculation demonstrated by (29). Throughout our computational analysis, we consider both the shape and the topography to ensure an accurate representation of the resulting flexure and gravity field.

Gravity Solution

We calculate the gravity anomaly resulting from the erosional load and flexural deformation using the finite amplitude formulation of (29). The gravity anomaly can be expressed as,

$$\Delta g = \frac{GM}{r^2}\left(\frac{R_p}{r}\right)^l (C_{lm}^{surf} + C_{lm}^{moho})Y_{lm}, \tag{2.15}$$

where C_{lm}^{surf} and C_{lm}^{moho} represent the topography along the surface and base of the crust, respectively. However, we slightly modify the solution, as described by (24) for C_{lm},

$$C_{lm} = \frac{4\pi\Delta\hat{\rho}r^3}{M(2l+1)}\sum_{n=1}^{l+3}\frac{{}^n\hat{S}_{lm}}{r^n n!}\frac{\prod_{j=1}^{n}(l+4-j)}{(l+3)}, \tag{2.16}$$

where r is the reference radius of the Martian geoid along the density interface, ${}^n\hat{S}_{lm}$ is the spherical harmonic representation of the planetary shape along the interface raised to the nth power, and $\Delta\hat{\rho}$ is the change in density across the interface. The first term in the above expansion represents a first-order (mass-sheet) approximation of the gravity anomaly by representing the mass variations due to topography along the surface and crust-mantle as an infinitesimally thin sheet. The higher order terms take into account the effect of the finite amplitude relief along two-dimensional density interfaces. Though the first-order treatment is generally adequate, for cases of large or varying relief along a density interface, the mass distribution with depth becomes increasingly important and is accounted for by the summation of terms beyond $n = 1$. In our calculation, we consider only the first six terms of the above summation. For the surface, $r = R_p$ and $\Delta\hat{\rho} = \rho_L$, whereas $r = R_p - T_{crust}$ and $\Delta\hat{\rho} = \rho_m - \rho_L$ along the crust-mantle boundary. Here, T_{crust} represents the mean crustal thickness. We list parameter values for each interface in Table 2.2.

2.3 Erosional Constraints within Arabia Terra

Using altimetry data returned by the MOLA (18; 6) on MGS (19) along with gravity data from MRO (20), we place geophysical constraints on the maximum amount of erosion for Arabia Terra. We analyze the topography (7) and gravity (30) in a 1^o resolution grid in the spatial domain. Unless otherwise noted, we expand our data fields to $l = 75$. We define and restrict our investigation of Arabia Terra to the region outlined by Figure 2-1(a). Here, we examine the unique structure of Arabia Terra and key evidence interpreted as erosional indicators.

2.3.1 Terrain and Crustal Thickness

The elevation (6; 7) and crustal thickness (8; 9) profiles within Arabia Terra decrease gradually to the north, in between more discrete transitions at the northern and southern boundaries of the province (31). The topography decreases by $\sim$5 km over a distance of 2500 km across Arabia Terra (Figure 2-1(b)), while the crustal thickness decreases by $\sim$25 km. Unlike other areas along the Martian dichotomy boundary, Arabia Terra is afforded a more gentle transition from the highlands to the northern lowlands in elevation and crustal thickness as shown in Figure 2-2(a) (6; 7). Though the region possesses topography and crustal thickness that are arguably more similar to the northern lowlands (8), recent analysis by (31) reveals the northern edge of Arabia Terra is continuous with the crustal dichotomy boundary, suggesting that Arabia Terra is, in a physiographic sense, part of the highlands.

Arabia Terra contains many inliers (local elevation maxima) and isolated mesas (fretted terrain) that have been interpreted as evidence for a prior, more elevated surface (e.g., (11; 32). In order to gauge the minimal amount of eroded material, (11) use the local elevation maxima to establish a lower bound on regional erosion. (11) restricted their investigation to western Arabia Terra and Margaritifer Sinus and estimated a minimum of 4.5×10^6 km^3 of eroded material. If distributed across Arabia Terra, this total amount of erosion is equivalent to a uniform erosional load of 450 m.

As a result of the prominence of partially degraded craters (14), infilled craters (33) and ancient valley networks (34), surface modification processes, namely erosion and deposition, have been proposed to have acted across the whole of the highlands (35; 14). While partially degraded craters are inherent to Arabia Terra as part of the highlands, Arabia Terra lacks a widespread presence of the ancient valley networks characteristic of highlands terrain (36). The absence of the valley networks and an apparent deficit in the large surface crater population (35), both of which are physiographic indicators of the southern highlands, have been interpreted as increased activity of erosion and deposition within Arabia Terra in early Martian history (11). The abundant geomorphologic evidence indicates a complex, yet ambiguous erosional history (33; 35; 14; 15). Given that it is difficult to place firm constraints on the net volume of material eroded and removed from a geomorphic perspective, we focus on the geodynamic response to evaluate the maximum volume of eroded material that is consistent with the gravity and topography.

2.3.2 Gravity

Notwithstanding the geomorphic evidence for surface erosion, gravity anomalies indicative of massive denudation are not readily observed and may be attributed to the regional dominance of Tharsis' antipodal bulge (36). By virtue of its long-wavelength nature, we can approximate this Arabia bulge by incorporating a degree-1 offset into our gravity anomaly as shown in Figure 2-2(c). Though we acknowledge this approximation is insufficient to remove the entirety of the gravitational signature associated with the Tharsis rise and its flexural response, this correction more satisfactorily removes the Tharsis-induced gravity anomalies in Arabia Terra than does the application of high-pass filters.

With the Arabia bulge correction, we can evaluate the viability of different erosional scenarios by comparing the modeled and observed gravity anomalies. Unless explicitly stated, we assume Arabia Terra was initially devoid of any gravity anomaly differences across its boundaries beyond the isostatic signature associated with the Martian dichotomy boundary. We expect the gravitational signature resulting from erosion interior to Arabia Terra to be

observable as a change across the northern and southern provincial boundaries. We define this gravity anomaly difference between the exterior and interior of Arabia Terra as the *relative gravity anomaly* (RGA).

Accordingly, we focus our comparison on analyzing the relative gravity anomaly across the boundaries. We use the average gravity anomaly and standard error on the mean (noise measurement) to establish a limit of 4±2 milligals (mGal) for the relative gravity anomaly along the southern boundary of Arabia Terra. In northern Arabia Terra, we observe a strong negative gravity anomaly immediately exterior to the boundary. Relative to Arabia Terra, this highly localized signal provides for a negative relative gravity anomaly across the northern boundary, whereas an Arabia Terra erosional load would generate a positive relative gravity anomaly at the boundary. This anomaly could not have been generated by an erosional load interior to Arabia Terra and could conceivably be a result of crustal flow along the dichotomy boundary (37), (31). As a result, we contrast the interior gravity anomaly with its exterior counterpart beyond this highly localized signature to attain a 16±4-mGal relative gravity anomaly along the northern boundary.

We use the constraints of 6 mGal and 20 mGal for the maximum relative gravity anomalies for the southern highlands and northern lowlands, respectively.

2.3.3 Estimating Regional Elastic Thickness

Admittance & Coherence

In order to model the geophysical response to erosion within Arabia Terra, we must first constrain the elastic thickness at the time of the erosion. The free-air admittance relation is used to place limits on the effective elastic thickness for a given region (38). Over geologic timescales, the effective response of the Martian lithosphere to a surface load can be well approximated by an elastic plate with a specified elastic thickness, T_e. For thin elastic shell loading, Equations (2.8 -2.16) provide a linear mapping between the applied load and the gravity anomaly (27), neglecting finite amplitude effects. The transfer function relating the

final topography to the gravity anomaly is primarily sensitive to the elastic thickness and not the magnitude of the load.

In order to estimate the elastic thickness at the time Arabia Terra formed, we compute the localized admittance spectrum over the region and compare with similarly localized admittance spectra from the thin elastic shell model. The localization of the model and observational data averts the upward bias (inflated admittance values) as described by (38). The admittance spectrum, Z, is defined as

$$Z(l) = \frac{S_{gt}(l)}{S_{tt}(l)}, \tag{2.17}$$

where S_{gt} is the cross-power spectrum of the free-air gravity anomaly and topography and S_{tt} is the power spectrum of the topography (23). The observed topography, relative to a mean highlands' elevation of 2.1 km, is used to determine the associated gravity anomaly by Eq. (2.15) for an elastic thickness estimate; theoretical admittance spectra are subsequently calculated for a range of elastic thickness values.

The associated coherence represents the correlation between the surface topography and the gravity field. The associated coherence function, γ, is given by

$$\gamma(l) = \frac{S_{gt}(l)}{\sqrt{S_{tt}(l) S_{gg}(l)}}, \tag{2.18}$$

where S_{gg} is the power spectrum of the gravity field. A mismatch between the modeled and observed coherence may be indicative of loads that have not been represented. Modification processes such as un-modeled surface and subsurface loading may be primary factors in reducing the correlation between the gravity field and the surface topography (39). A satisfactory elastic thickness estimate, requires an admittance fit over a significant portion of wavelengths as well as a strong coherence.

For our analysis, all power spectra have been localized to the region of interest prior to admittance and coherence computation. Invoking this formalism assumes that surface and subsurface loading are statistically independent processes (40).

Results

Since the elastic thickness in Eqns. (2.8) and (2.9) is a sensitive parameter with respect to the permissible erosional load and is poorly constrained for Arabia Terra, we utilize the free-air gravity admittance to attain a better estimate. We identify the best-fit elastic thickness of T_e=15 km by minimizing the misfit (Figure 2-3(a)) between modeled and observed admittances. As we choose L_{win}=15, the localized admittance can only be computed for degrees 15 through 60, limited by the finite bandwidth of our spatio-spectral localization. As shown in Figure 2-3(b), this provides a reasonable fit between degrees 20 and 50, though the observed admittance takes a downturn beyond degree 50. The local maximum at degree 18 is a distortion by the long-wavelength effects of the rotational flattening and Tharsis, since degree-18 in the localized data includes contributions from as low as degree-3 in the global data fields. Notwithstanding this aberration in the admittance, an elastic thickness of 15 km provides a best fit between degrees 20 and 50.

For any region with accurately modeled loads, we expect a coherence near unity for all degrees (39). In the presence of noise, un-modeled surface loads, or sub-surface loading, the coherence may decrease. Though we restrict our investigation to only surface loading, the lesser values in the observed coherence also suggest that other processes – subsurface erosion or generation of crustal density anomalies – may have acted within Arabia Terra. Even so, the coherence (Figure 2-3(c)) remains relatively high for the localized region which indicates that if subsurface erosion did occur, it is not a significant influence on the regional gravitational anomaly.

2.4 Erosional Scenarios

We focus on four main erosional scenarios for the province of Arabia Terra:

1. Highlands' Elevation Load – an erosional load of the spatially-varying, present-day elevation difference between the mean southern highlands' elevation and Arabia Terra.

2. Flexural Fit – an erosional load yielding the current surface elevation of Arabia Terra after flexural adjustment.

3. Uniform – a uniformly thick layer of erosion applied to the whole of Arabia Terra.

4. Bounded – a linearly-interpolated load with erosional constraints at the northern and southern provincial boundaries.

We employ a forward modeling approach to thoroughly examine each of the aforementioned loading scenarios for Arabia Terra. For each scenario, the erosion is represented as a removal of a surface load with a uniform density of 2900 kg m^{-3} (8; 24). Though we acknowledge that other cases which partially erode a sub-region of Arabia Terra may be equally valid, for simplicity, we constrain our study to scenarios which erode the whole of Arabia Terra. The material eroded in these scenarios is assumed to have been removed entirely from the region.

2.4.1 Highlands' Elevation Load

The Highlands' Elevation Load (Figure 2-4(a)) represents the present-day elevation difference of Arabia Terra from the mean highlands' elevation of 2100 m. In this scenario, we investigate the viability of forming Arabia Terra from highlands-like terrain and crustal thickness by removing a load representative of the present-day elevation difference. The erosional load ranges from 0 to 5100 m in thickness (Figure 2-5(a)). We contrast this scenario with the Flexural Fit scenario to quantify the importance of flexure. Along with the assumption of an initial 2100-m elevation for Arabia Terra, we assume that the basic physical properties of the highlands are the same as those within Arabia Terra.

Applying the Highlands' Elevation Load to the thin elastic shell model results in a final topography that does not yield present-day Arabia Terra (Figure 2-6(a)). We disregard the sharp transition at the northern and southern edges as a result of spherical harmonic ringing inherent in such a model.

The flexural rebound (deflection) generates significant uplift (Figure 2-5(b)), yielding a

region with an elevation that decreases by 700 m from the southern to the northern boundary of Arabia Terra. This produces a final topography with an elevation trend shallower than the current Arabia Terra and deviates from the observed elevation at the northern boundary by over 4 km. As illustrated in Figure 2-6(a), the flexural rebound also generates 500 m of uplift exterior to the northern boundary. This 500-m uplift exterior to northern Arabia Terra lies outside of one standard deviation of the regional elevation profile. Additionally, the amount of erosion does not achieve the deficit required to match the observed reduction in regional crustal thickness (Figure 2-6(b)). Thus, the crustal thickness and the topography, interior and exterior to Arabia Terra, fail to match the observations.

Although the relative gravity anomaly along the southern boundary is small at 8 mGal, it still exceeds the 6-mGal limit imposed by the observations. Larger amounts of erosion at the northern boundary result in a greater relative gravity anomaly of 20 mGal, consistent with the maximum allowable RGA identified for northern Arabia Terra.

While this erosional scenario is nearly consistent with the observed gravity anomalies, it cannot reproduce the present-day topography or crustal thickness of the region. The inability of this scenario to yield an elevation consistent with the current state of Arabia Terra demonstrates the importance of flexure. The topography of Arabia Terra cannot be reproduced without significantly more erosion than calculated by the elevation difference alone. Hence, this erosional scenario cannot be singularly responsible for the formation of Arabia Terra.

2.4.2 Flexural Fit

Incorporating flexure into the reconstruction of the original surface requires erosion of a significantly greater amount (Figure 2-4(b)) than the prior scenario. We employ an analogous relation to Equation 2.10, as previously discussed, to permit an explicit calculation of the amount of additional erosion required to produce the present-day Arabia Terra topography. The supposition of erosion as the primary mechanism responsible for the current physiographic state of Arabia Terra requires the initial (pre-erosion) elevation to be coincident

with the southern highlands' elevation of 2100 m, similar to the previous scenario.

The erosional load required to form the topography of Arabia Terra from an initial state similar to the southern highlands is shown in Figure 2-7(a). The amount of erosion is equivalent to a 750-m layer of sediment spread across the whole of the northern lowlands. With a 15-km elastic thickness, this scenario erodes up to 22 km at the northern extremity yielding a total eroded volume of 1.7×10^8 km^3. This erosional load reproduces the crustal thickness deficit (Figure 2-6(b)) to within 5 km of Arabia Terra relative to the southern highlands.

As a consequence of erosional amounts in excess of the elastic (lithosphere) thickness, we invoke the caveat that the erosion must transpire on a timescale sufficiently long to allow for thermal diffusion to maintain a minimal elastic thickness of 15 km. Using the thermal diffusion timescale, the erosion must occur in no less than 2.4 My or at a rate less than 9.2 mm/yr. This rate is orders of magnitude greater than the average erosion rates estimated for Mars (14), justifying the assumption of a minimal elastic thickness during the erosional event.

Though the erosional load is designed to reproduce the topographic expression of Arabia Terra, the scenario fails to reproduce the elevation exterior to Arabia Terra and an allowable relative gravity anomaly. In eroding nearly 22 km at the northern extremity, the resultant flexural rebound produces uplift of over 1 km immediately exterior to Arabia Terra. This substantial elevation rise is contradictory to the observations and is too large to be masked by measurement noise. While this 1-km exterior uplift alone is sufficient to deem this scenario implausible, the resultant gravitational anomaly further diminishes the viability of this scenario. The gravity anomaly map in Figure 2-7(c) contains an 80-mGal relative gravity anomaly across the northern boundary, 60 mGal greater than allowable for northern Arabia Terra. Furthermore, this scenario establishes a strong gradient in the gravity anomaly interior to Arabia Terra, contradictory to observations of a nearly uniform gravity anomaly. The relative gravity anomaly on the southern boundary of 40 mGal also surpasses the allowable RGA of 6 mGal.

Though the relative gravity anomalies are too large to be accommodated by the observa-

tions, the resulting crustal thickness trend more closely resembles crustal thickness models than the prior scenario. While the discrepancy in crustal thickness in the erosional model is small, the overcompensated, excess crustal thickness is sufficient to produce large negative gravity anomalies over Arabia Terra, in conflict with the observations.

This scenario is designed to reproduce the topography of Arabia Terra via erosion from an initial state similar to the southern highlands. Using this scenario, we produce an overcompensated Arabia Terra crustal thickness estimate with a gravity anomaly trend interior to Arabia Terra and relative gravity anomalies on the northern and southern boundaries that exceed the observations. Thus, these results demonstrate that erosion cannot be solely responsible for the formation of the current Arabia Terra from a highlands-like elevation.

2.4.3 Uniform Erosion

This scenario diverges from the notion of a pre-erosional Arabia Terra commensurate with the southern highlands and instead erodes a uniformly thick layer from Arabia Terra. In order to yield a final elevation and crustal thickness consistent with the current state of Arabia Terra, the pre-erosional state includes isostatic crustal thickness variations specific to the applied erosional load.

As the gravity anomalies arising from isostatically compensated topography are small relative to those arising from flexurally supported loads, the uniform erosion scenario will produce a similar relative gravity anomaly across all boundaries. We first consider an amount of erosion consistent with (11), a uniform erosional load of 450 m. This erosional load produces a 3-mGal and 2-mGal relative gravity anomaly on the northern and southern boundaries, respectively (Figure 2-8(c)). The amount of flexural rebound immediately exterior to Arabia Terra is minimal. Accordingly, this amount of erosion is allowable based on the observations.

Using an iterative, forward-modeling approach to minimize the misfit between the modeled and observed relative gravity anomalies, we can determine the maximum amount of uni-

form erosion consistent with the observations. The 6-mGal relative gravity anomaly on the southern boundary is the primary constraint, allowing for a maximum uniform erosional load (Figure 2-8(a)) of approximately 1300 m. Neglecting contributions to the southern RGA from noise/error, a best-fit uniform erosional load can also be determined: 750 m.

2.4.4 Bounded Erosion

The difference in the observed northern and southern RGA upper limit suggests that a relatively larger amount of erosion is allowable along the northern boundary. In this scenario, we consider a load with assigned erosional amounts on each boundary; between the boundaries, the erosion is linearly interpolated to attain the erosional load.

Through an iterative forward-modeling scheme similar to the prior scenario, we determine the maximum amount of erosion for Arabia Terra (Figure 2-8(b)) – erosion linearly increases from 300 m in the south and culminates at 5000 m in the north. This maximum erosional load attains the 6-mGal and 20-mGal relative gravity anomaly upper limit along the southern and northern boundaries, respectively. Thus, this bounded erosional load is compatible with the upper bound of the relative gravity anomalies along the boundaries. This maximum erosional load amounts to 3.1×10^7 km^3 of material that could have conceivably been removed from Arabia Terra. Additionally, we calculate a best-fit bounded erosional load designed to match the observed northern and southern RGA without error. The best-fit bounded erosional load increases from no erosion in the south to 4000 m in the north.

2.5 Discussion

The thin elastic shell loading model applied here provides constraints on the maximum volume of erosion which can reproduce the observed gravity anomalies (Table 2.3). In addressing erosion from the vantage of geophysics, we eliminate uncertainty in the inter-

pretation of geological units and employ a model independent of specific fluvial or aeolian processes. Our 15-km elastic thickness is consistent with past estimates for northeastern Arabia Terra and the bulk of the southern highlands ($T_e < 16$ km) (24; 41). In general, the southern highlands have a lower elastic thickness than the more rigid lowlands, yielding more intermediate elastic thickness estimates along the dichotomy boundary (24; 41; 8; 42; 43; 44; 45).

Any significant alteration of Arabia Terra would have likely occurred prior to the onset of the Hesperian epoch in order to maintain current estimates for the terrain age (13) and to be consistent with the thin elastic thickness (24). It is likely that if erosion did occur within Arabia Terra, it may have occurred over a period of time (15; 11; 14) rather than in a single event. As our admittance and coherence analysis indicates, Arabia Terra was formed in the presence of a 15-km elastic lithosphere; any subsequent surface modification would have occurred at a greater elastic thickness. Since the lithosphere becomes more rigid over time (i.e. the elastic thickness increases), a given erosional load will result in a larger relative gravity anomaly. Therefore, by modeling erosion with a 15-km elastic lithosphere, the viable erosional loads likely represent an upper limit for erosion within Arabia Terra.

As illustrated by the Highlands' Elevation Load, the Arabia Terra topography cannot be reproduced by the removal of a load representative of the elevation difference as a result of subsequent flexural rebound. Although we can reproduce the topography of Arabia Terra via the Flexural Fit scenario, the erosion required produces large gravity anomalies and lowlands' uplift in conflict with the observations. Further, the removal of massive amounts of material would have likely generated large surface stresses and tectonic features contrary to regional observations (46; 47).

Although the current physiographic expression of Arabia Terra cannot be explained by erosion, lesser amounts of erosion are allowable within the region from the geodynamical constraints. Employing a fit to the relative gravity anomaly of Arabia Terra, uniform erosion of no greater than 1300 m of material could have occurred; beyond 1300 m, the relative gravity anomaly along the southern boundary of the province is exceeded. However,

the larger relative gravity anomaly in northern Arabia Terra allows for a greater amount of material to have been removed. Accordingly, our bounded erosional load can reproduce the difference between the maximum allowable relative gravity anomalies. The erosional load linearly increases with distance from the southern boundary of Arabia Terra with 300 m of erosion in the south and up to 5000 m in the north. The load represents the maximum amount that may be removed from Arabia Terra: 3×10^7 km^3 of material. Though this load is consistent with the gravity observations, it cannot produce the Arabia Terra topography or crustal structure from highlands-like topography or crustal thickness.

Given the constraint on the surface age from crater statistics, a majority of the erosion from the Highlands Flexural Fit scenario would have had to occur no later than $\sim$3.8 Ga. Though lateral crustal flow may have diminished the resultant gravity anomalies observed on present-day Mars, the persistence of the north-south crustal dichotomy boundary through the early Noachian provides a constraint on crustal relaxation (8; 48; 37; 49). On the basis of thermal models that include consideration of crustal heat production and the role of hydrothermal circulation in the crust, relaxation rates $<10^{-17}$ s^{-1} required to maintain crustal thickness variations are achieved (49). The relaxation rate constraint is easily met for plausible thermal structures in the Noachian, and limits vertical perturbation of the crust-mantle boundary to be on the order of 1 km within Arabia Terra. Thus, while crustal flow within Arabia Terra would affect our estimate on the maximum amount of erosion, erosion with crustal flow still cannot explain the formation of Arabia Terra from the southern highlands. Further, it is likely crustal-thinning resulting from erosion would increase the effective viscosity allowing for greater preservation of the Arabia Terra crustal profile (37; 8). Ultimately, given the assumption of a pre-erosional Arabia Terra similar to the highlands, the preservation of the large-scale Noachian crustal thickness variations on Mars (i.e. crustal dichotomy boundary, Hellas) suggests that lower crustal flow would not have been substantial within Arabia Terra (37).

2.6 Conclusions

In order for erosion to be a viable candidate for the formation of Arabia Terra from highlands-like topography and crustal thickness, an erosional model must reproduce the topography and gravity anomaly both within and exterior to the region. Appropriately reproducing the topography entails the consideration of flexure; without the consideration of flexure the load itself cannot properly be determined or evaluated.

Our admittance analysis demonstrates that the present-day topography of Arabia Terra was established in the presence of a 15-km elastic lithosphere. This lithosphere thickness determines the flexural response of Arabia Terra to any large-scale loading event. In order to generate via erosion the observed topography of Arabia Terra from highlands-like topography and crustal thickness, 1.7×10^8 km^3 of material must be eroded from the region. However, this erosion would result in a substantial flexural uplift of the lithosphere immediately exterior to Arabia Terra and resultant gravity anomalies that exceed observations by $\sim$60 mGal.

This work demonstrates the maximum amount of erosion that could have occurred in Arabia Terra is 3×10^7 km^3, consistent with the geological minimum established by (11). Further, we conclude that either some other mechanism (e.g., (31)) removed crust from Arabia Terra thereby dominating the regional evolution or alternatively the region developed with less topography and a thinner crust relative to the rest of the southern highlands. If the unique physiography of this region is a result of erosion, it must have been accompanied by significant viscous relaxation (37) or must have possessed large isostatic crustal thickness variations prior to erosion. Ultimately, erosion alone cannot explain the observed topography and crustal thickness deficit of Arabia Terra.

2.7 Acknowledgements

I thank Jeff Andrews-Hanna for guidance and support in developing models and research approach and I think F. Simons for assistance in spherical harmonic localization.

2.8 Figures

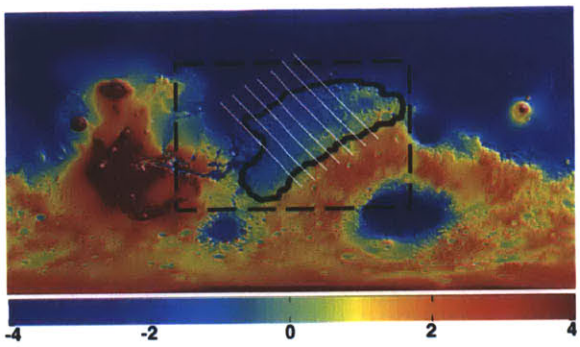

(a) Mars Global Topography (km).

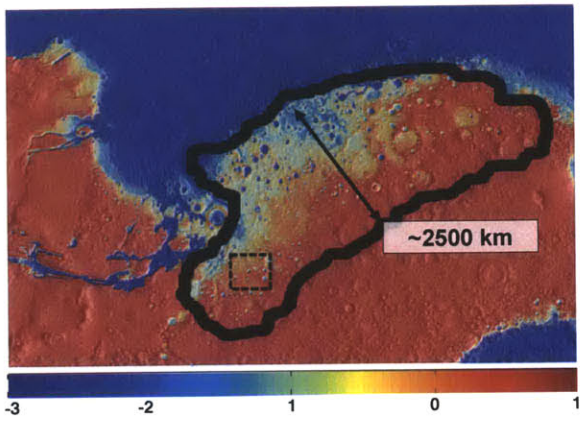

(b) Regional Topography (km).

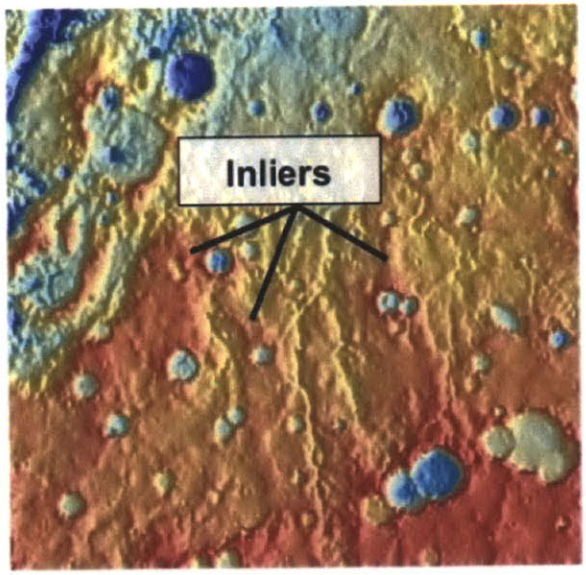

(c) Regional Terrain (km).

Figure 2-1: Mars Topography (km). (a) The solid black line encloses the region of Arabia Terra. The seven white lines are profiles used in the construction of subsequent regional profile figures. The dashed box represents (b) in the global topography. (b) Shaded relief elevation map of the Arabia Terra region. Over a 2500-km span, the topography of Arabia decreases by 5 km. The dashed box represents (c) in the regional topography. (c) A view of the isolated mesas within Arabia Terra.

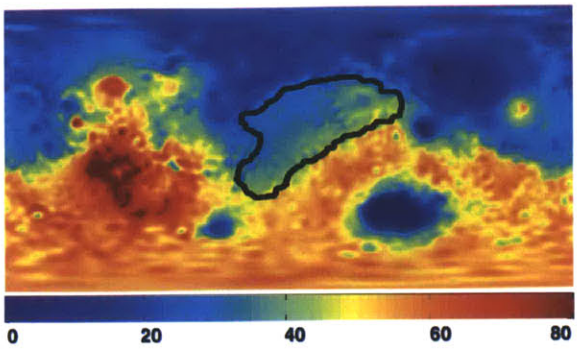

(a) Mars Global Crustal Thickness (km).

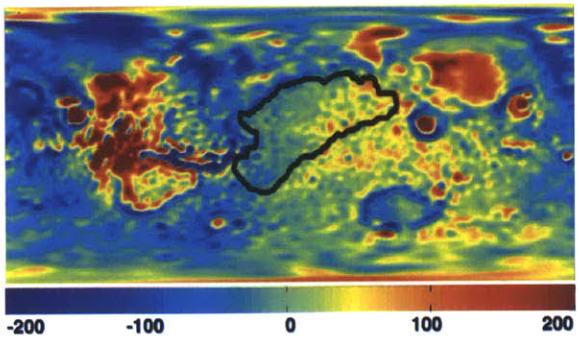

(b) Mars Global Gravity Anomaly (mGal).

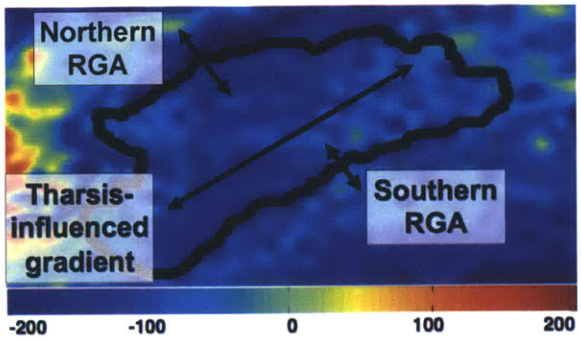

(c) Arabia Terra Regional Gravity Anomaly (mGal).

Figure 2-2: Mars Crustal Thickness and Gravity Anomaly Maps. (a) Global Crustal Thickness (km). Within the region of Arabia Terra, the crustal thickness decreases from 53 km to 28 km near the northern border, yielding a total crustal thickness reduction of 25 km. The region enclosed by the solid black line is Arabia Terra. (b) Mars Global Gravity Anomaly (mGal). The Arabia Terra region is dominated by the antipodal signature associated with Tharsis. (c) Offset Regional Gravity Anomaly (mGal). A regional gravity anomaly map with a center-of-mass offset ($g_{1,0} =< 18, 0 >$ and $g_{1,1} =< 43, -144 >$ of the gravity field, g_{lm}) incorporated to offset the antipodal signature associated with Tharsis.

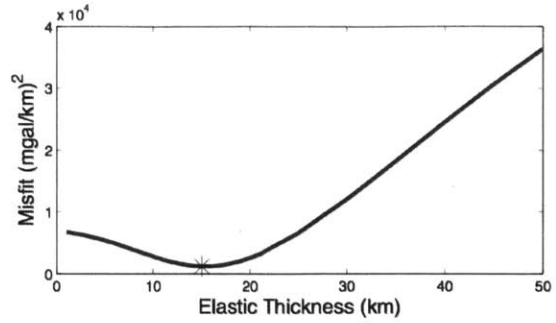

(a) Admittance Misfit.

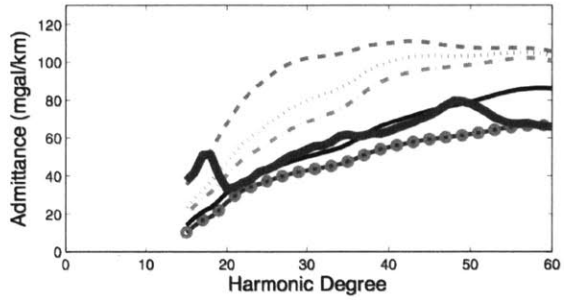

(b) Model and Observation Admittance.

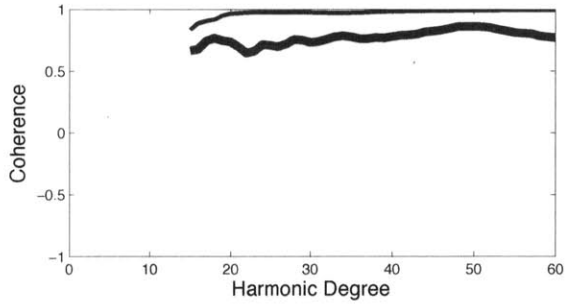

(c) Coherence.

Figure 2-3: (a) Admittance Minimum Misfit. The admittance for Arabia Terra is best fit by a model with an elastic thickness of 15 km, denoted in the misfit by the asterisk. The misfit is applied between degrees 20 through 50. (b) Model and Observation Admittance. The model admittance is shown above for an elastic lithosphere thickness of 5 km (circles), 15 km (solid), 30 km (dashed-dotted), 45 km (dotted), and 60 km (dashed). The thick line represents the actual free-air admittance for Arabia Terra. The peak in admittance near degree-18 is due to long-wavelength effects (e.g., Tharsis). (c) Coherence. The thick line represents the coherence for Arabia Terra and the thin line represents the theoretical coherence for an elastic lithosphere of 15 km.

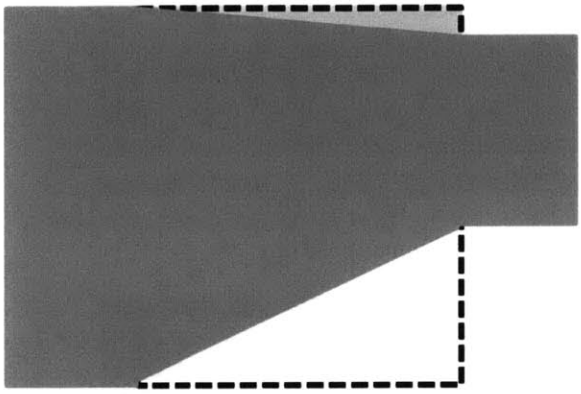

(a) Highlands' Elevation Load.

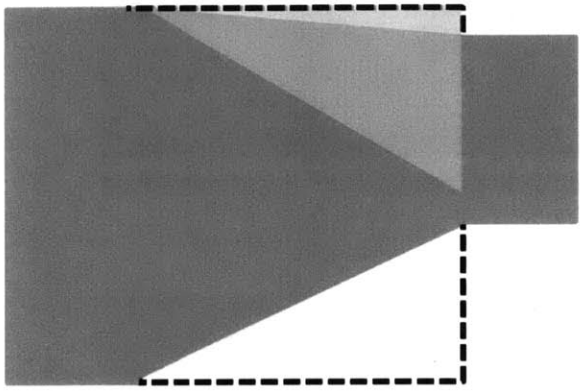

(b) Flexural Fit.

Figure 2-4: Conceptual Model. Extending left to right from the southern highlands to the northern lowlands, respectively, the conceptual model illustrates a crustal cross-section along the Arabia Terra dichotomy boundary. The dark-shaded region represents the present-day crustal thickness and elevation of Arabia Terra. The dashed lines represent the pre-erosional state of Arabia Terra with a highlands-like elevation and crustal thickness. The light-shaded region represents the eroded amount for each scenario. (a) Highlands' Elevation Load. The erosional load is the spatially-varying elevation difference between the mean southern highlands' elevation (pre-erosional Arabia Terra and the present-day Arabia Terra elevation. (b) Flexural Fit. The erosional load (superimposed on present-day topography) is designed to match the observed elevation of Arabia Terra by accounting for flexure. Significantly more erosion is required than in the Highlands' Elevation Load.

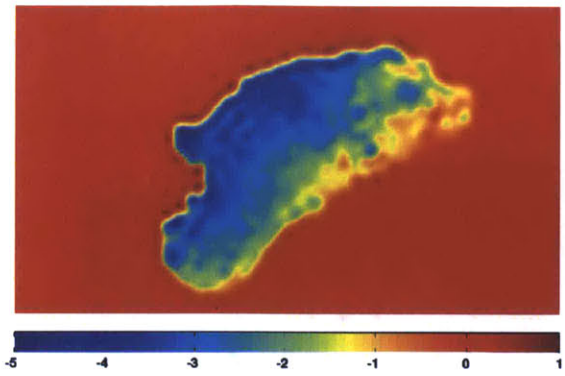

(a) Erosional Load (km).

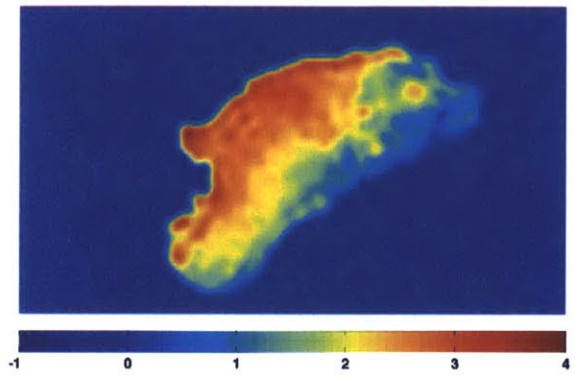

(b) Deflection (km).

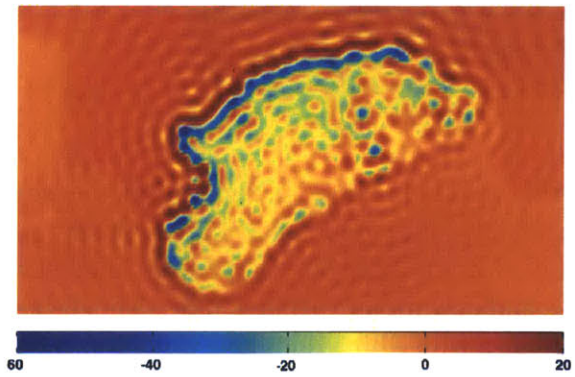

(c) Gravity Anomaly (mGal).

Figure 2-5: Highlands' Elevation Load. (a) Erosional Load (km). Load applied to Arabia Terra region. The erosional load is the spatially-varying elevation difference between the mean southern highlands' elevation and the Arabia Terra elevation. (b) Deflection (km). Resultant flexure from erosional load. (c) Gravity Anomaly (mGal). The model gravity anomaly map of Arabia Terra after the erosion. The resultant gravity anomaly includes the finite amplitude effect resulting from topography on the surface and along the crust-mantle boundary.

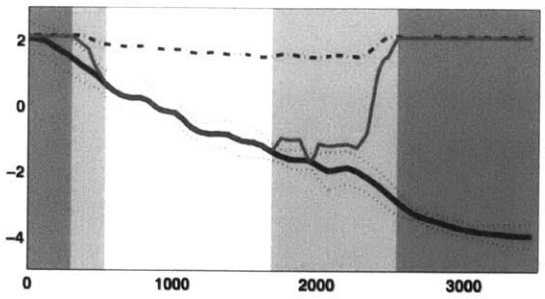

(a) Elevation (km).

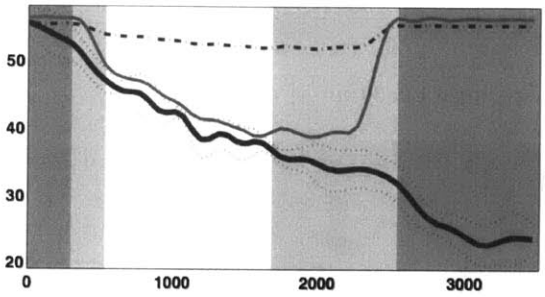

(b) Crustal Thickness (km).

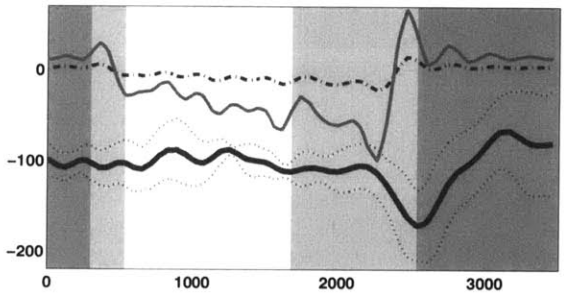

(c) Gravity Anomaly (mGal).

Figure 2-6: Averaged Profiles for Formational Erosion Scenarios. The profiles extend from the southern highlands to the northern lowlands as shown in Figure 2-1(a). The distance from the southern highlands is on the horizontal axis. The unshaded regions contain data internal to Arabia Terra. The light-shaded regions incorporate data interior and exterior to Arabia Terra, while the dark-shaded region represents data solely exterior to Arabia Terra. Shown above are model data of the Flexural Fit scenario (thin solid), the Highlands' Elevation Load scenario (dashed-dotted), and the observation data (thick solid) along with the standard deviation (dotted) of Arabia Terra. (a) Elevation (km). The final topography of the formational erosion scenarios, referenced to a 2100 m elevation, are shown with the present-day elevation of the region. The averaged profile for the Flexural Fit scenario matches the present-day Arabia Terra elevation, unlike the Highlands' Elevation Load. (b) Crustal Thickness (km). The present-day crustal thickness of Arabia Terra is matched by the Flexural Fit scenario within the region, unlike the Highlands' Elevation Load scenario. (c) Gravity Anomaly (mGal). The observed relative gravity anomaly (exterior gravity anomaly less the interior gravity anomaly) is exceeded by both formational erosion scenarios.

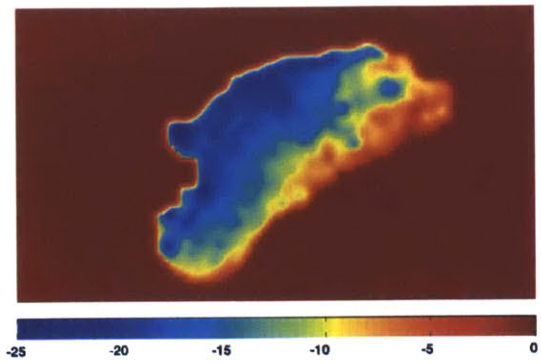

(a) Erosional Load (km).

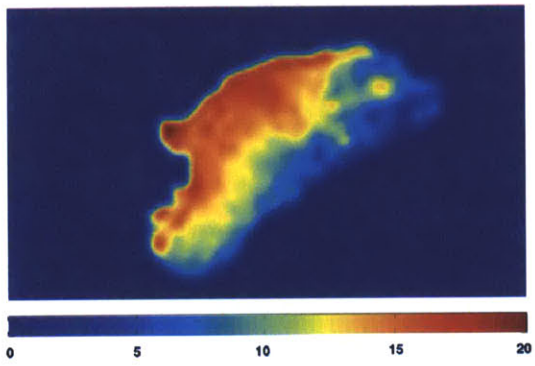

(b) Deflection (km).

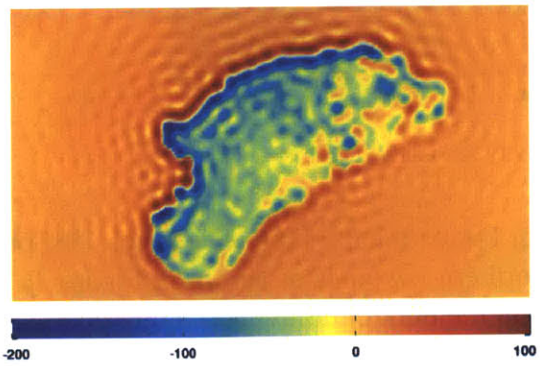

(c) Gravity Anomaly (mGal).

Figure 2-7: Flexural Fit Scenario. (a) Erosional Load (km). Load applied to Arabia Terra region. The erosional load is designed to match the observed elevation of Arabia Terra. (b) Deflection (km). Resultant flexure from erosional load. (c) Gravity Anomaly (mGal). The model gravity anomaly map of Arabia Terra after the erosion. The resultant gravity anomaly includes the finite amplitude effect resulting from topography on the surface and along the crust-mantle boundary.

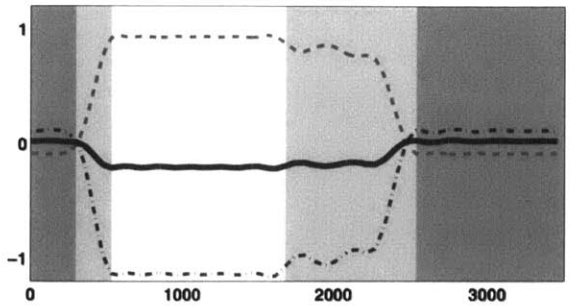

(a) Maximum Uniform Erosional Load (km).

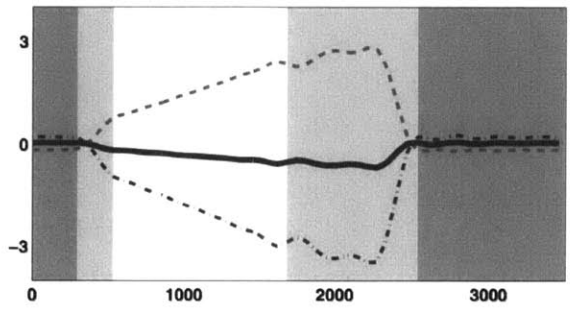

(b) Maximum Bounded Erosional Load (km).

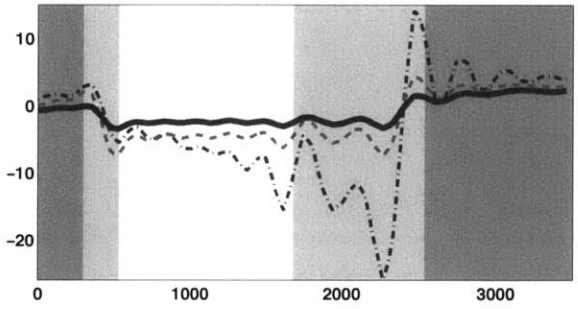

(c) Gravity Anomaly (mGal).

Figure 2-8: Averaged Profiles for Non-Formational Erosion Scenarios. The profiles extend from the southern highlands to the northern lowlands as shown in Figure 2-1(a). The distance from the southern highlands is on the horizontal axis. The unshaded regions contain data internal to Arabia Terra. The light-shaded regions incorporate data interior and exterior to Arabia Terra, while the dark-shaded region represents data solely exterior to Arabia Terra. (a) Maximum Bounded Erosional Load (km). The offset of the present-day topography from the initial topography (solid line) is shown along with the erosion load (dashed-dotted line) and the deflection (dashed line). (b) Maximum Uniform Erosional Load (km). The offset of the present-day topography from the initial topography (solid line) is shown along with the 1300-m uniform erosional load (dashed-dotted line) and the deflection (dashed line). (c) Gravity Anomaly (mGal). Averaged profile of gravity anomaly for 450-m erosional load (solid line), maximum uniform erosional load (dashed line), and the maximum bounded erosional load (dashed-dotted line).

2.9 Tables

Table 2.1: Parameter Values for the Thin Elastic Shell Loading Model

Parameter	Value
Crustal Density, ρ_c	2900 kg m^{-3}
Load Density, ρ_L	2900 kg m^{-3}
Mantle Density, ρ_m	3500 kg m^{-3}
Mean Density, $\bar{\rho}$	3940 kg m^{-3}
Gravity, g	3.72 m s^{-2}
Equatorial Radius, R_eq	3396 km
Mean Planetary Radius, R_p	3389.5 km
Poisson's Ratio, ν	0.25
Shell Thickness, T_e	15 km
Young's Modulus, E	10^{11} N m^{-2}

Table 2.2: Parameter Values for the Density Interfaces

Parameter	Surface Interface	Mantle Interface
Density Change, $\Delta\hat{\rho}$	ρ_c	$\rho_m - \rho_c$
Reference Radius, r	R	$R - T_{crust}$
Shape, $\hat{S}_{lm}$	$\hat{h}_{lm} + A_{lm}$	$w_{lm} + A_{lm}$

Table 2.3: Erosion Scenario Summary.

Scenario	Relative Gravity Anomaly (mGal)[a]		Erosional Load (m)	
	North	South	North	South
Observations	*16 ± 4*	*4 ± 2*	-	-
Highlands' Elevation Load	20	8	5100	0
Flexural Fit	80	40	25000	0
Uniform Erosion (450 m)	3	2	450	450
Uniform Erosion: Maximum	7	6	1300	1300
Bounded Erosion: Maximum	20	6	5000	300
Uniform Erosion: Best-fit	5	4	750	750
Bounded Erosion: Best-fit	16	4	4000	0

[a]The uncertainty on the relative gravity anomaly is determined from the standard error on the mean.

Chapter 3

A Wet, Heterogenous Lunar Interior: Lower Mantle & Core Dynamo Evolution

3.1 Introduction

The Moon is posited to have formed from the coalescence of post-impact debris of a proto-planet with the young Earth (50; 51). Following the giant impact of the Earth with a planetary embryo, material scattered beyond the Roche-limit into a proto-lunar disk and subsequently aggregated to form the Moon (51; 50; 52; 53). The anorthositic and KREEP-rich (material rich in potassium, rare Earth elements, and phosphorus) composition of the lunar highlands (54) supports the past existence of a large-scale lunar magma ocean leading to fractional crystallization and compositional stratification of the Moon(55; 56; 57). Although a 40- to 50-km anorthositic lunar crust is consistent with a magma ocean depth of up to 1000 km, a lower depth limit may be expected given recent observational data from the dual Gravity Recovaery and Interior Laboratory (GRAIL) spacecraft (58) that indicates an average crustal thickness between 34 and 43 km (59). During the final stages of fractional crystallization from a lunar magma ocean, the last dregs of the melt would be enriched

in water and incompatible elements, subsequently crystallizing beneath the anorthositic crustal lid (60; 61). Further, fractional crystallization would result in a chemically-layered mantle, which may be supported by some seismic observations (29). Until recently, the Moon had been thought to have a relatively low volatile content due to a combination of its low gravity and hot impact origin (62; 63). Accordingly, past studies of the Moon's formation and its chemical and thermal evolution have focused on a bulk Moon with minimal volatile content and absent of water (64). However, recent geochemical analyses of very-low-Ti glasses and lunar melt inclusions present compelling evidence that water concentrations of at least 260 ppm and up to 6000 ppm were present in the deep lunar interior prior to 3 Ga (65; 66). If water was a constituent of the bulk Moon, fractional crystallization of all but the deep mantle would have resulted in a sequestered source of interior water. Ultimately, in this scenario, a post-magma ocean Moon would contain separate sub-crustal and deep mantle reservoirs, which may be dually consistent with localized water-rich reservoirs ($\geq$260 ppm) (65), and a bulk magma ocean containing under 100 ppm water (67).

While deuterium to hydrogen (D/H) ratios of measured lunar water in apatite are consistent with a cometary origin (68), the observed hydrogen fractionation could alternatively result from water-rich glasses erupted from a source region with terrestrial D/H values, provided the glasses have undergone kinetic fractionation during post-eruptive degassing (69). (63) find, absent removal mechanisms that may be responsible for later depletion of terrestrial-imparted volatiles, a post-formation enhancement of volatiles relative to the silicate Earth is likely for the Moon.

Regardless of whether the origin of lunar water is indigenous, exogenous or a combination thereof, water in the deep lunar interior must have been retained from accretion or accreted prior to and perhaps during lunar magma ocean solidification. Under the lunar magma ocean model, water would be progressively enriched with incompatible elements during solidification, and a fraction may have been retained by the lunar mantle (70; 67). Although it is unclear whether measured water concentrations are representative of the entire lunar mantle or a water-enriched reservoir (66), the existence and subsequent enrichment of water in the lunar interior could well have had a significant effect on early lunar thermochemical

evolution (64; 71). In particular, water may have aided the cooling of the early Moon (72; 73) in addition to influencing the expression of surface features such as impact basins.

Unlike the Earth (74), deep reservoirs of water within the Moon could conceivably exist near the core-mantle boundary and, if so, could decrease lower mantle viscosity, possibly facilitating a prolonged and perhaps vigorous lunar dynamo. While the size and composition of the lunar core are still a matter of active investigation (75), recent analyses of lunar samples indicate that the Moon had a dynamo-driven magnetic field from at least 4.2-3.56 Ga, consistent with the presence of an advecting liquid iron-rich core (76; 77; 78; 79). Given bounds on the lunar core size (80), it may be implausible for homogeneous mantle convection from secular cooling to generate such a long-lasting dynamo via core convection (79) without mediation by a thermal blanket (81), impact-induced rotation changes(82), compositionally stratified mantle convection or, possibly, a water-rich layer near the core-mantle boundary. Although the cooling history of the Moon is still ambiguous, there is some evidence, including recovered lunar alkalic igneous rocks, indicative of a late rapid cooling scenario for the shallow part of the Moon which may have been preceded, or overlapped, with a slow cooling phase of the deep Moon (54; 83; 84). Such a scenario would be consistent with a convective core dynamo. In this study, we address the influence of water on lunar evolution by incorporating an attenuating strain rate as a proxy for decreased viscosity (64; 71; 85) for potential wet regions in the lunar interior. From experimental studies of the Earth's upper mantle (300 MPa), the presence small amounts of water ($\sim$20 wt. ppm) can result in a viscosity reduction by a factor in excess of 100 (71; 85). We examine the influence of compositional stratification and water via protonic weakening (85) - proton diffusion into nominally anhydrous minerals - on the deep interior. We utilize a finite-element thermochemical evolution model and investigate changes in temperature, modes of heat transport, core-mantle boundary heat flux and surface magnetic field intensity. We then use the core-mantle boundary heat flux to provide constraints on the duration of core dynamo activity.

3.2 Methodology

3.2.1 Thermochemical Evolution

We employ a modified version of the spherical, axisymmetric finite-element thermochemical evolution (convective and conductive heat transport) code, Citcom2D (86; 87; 88) that models two-dimensional incompressible mantle evolution with the Boussinesq approximation through the non-dimensionalized governing equations of the conservation of mass, momentum, and energy,

$$u_{i,i} = 0 \tag{3.1}$$

$$-P_{,j} + \left[\eta(r,T)\left(u_{i,j} + u_{j,i}\right)\right]_{,j} + Ra\left(T - \beta C\right)\delta_{i,r} = 0 \tag{3.2}$$

$$\dot{T} + u_i T_{,i} = \kappa T_{,ii} + H(t) \tag{3.3}$$

where $\vec{u}$ is the velocity vector, P is the dynamic pressure, Ra is the Rayleigh number referenced to the lunar radius, β is the buoyancy number calculated from the difference in density and reference density, and T is the temperature. Values used for thermochemical evolution model are listed in Table 3.1 In the above equations, we employ Einstein notation to indicate summation over repeated indices, with a subscript comma denoting the derivative with respect to the following spatial index. We modify this formalism to allow for a time-dependent heat source, $H(t)$, to account for radioactive decay (Table 3.2) and we incorporate a temperature- and depth-dependent viscosity, $\eta(R,T)$

$$\eta(r,T) = A\eta_o \exp\left[\frac{E' + V'(1-r)}{T + T'_s} - \frac{E' + V'(1 - r_{core})}{1 + T'_s}\right] \tag{3.4}$$

$$E' = \frac{E}{R\Delta T}, V' = \frac{\rho g V R_p}{R\Delta T}, T'_s = \frac{T_s}{\Delta T}$$

where E', V', and T_s', are the non-dimensionalized activation energy, E, activation volume, V and surface temperature, T_s, respectively (89; 90), and η_o is the reference viscosity. The parameter ΔT represents the temperature difference across the mantle, g is the lunar surface gravity, and A is a dimensionless pre-exponential factor, herein used to incorporate viscosity reduction. We apply this viscosity equation in Sections 3.1 and 3.2.

To model the cooling of the core-mantle boundary (CMB), we adjust the model to allow for a time-varying CMB thermal boundary condition based on

$$\dot{T}_{cmb} = \frac{-k_m T_{,i} S}{(\rho C_p V)_{core}} \tag{3.5}$$

where T, i is the temperature gradient above the CMB, S is the surface area and V is the volume of the core, k_m is mantle conductivity, ρ is the core density and C_p is the core specific heat. Additionally, we use a particle tracer method (91) to allow for radially-varying density structures and radioactive element concentrations. In addition to bottom heating, we include volumetric heating of the mantle, crust, and KREEP layer, starting from the initial radioactive element concentrations listed in Table 3.2.

Prior lunar mantle convection models (81; 92) have applied a variant of the viscosity equation,

$$\eta(P,T) = A\eta_o \exp\left[a\frac{E+PV}{RT}\right] \tag{3.6}$$

with a partially non-dimensionalized viscosity equation (93) that damps the temperature-dependence of viscosity (Eq. 3.6). Although the non-dimensionalized Arrhenius equation (Eq. 3.4) uses radial distance as a proxy for pressure ($\rho g h$), ultimately the difference in gravity between the surface and the core is not a determining factor in the convection model. The key difference in heat flux predicted by the two viscosity equations is a result of the damping of the temperature dependence by a scale factor, a. This constant a is partially offset by the omission of a second exponential term that references viscosity to the CMB as in Equation 3.4. In Section 3.3.2, we use this variant of the viscosity equation as a proxy for a set of scenarios in which the pre-overturn temperature of the magma ocean cumulates is not completely retained, and to illustrate the differences in applying a rheological equation

that does not fully account for the temperature dependence of viscosity. We normalize the viscosity at the CMB to our reference viscosity, 10^{20} Pa-s.

3.2.2 Water, Pressure, and Rheology

Experimental studies of olivine aggregates and single crystals demonstrate that viscosity is reduced in the presence of water (protons) (94; 95). (94) found viscosity is reduced by up to a factor of 140 for saturated olivine, corresponding to 40±20 ppm H, at confining pressures of 300 MPa. Their re-examination of higher pressure data from (96) further suggests that the viscosity reduction factor is directly proportional to the concentration of water in the olivine crystal matrix. Consequently, with the pressure-dependent increase of water solubility in olivine, we expect a maximum viscosity reduction factor in excess of 140 for a deep lunar mantle (≥300 MPa) preferentially enriched in water and approximately a factor of 140 or less at the near-surface given the lower pressure.

3.2.3 Core Heat Flux & Magnetic Field Intensity

We consider a core dynamo driven by thermal core convection. In this case, a necessary but not sufficient condition for an internally-generated magnetic field on the Moon is a heat flux at the core-mantle boundary (CMB) above the critical threshold value, q_{ad}, of that carried conductively along the core adiabat, where

$$q_{ad} = \frac{4\pi G \alpha_c \rho_{\text{core}} T_c k_c R_c}{3 c_{p,\text{core}}}. \tag{3.7}$$

We define the relevant variables in Table 3.1. Using the energy flux to magnetic field strength scaling of (97) and assuming constant material properties in the core (see Table 3.3), we can employ the following relation as an upper limit for the surface magnetic field intensity that can be produced from our core heat flux

$$B_s = \left(\frac{R_c}{R_p}\right)^3 \sqrt{2\mu_o c f_{\text{ohm}} \rho_{\text{core}}^{1/3}} \left[\frac{(q_{cmb} - q_{ad}) q_{ad} R_c}{k_c T_c}\right]^{1/3}, \tag{3.8}$$

which can be reduced to $B_s = 8.5 \times 10^{-5} \left[q_{\text{ad}} \left(q_{\text{cmb}} - q_{\text{ad}}\right)\right]^{1/3}$, where B_s is the magnetic field intensity (Teslas), and is scaled by the squared difference of the CMB heat flux less the core adiabatic flux.

Many workers have attempted to examine the possibility of an internally-generated lunar magnetic field (98; 99; 81; 100; 82), finding that core convection generally cannot be sustained after 3.5 Ga (98; 81). Additionally, varied assumptions in Eq. 3.7 lead to variations in the minimum heat flux (1-10mW/m^2) required for sustaining a core dynamo. Herein, for a 350-km core, we use a critical threshold value between 2.4-4.0 mW/m^2 as a sufficient constraint to sustain a core dynamo.

3.3 Results

We investigate the effect of water on lower-mantle thermal evolution through end-member scenarios of initial density and temperature profiles within the Moon. Estimates of lunar magma ocean depth are based upon the thickness of the feldspar-rich flotation crust and recent modeling by (1) suggest a depth of up to 1000 km for a lunar magma ocean, while more conservative estimates yield up to 250 km (57). A 1000-km deep lunar magma ocean (LMO) crystallizes with an unstable density profile, leading to gravitationally driven overturn of the magma ocean cumulates and thereby permitting cooler, near-surface material to be transported deeper in the mantle. While a similar gravitationally driven overturn may occur for shallower lunar magma oceans, we model a 400-km-deep lunar magma ocean as a chemically homogeneous mantle. Accordingly, we choose the following two end-member scenarios for initialization of our evolution model and assume a model start time of 4.4 Ga (Figure 3-1):

1. Shallow Magma Ocean - a chemically homogeneous mantle at a temperature of 1600 K below 400-km depth and with a temperature that varies linearly from 1450 K to

1600 K from the surface to 400 km depth.

2. Deep Magma Ocean - a chemically-heterogeneous mantle at a post-magma ocean overturn temperature and density (Figure 3-1). From the surface, the density increases linearly from 3000 to 3500 kg/m^3 until 1000-km depth. This model of lunar convection may be consistent with possible seismic discontinuities of magma ocean cumulates (29), which may be a result of layering from overturn of the lunar magma ocean.

Using the fully non-dimensionalized Arrhenius equation (Eq. 3.4), we explore the effect of water enrichment for a range of CMB temperature boundary conditions. While the lunar core may be capable of initially retaining a 700-K higher temperature relative to the lower mantle (98), we examine moderate cases initiated with a temperature difference across the core-mantle boundary, $\Delta T_{cmb} \leq 200$ K. In Section 3.3.2, we examine the effect of varying core radii on our results and employ a temperature-damped viscosity equation (Eq. 3.6) as a proxy for a deep LMO scenario in which the magma ocean cumulates do not fully retain their temperature post-overturn.

3.3.1 Shallow Lunar Magma Ocean

For a predominantly chemically homogeneous mantle and no temperature difference across the CMB, heat flow in the lunar mantle is dominated by conduction. As a result, the core heat flux is relatively weak and is below the minimum needed to sustain a dynamo for all of lunar history (Figure 3-2a).

In Figures 3-3d and 3-2d, we observe that a higher CMB temperature difference enhances the CMB heat flux in the first few hundred million years, and exceeds the minimum CMB heat flux within the first 0.01 Gyr. We find a core heat flux above the minimum required for convection cannot be sustained beyond 3.9 Ga, which is too young to produce a dynamo recorded by lunar samples at 3.56 Ga (79). As expected from Eq. (3.8), the increased CMB temperature difference results in a greater intensity for the magnetic field at the surface: 2.5 μT and 3.2 μT, for 100 K and 200 K CMB temperature differences, respectively.

Shallow LMO: Water

When water is relatively enriched in a layer above the CMB, the lower viscosity layer promotes convection, resulting in a higher CMB heat flux and a lower core temperature (Figure 3-3b,c). In this case, the upper mantle remains in a conductive heat transport regime, while the mantle below 600 km convects for up to 0.8 Gyr.

In Figure 3-3, we show the CMB heat flux alongside the temperature difference of water-enrichment models relative to the unenriched case. In cases with water enrichment, we illustrate the efficiency in which heat is removed relative to the nominal unenriched case by plotting the temperature difference with depth (e.g. Figure 3-3b, c)

As shown in Figures 3-2a-c, in the case of no initial temperature difference across the CMB, the addition of a water-enriched region above the core yields a CMB heat flux incapable of sustaining a core dynamo for much of lunar history. Nevertheless, we find the core dynamo may be prolonged with ΔT_{cmb}= 200 K. For a value of ΔT_{cmb}= 200 K, for 40 ppm water in 250-km and 500-km layers above the core, the CMB heat flux is capable of sustaining a core dynamo lasting from 0.1-0.5 Gyr (Table 3.4). However, water restricted to a 250-km layer above the core allows for a reactivated core dynamo between 0.7-0.9 Gyr. Although increased water concentrations may increase the duration of a core dynamo, the maximum magnetic field intensity is not increased more than 0.4 μT at the surface.

3.3.2 Deep Lunar Magma Ocean

With the post-overturn deep LMO and ΔT_{cmb} = 0 K, the initial mantle has a non-monotonic, radial temperature profile (Figure 3-1) with cold layers of magma ocean cumulates, formerly near the surface, embedded in warmer areas of the lower mantle. After approximately 1.8 Gyr, the cold layers are heated by a combination of conduction and minimal convection. The heating of the sequestered cold layer allows for a delayed core dynamo to begin within 0.4 Gyr after model initialization. Within the first few million years, the crust conductively removes the excess heat from the overturn and approaches a steady-state

thermal profile.

For these chemically-heterogeneous LMO cases, the upper- and mid- mantle maintain a conductive heat transport regime, while periodic and sluggish lower mantle convection may persist for the first 0.6 Gyr (Figure 3-4). As shown in Figure3-5d, this case has a slightly lower CMB temperature than the shallow LMO scenario with core heat removed via convection at the top of the core. While the layer below the sequestered cold layer convects, the cold layer is inhibited from participating in convection due to its higher viscosity. Unlike the shallow LMO scenario, a larger thermal gradient at depth can be maintained due to the sequestered cold layer. This thermodynamical behavior enables a mantle without water enrichment to sustain a CMB heat flux within the core dynamo regime for approximately 1.5-2 Gyr (Figure 3-5d).

For increases in ΔT_{cmb}, the initiation of a core dynamo is accelerated by the earlier onset of lower mantle convection and continues through 2.4 Ga (Table 3.5). Given the more vigorous convection catalyzed by the higher ΔT_{cmb}, the final core temperature is decreased as ΔT_{cmb} increases. Furthermore, when $\Delta T_{cmb} = 200$K, a core dynamo is capable of producing a maximum magnetic field intensity of 3.5 μT at the surface.

In summary, for a deep LMO without a water-enriched lower mantle, we find that the core heat flux condition for a convective core dynamo can be met until 2.4 Ga.

Deep LMO: Water

By incorporating water within the deep lunar interior through a reduction in viscosity, the lower lunar mantle more readily sustains a separate convective layer from the remainder of the lunar mantle (Figure 3-4 g-i). We analyze scenarios containing 20 ± 10 wt. ppm (factor of 10 viscosity reduction) and 40 ± 20 wt. ppm (factor of 100 viscosity reduction), within layers of 100 km, 250 km, and 500 km above the CMB. To gauge the effect of water content in the deep interior, we examine model cases relative to the unenriched wet mantle case, alongside varying CMB temperature boundary conditions.

Generally, the result of a lower mantle with a relative enrichment in water is a layer of

reduced viscosity above the core that convects heat away from the CMB into a sluggishly-convecting or conducting overlying mantle. A relative enrichment of water enables heat to be transported out of the core at an increased rate, catalyzed by the sequestered cold-mantle layer. The effect of water has a potent effect on paleointensities for no CMB temperature difference, as observed by the 1.3 μT increase in the magnetic field strength for a 250-km-thick, water-enriched layer (Table 3.5) (although water enrichment generally shortens the core dynamo timespan due to the more rapid heat loss from the core).

For 40 ppm water in 250-km and 500-km layers above the core, the CMB heat flux generally allows a core dynamo to be active within 0.01 Gyr of the beginning of the model (Table 3.4) and lasting until 2.9-2.4 Ga, depending on the initial ΔT_{cmb}. These cases all produce a high heat flux after 3.6 Ga, encompassing the possible high lunar magnetic era of (101). However, water at the same concentration, restricted to a 100-km layer above the core has a negligible effect on the heat flux.

Temperature-Damped Convection

We re-examine the deep LMO scenario for 350-km and 450-km core radii, this time using the temperature-damped viscosity equation (Equation 3.6). For a post-overturn temperature profile, the upper- and mid-mantle remain in the conductive heat transport regime, with minimal lower mantle convection for the first 0.3 Gyr (Figure 3-1) occurring in the lower mantle. As for our standard deep LMO scenario, the sequestered cold layer persists throughout the possible core dynamo era. As a consequence of the temperature dampening, the sequestered cold layer is able to participate in convection, leading to a major upwelling and CMB heat flux peak occurring around $\sim$0.25 Gyr.

When water is enriched in a layer above the CMB, heat is removed with a greater efficiency, resulting in a higher CMB heat flux and a lower final core temperature. For 40 ppm water in 250-km and 500-km layers above the core, the CMB heat flux is capable of sustaining a core dynamo within the first 0.1 Gyr (Figure 3-7), but may reduce the lifetime of a core dynamo by 0.5 Ga. In all but one case, increasing the temperature difference across the

CMB reduces the end time of the core dynamo era by ~0.2 Gyr while generally producing higher heat fluxes and hence stronger magnetic fields.

Relative to the nominal deep LMO scenarios presented earlier, the temperature-damped cases allow for the mantle to transfer more heat earlier in lunar history, constraining the end time for a possible dynamo era to ~3.3 Ga. Contrary to the undamped case for a deep LMO with a 350-km core radius, the addition of a water enriched layer can substantially increase the maximum surface intensity of the magnetic field by up to 40% to 5.1 μT for a 200 K CMB temperature difference.

For an increased core radius of 450 km, the CMB heat flux for an unenriched water case is negligibly affected (Figure 3-7) while for the 250-km water-enriched layer case CMB heat flux peak locations and amplitudes vary. The greater variance in heat flux of the water-enriched case is due to the increase in total water content volume resulting from a larger core radius. The larger core radius shifts the top and bottom of the water-enriched layer to a larger radius; so for a constant layer thickness, we have a larger overall volume for the water-enriched layer. While the heat flux variance is minimal, the 450-km core size results in stronger surface magnetic fields by a factor of 2-3.5 relative to the 350-km core case. The increased magnetic field intensities are primarily a result of the increased core radius (see Eq. 3.8), and demonstrate that the size of the core is a critical factor determining the maximum field strength observed at the lunar surface. This result derives from the fact that the surface field intensity scales as the cube of the ratio of core radius to the lunar radius.

3.4 Discussion

The recent re-analyses of Apollo-era samples for remnant magnetization have likely identified the existence of an internally-generated field on the Moon between ~4.2 and 3.56 Ga (78). The existence of such a field produced by a lunar core dynamo has been thought to be untenable for convective core dynamos, with heat fluxes at the CMB unable to sustain a heat flux in excess of the adiabat beyond 4.0 Ga. Homogeneous models of the lunar mantle,

as an approximation of a shallow LMO predominantly transport heat by conduction after approximately 4.0 Ga (Figure 3-1). For the Moon, these models consistently result in large CMB heat fluxes within the first few hundred million years and near-zero fluxes for the remainder of lunar history, generally independent of most model parameters. The addition of water has two main effects: it may change the duration of a dynamo for a homogeneous mantle by up to 150 Ma, and in the lower mantle it provides a mechanism to enhance the amount of heat advected away from the core, possibly strengthening the dynamo field intensity.

Our heterogeneous model of the lunar mantle is capable of producing a CMB heat flux above the core adiabat for 2.0 Gyr. The initial thermal profile retains the pre-overturn temperature with cold layers of mantle, formerly near the surface, embedded in warmer areas of the lower mantle. Whether gravitational-driven overturn of the LMO can occur while retaining the pre-overturn temperature of the cumulates depends on the layer thickness, start time and duration of overturn. Our analysis of the case in which the temperature is fully retained shows that after approximately 1.8 Gyr, the cold layers are heated by a combination of conduction and sluggish convection, which helps to stimulate convection in the lower mantle. The heating of the deeper, colder layers allows for a delayed core dynamo to begin at approximately 0.3 Ga after magma ocean solidification.

If the LMO overturn is complete by 4.5 Ga, this scenario would be consistent with the earliest recorded magnetic field in the 4.2 Ga troctolite (76). Without water enrichment, this scenario also allows for the possibility that a core dynamo existed for 2.0 Gyr, which may still be consistent with Apollo era paleomagnetic data given that such a weak field would likely be below the detectable threshold (102). If the temperature dependence of viscosity is damped to simulate a scenario in which the thermal gradient in the overturned mantle is partially muted compared to our nominal post-LMO cases, our convective dynamo persists until 3.4 Ga.

Analysis of the electrical conductivity of the Moon suggests a reduced viscosity layer above the core-mantle boundary consistent with an enriched-wet region of approximately 100-200 km (103). In examining the role of water on the thermal evolution of the interior, we find

that water enrichment at depth is likely to further decrease the temperature of the lower mantle over time and, depending on the water concentration and regional extent, this may shorten or lengthen the duration of a possible core dynamo by as much as 600 Ma. With a range of density and temperature profiles, the addition of water in the deep interior, we find that water acts as a catalyst for transporting heat out of the deep mantle. By incorporating the temperature dependence of viscosity, this effect is more pronounced and generates a heat flux in most cases exceeding 4 mW/m^2.

We find that water-enriched regions provide a stronger CMB heat flux. Using Eq. 3.8, an upper limit for the magnetic field intensity can be produced from our core heat flux. For a deep LMO case with 40±20 ppm water at 500 km above a 350-km core, the heat flux could promote a 5-μT magnetic field at the surface, compared with up to 3.5 μT in cases without water enrichment. Further, we find varying the core radius (see Eq. 3.8) results in a minimal change to the core heat flux, but causes substantial changes in the surface magnetic field strength.

With the exception of a KREEP layer at the near surface, our temperatures do not exceed the bulk solidus and thus melt quantities are neglected. For larger quantities of melt, the partitioning of water and the amount of melt will play dominant roles in determining whether a viscosity reduction or increase is likely for melt under hydrous conditions (94). The very-low-Ti glasses recently discovered to contain water are theorized to originate from a heterogeneous mantle source, including a KREEP component, at less than 520-km depth (65; 64; 104; 105). If only a small amount of KREEP was retained near the surface, the remainder along with its radioactive element and water content may have foundered with a dense layer of cumulates below. Given our results, it is likely that under these circumstances, water could have played an influential role in promoting a higher CMB heat flux and could have promoted core dynamo activity beyond 3.7 Ga.

Although our shallow LMO cases are unable to sustain the minimum CMB heat flux beyond 3.7 Ga, we note that a growing solid inner core is likely to reduce the minimum CMB heat flux necessary to main a superadiabatic liquid outer core (106; 100), thus potentially allowing a chemically homogeneous mantle to sustain a core dynamo. In general, these

shallow LMO cases illustrate that water enrichment above the CMB promotes a stronger, higher CMB heat flux, extending a lunar core dynamo period by up to 150 Ma.

3.5 Summary

A homogeneous, dry model of the lunar mantle is biased to predominantly conduction after approximately 4.0 Ga, after which time it is generally unable to support a convective core dynamo without external mediation of a thermal blanket (81), impact-induced rotation changes (82), or, as we show in this study, the addition of mantle water. For the Moon, these models tend to result in large CMB heat fluxes within the first few hundred million years, and very low fluxes for the rest of lunar history, consistent with prior models (98; 81). We find that a deep lunar magma ocean after gravitationally driven overturn may sustain a core dynamo on timescales longer than the latest paleomagnetic data (78; 79), through 2.4 Ga. Based on the core dynamo scaling model of (97) for a 350-km core radius, our results yield a maximum magnetic field intensity of 3.5 μT without water enrichment and 5.1 μT with water enrichment. Additionally, we find that the observed maximum magnetic field strength at the surface is strongly dependent on the lunar core radius. For the homogeneous and heterogeneous mantle cases, enriched water in the lower mantle acts as a catalyst for transporting heat out of the deep mantle due to the reduced viscosity from protonic weakening (85). If water was transported or retained preferentially in the deep interior, even in small amounts ($\leq$20 ppm), it would have played a significant role in transporting heat out of the deep interior and reducing the lower mantle temperature. Water enriched in the lower mantle could have influenced the timing by up to 1.0 Gyr and enhanced the vigor of a lunar core dynamo.

3.6 Acknowledgements

I thank Linda Elkins-Tanton for temperature and density data provided for a post-overturn lunar magma ocean, Shijie Zhong for assistance in the Citcom2D thermal evolution model,

and Benjamin Weiss for assistance and comments. This work was supported by the NASA Lunar Science Institute and a NASA Lunar Advanced Science and Exploration Research grant to BPW.

3.7 Figures

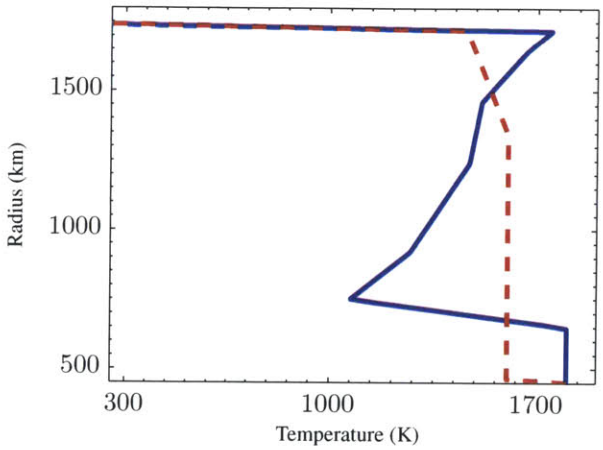

Figure 3-1: Initial temperature and density profiles used in our convective models with $\Delta T_{cmb} = 200$ K. Shown is the temperature profile of the deep LMO scenario (blue solid line) as determined by (1) compared to the shallow LMO (red dashed line).

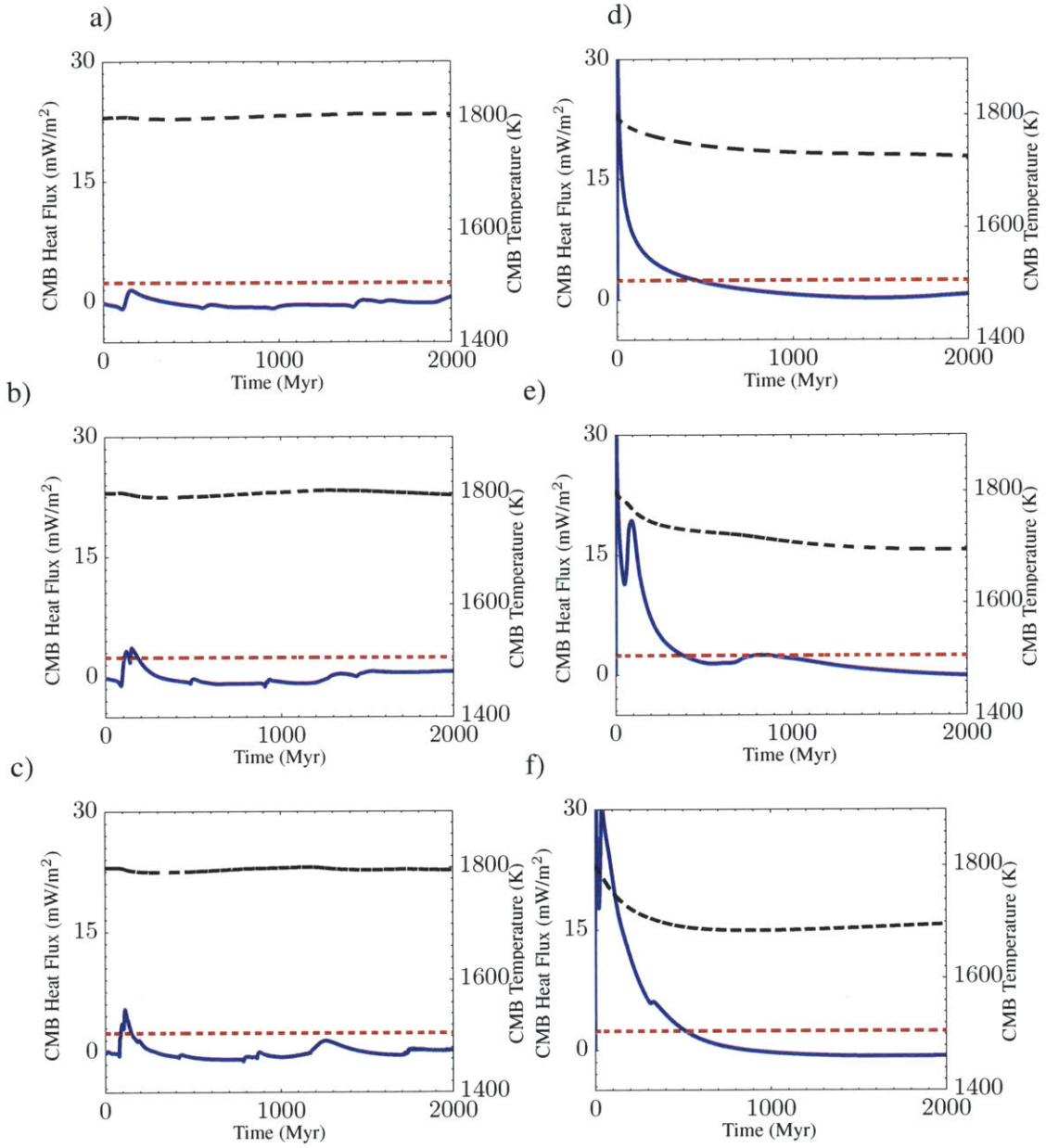

Figure 3-2: CMB heat fluxes for shallow lunar magma ocean model. The CMB heat flux (blue solid line) is shown on the left axis with the minimum heat flux needed to sustain a core dynamo (red dash-dot line) and the core temperature (black dashed line) on the right axis. (a, b, c) Models with ($\Delta T_{cmb} = 0$ K). (d, e, f) Models with $\Delta T_{cmb} = 200$ K. (a) Case ZXX01: No Water Enrichment, (b) case ZXX02: 200-km water-enriched layer with 40$\pm$20 ppm water, (c) Case ZXX03: 500-km water-enriched layer with 40$\pm$20 ppm water, (d) Case ZXX25: No Water Enrichment, and (e) Case ZXX26: 200-km water-enriched.

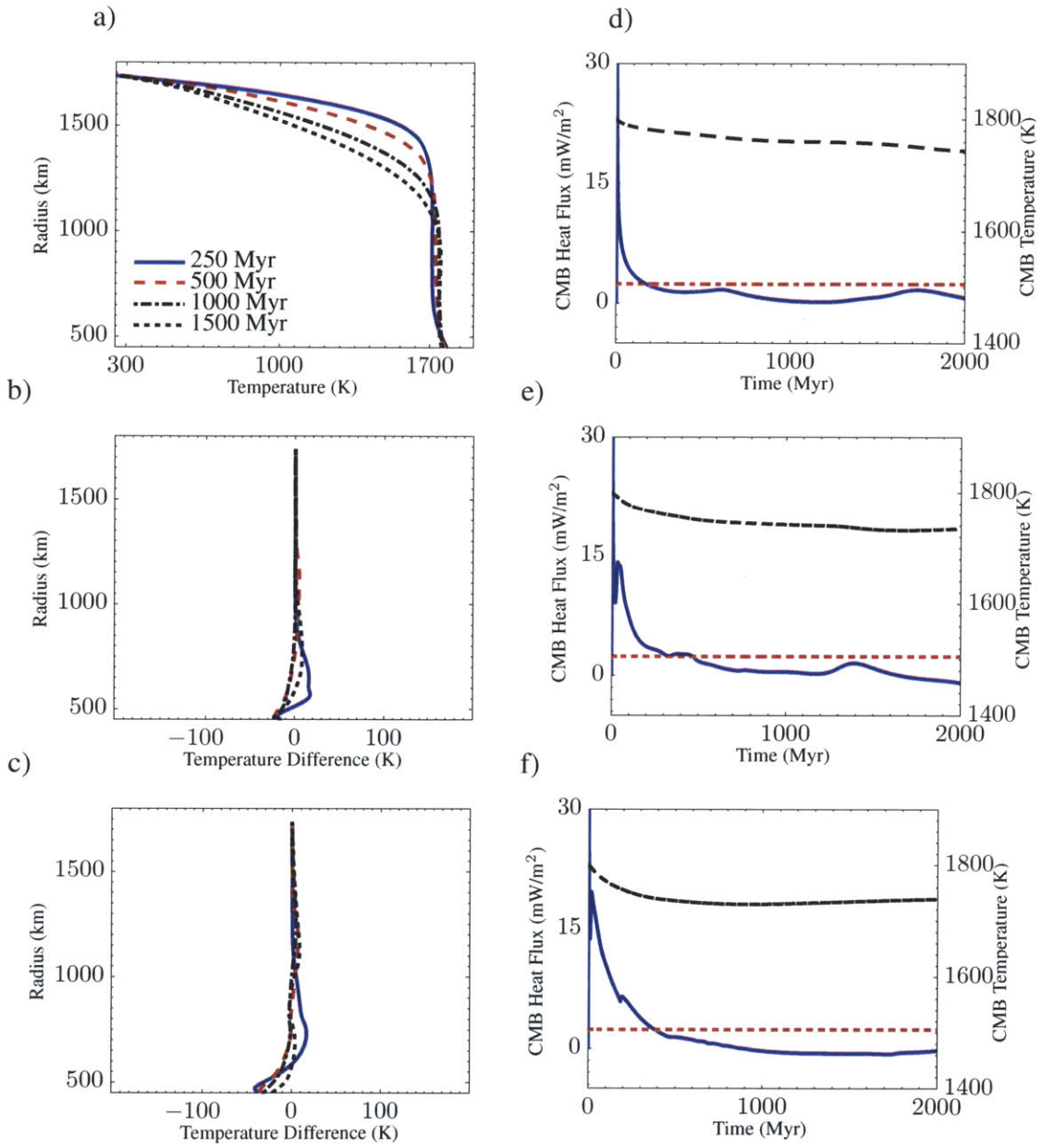

Figure 3-3: Temperatures and CMB heat fluxes for shallow lunar magma ocean model with $\Delta T_{cmb} = 100$K. (a,d) Case ZXX25: No Water Enrichment, (b,e) Case ZXX26: 200-km water-enriched layer with 40±20 ppm water, and (c,f) Case ZXX27: 500-km water-enriched layer with 40±20 ppm water. (b, c) Mantle temperature differences relative to the non water-enriched scenario for water-enriched models. In (d,e,f) CMB Heat Flux (blue solid line) as a function of model start time is shown on the left axis with the minimum heat flux needed to sustain a core dynamo (red dash-dot line) and the core temperature (black dashed line) on the right axis.

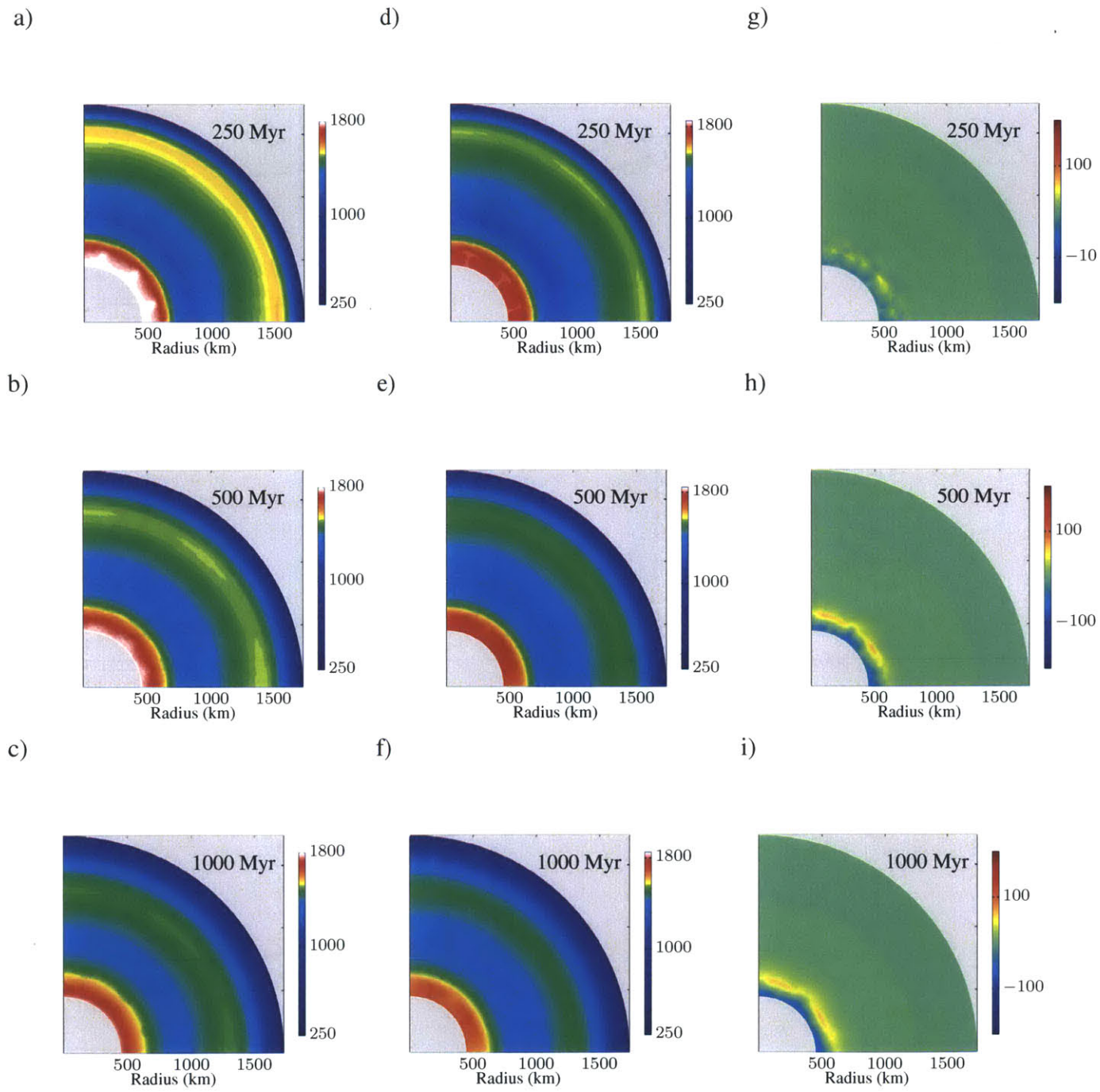

Figure 3-4: Half-Hemisphere temperature view of the lunar mantle model. ΔT_{cmb} = 0 K. Shown are lunar interior panels with pseudocolor temperature (K) at 0.25, 0.50, and 1.0 Gyr after model initialization. a, b, c) Case VXX07 (no water enrichment). (d, e, f) ase VXX08 (200-km water-enriched layer with 40±20 ppm water). (g, h, i) Temperature difference between cases VXX08 and VXX07, highlighting the increased convection vigor of the water-rich layer. The radial average of the temperature difference with time is shown in Figure 3-5b.

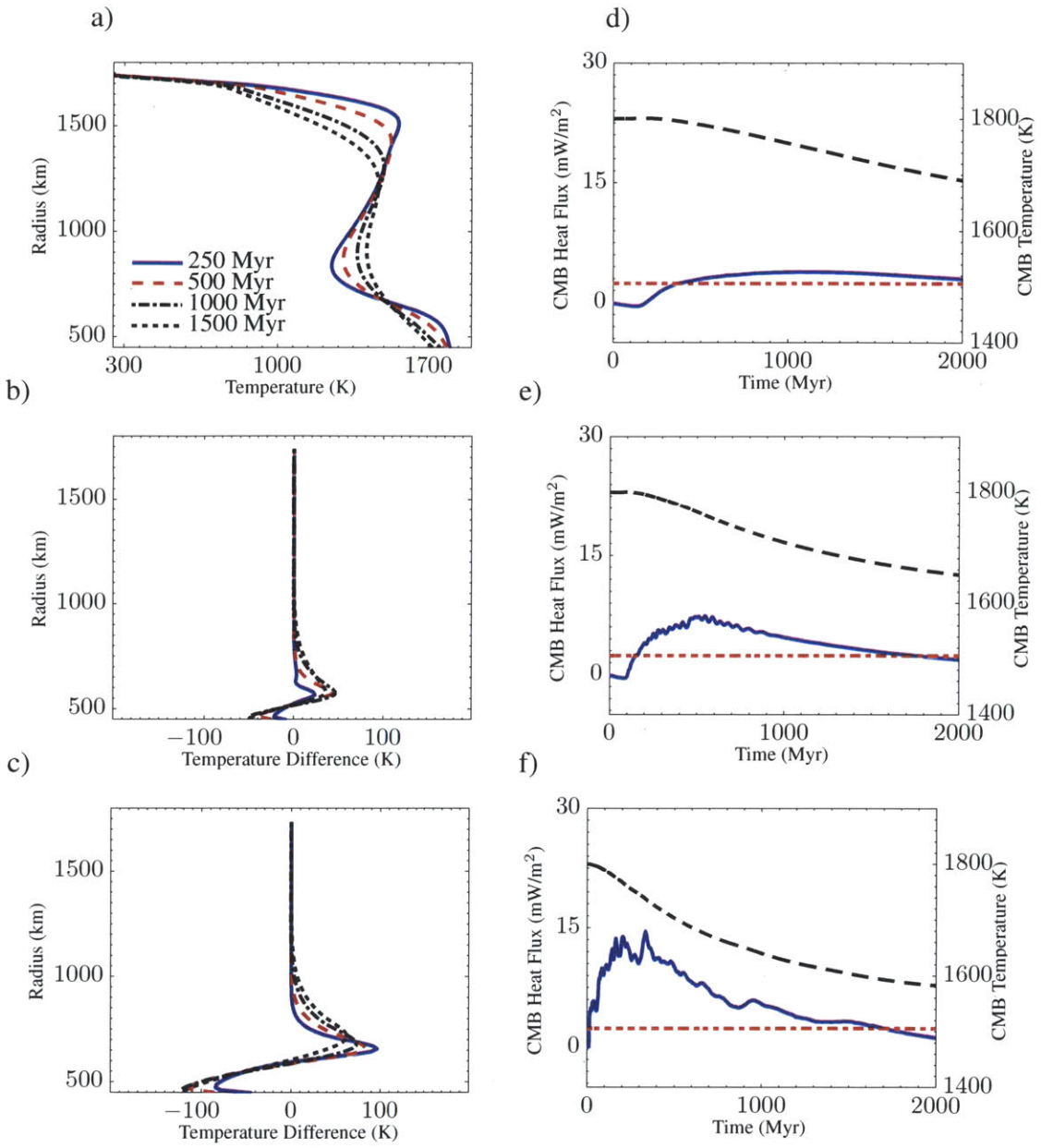

Figure 3-5: Temperatures and heat fluxes for deep lunar magma ocean model with ΔT_{cmb} = 0 K. (a,d) Case VXX07: No Water Enrichment, (b,e) Case VXX08: 200-km water-enriched layer with 40±20 ppm water, (c,f) Case VXX09: 500-km water-enriched layer with 40±20 ppm water, The radially-averaged temperature in time is shown for Case ZXX01 in panel (a) with panels (b,c) tracking the temperature differences with time relative to Case VXX07. In (d, e, f), the CMB heat flux (blue solid line) is shown on the left axis with the minimum heat flux needed to sustain a core dynamo (red dash-dot line) and the core temperature (black dashed line) on the right axis.

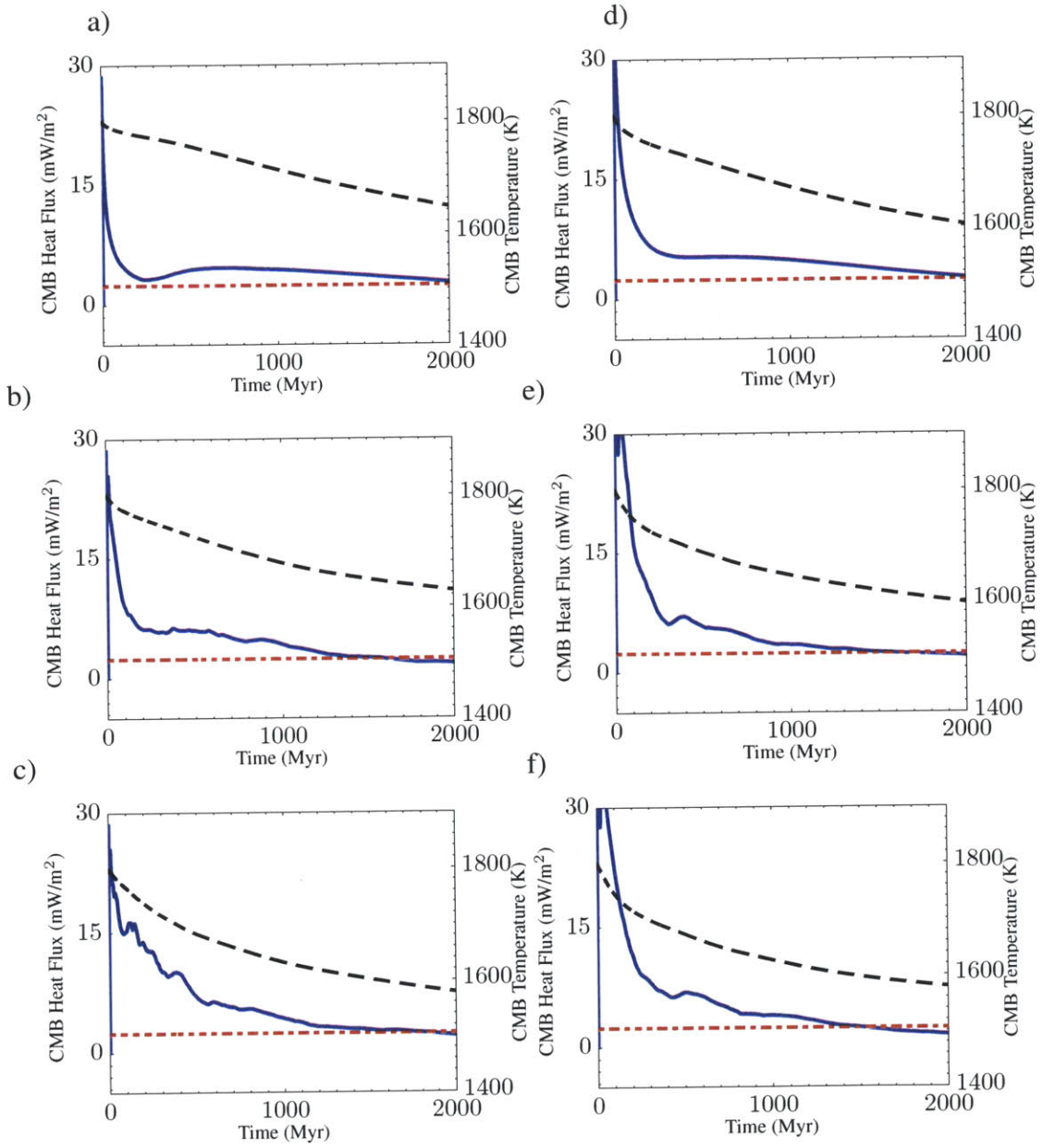

Figure 3-6: CMB heat fluxes for deep lunar magma ocean model. The CMB heat flux (blue solid line) is shown on the left axis with the minimum heat flux needed to sustain a core dynamo (red dash-dot line) and the core temperature (black dashed line) on the right axis. (a, b, c) Models with (ΔT_{cmb} = 100K) Case VXX37: No Water Enrichment, Case VXX38: 200-km water-enriched layer with 40±20 ppm water, and Case VXX39: 500-km water-enriched layer with 40±20 ppm water, respectively. (d, e, f) Models with (ΔT_{cmb} = 200K) Case VX43: No Water Enrichment, Case VX44: 200-km water-enriched layer with 40±20 ppm water, and Case VX45: 500-km water-enriched layer with 40±20 ppm water.

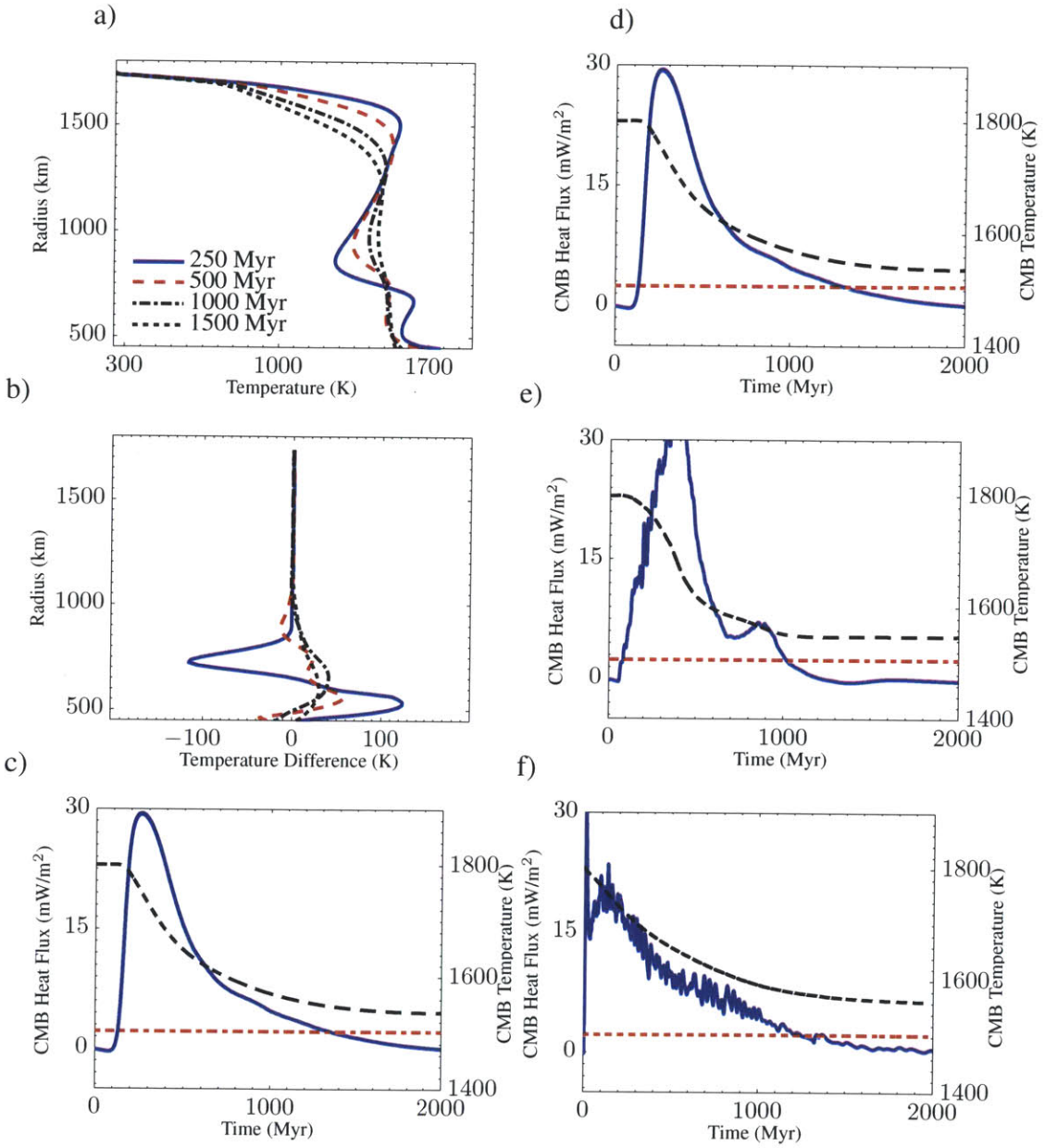

Figure 3-7: Temperatures and CMB heat fluxes for case for the temperature-damped, deep lunar magma ocean model with $\Delta T_{cmb} = 0$ K. (a,d) Case VXX13: 350-km core radius and no water enrichment, (b,e) Case VXX14: 350-km core radius and 200-km water-enriched layer with 40±20 ppm water, (c) Case VX13: 450-km core radius and no water enrichment, (f) Case VX14: 450-km core radius and 200-km water-enriched layer with 40±20 ppm water. The temperature evolution in model time is shown with radius for Case VXX13 in panel (a) with panel (b) showing the temperature difference of Case VXX14 at the same time relative to Case VXX13. In c-f the CMB heat flux (blue solid line) is shown on the left axis with the minimum heat flux needed to sustain a core dynamo (red dash-dot line) and the core temperature (black dashed line) on the right axis.

3.8 Tables

Table 3.1: Parameter Values for Convection Model

Parameter	Value
Activation Energy, E	5.0×10^5 J mol^{-1}
Activation Volume, V	1.5×10^{-6} m^3 mol^{-1}
Core Density, ρ_{core}	7400 kg m^{-3}
Core Radius, R_c	350 km
Core Conductivity, k_{core}	25-40 W/(m-K)
Core Heat Capacity, $c_{p,\text{core}}$	800 J/K
Core Temperature, T_c	1800 K
Core Thermal Expansivity, α_c	5.85×10^{-5}
Heat Capacity, $c_{p,\text{mantle}}$	1200 J/K
Mean Planetary Radius, R_p	1737 km
Rayleigh number, Ra	1.2×10^7
Thermal Diffusivity, κ	1.0×10^{-6} m^2 s^{-1}
Thermal Expansivity, α	3.0×10^{-5}
Shear Modulus, μ	5×10^{10} N m^{-2}
Surface Gravity, g	1.63 m s^{-2}
Viscosity, Maximum Variation	10^9
Viscosity, Minimum Variation	10^{-2}
Viscosity Reference, η_0	10^{20} Pa s
Surface Temperature, T_s	250 K

Table 3.2: Parameter Values for the Radioactive Content

Parameter	Value
KREEP Uranium Concentration	3.4 p.p.m.
Mantle Uranium Concentration	6.8 p.p.b.
Thorium/Uranium Ratio	3.7
Potassium/Uranium Ratio	2500

[a]Refers to layer height above CMB

Table 3.3: Parameter Values for Magnetic Field Intensity

Parameter	Value
Ratio of ohmic to total dissipation, f_{ohm}	1
Constant of proportionality, c	0.63
Magnetic permeability of free space, μ_o	1.26×10^{-6}

Table 3.4: Shallow Lunar Magma Ocean: CMB Heat Fluxes.

Scenario	Input Parameters			Dynamo Regime		Maximum Surface
	CMB ΔT (K)	Water Layer[a](km)	A_H	Begin (My)	End (My)	Field Intensity (μT)
ZXX01	0	0	1	-	-	-
ZXX02	0	250	10^{-2}	100	190	1.3
ZXX03	0	500	10^{-2}	90	150	1.6
ZXX04	0	100	10^{-2}	-	-	-
ZXX05	0	500	10^{-1}	100	150	1.2
ZXX06	0	100	10^{-1}	-	-	-
ZXX25	100	0	1	0	180	2.5
ZXX26	100	250	10^{-2}	0	470	2.6
ZXX27	100	500	10^{-2}	0	390	2.9
ZXX28	100	100	10^{-2}	0	180	2.5
ZXX29	100	500	10^{-1}	0	390	2.5
ZXX30	100	100	10^{-1}	0	180	2.5
ZXX31	200	0	10^{-2}	0	460	3.2
ZXX32	200	250	10^{-2}	0	410**	3.2
ZXX33	200	500	10^{-2}	0	520	3.5
ZXX34	200	100	10^{-2}	0	460	3.2
ZXX35	200	500	10^{-1}	0	690	3.2
ZXX36	200	100	10^{-1}	0	460	3.2

Table 3.5: Deep Lunar Magma Ocean: CMB Heat Fluxes.

Scenario	Input Parameters			Dynamo Regime		Maximum Surface
	CMB ΔT (K)	Water Layer (km)	A_H	Begin (My)	End (My)	Field Intensity (μT)
VXX07	0	0	1	370	2000*	1.3
VXX08	0	250	10^{-2}	150	1800	1.9
VXX09	0	500	10^{-2}	10	1710	2.6
VXX10	0	100	10^{-2}	370	2000	1.3
VXX11	0	500	10^{-1}	70	1790	1.9
VXX12	0	100	10^{-1}	370	2000	1.3
VXX37	100	0	1	0	2000*	2.7
VXX38	100	250	10^{-2}	0	1630	3.2
VXX39	100	500	10^{-2}	0	1850	3.2
VXX40	100	100	10^{-2}	0	2000*	2.7
VXX41	100	500	10^{-1}	0	2000*	2.8
VXX42	100	100	10^{-1}	0	2000*	2.7
VXX43	200	0	1	0	2000*	3.5
VXX44	200	250	10^{-2}	0	1720	3.6
VXX45	200	500	10^{-2}	0	1530	3.6
VXX46	200	100	10^{-2}	0	2000*	3.5
VXX47	200	500	10^{-1}	0	2000*	3.5
VXX48	200	100	10^{-1}	0	2000*	3.5

Table 3.6: Temperature-Damped Viscosity: CMB Heat Fluxes.

Scenario	Input Parameters				Dynamo Regime		Maximum Surface
	Core Radius (km)	CMB ΔT (K)	Water Layer (km)	A_H	Begin (My)	End (My)	Field Intensity (μT)
VXX13	350	0	0	1	130	1330	3.4
VXX14	350	0	250	10^{-2}	80	1020	4.0
VXX15	350	0	500	10^{-2}	0	870	4.2
VXX16	350	0	100	10^{-2}	130	1330	3.4
VXX17	350	0	500	10^{-1}	20	1080	3.9
VXX18	350	0	100	10^{-1}	130	1330	3.4
VXX49	350	200	0	1	0	1220	3.5
VXX50	350	200	250	10^{-2}	0	800	4.4
VXX51	350	200	500	10^{-2}	0	810	5.1
VXX52	350	200	100	10^{-2}	0	1220	3.5
VXX53	350	200	500	10^{-1}	0	780	4.5
VXX54	350	200	100	10^{-1}	0	1220	3.5
VX13	450	0	0	1	130	1240	8.4
VX14	450	0	250	10^{-2}	0	1170	8.4
VX15	450	0	500	10^{-2}	0	680	15.0
VX16	450	0	100	10^{-2}	70	920	10.1
VX17	450	0	500	10^{-1}	20	840	11.4
VX18	450	0	100	10^{-1}	90	1150	8.3
VX49	450	200	0	1	0	1120	8.8
VX50	450	200	250	10^{-2}	0	1000	11.6
VX51	450	200	500	10^{-2}	0	650	15.3
VX52	450	200	100	10^{-2}	0	1010	10.9
VX53	450	200	500	10^{-1}	0	820	12.5
VX54	450	200	100	10^{-1}	0	1020	9.2

[a]* The dynamo regime is still active at this time.

[a]** The CMB heat flux enters the dynamo regime for approximately 0.1 Gyr near 0.8 Gyr after model initialization.

Chapter 4

A Wet Lunar Mantle: Basin Modification

4.1 Introduction

As mentioned in the previous chapter, during the final stages of fractional crystallization from a lunar magma ocean, the last dregs of the melt would be enriched in water and incompatible elements, subsequently crystallizing beneath the anorthositic crustal lid (60; 61). Thus, a post-magma ocean Moon would contain a sub-crustal water-rich reservoir ($\geq$260 ppm) (65) and may have influenced the expression of surface features such as impact basins.

Similarly-sized lunar basins exhibit a predictable trend in the depth-to-diameter ratios, with older basins revealing shallower topographic profiles than their younger counterparts (107). Given the predicted high temperatures for the early Moon (108; 1), it is expected viscoelastic relaxation more pervasively influenced the evolution of the impact basin topography in early lunar history, such as Transquilitatis and South Pole-Aitken basins (109), and may have been enhanced by near-surface water reservoirs.

In this study, we address the influence of water on lunar evolution by incorporating an attenuating strain rate (i.e. decreased viscosity) (64; 71; 85) for potential wet regions in

the lunar interior. From experimental studies of the Earth's upper mantle (300 MPa), the presence small amounts of water (20 wt ppm) can result in a viscosity reduction by a factor in excess of 100 Pa-s (71; 85). For the near-surface effect of water, we construct profiles for pre-relaxed lunar basins [*Sori & Zuber, in prep.*] and examine the influence of impact heating, dislocation creep, and water on basin evolution through a viscoelastic model of basin loading to provide insight into the lunar thermal history and the existence of near-surface water reservoirs.

4.2 Methodology

4.2.1 Impact Heating & Initial Basin State

A projectile impacting a planetary surface initially forms a transient crater of diameter, D_{at} which can be related to the final rim diameter, D, by

$$D = 1.32 D_{at}^{1.086} D_{sc}^{-0.086} \tag{4.1}$$

where D_{sc} represents the single-to-complex transition diameter (110), approximately 20 km, as determined by (111). The transient crater diameter from Equation 4.1 is used to determine the impactor diameter in

$$D_p = 1.34 g^{-0.22} v_i^{0.44}, \tag{4.2}$$

derived from (112). For our calculations, we assume a vertical impactor velocity, v_i, of 15 km/s (113).

We can determine the temperature increase from waste heat generated by decompression from a shock state as derived by (114),

$$\Delta T_s(P_\delta) = \frac{P_\delta}{2\rho_0 S C_p}\left(1 - f^{-1}\right) - \frac{C^2}{S^2}(f - \ln f - 1) \tag{4.3}$$

$$f(P_\delta) = -\frac{2P_\delta S}{C^2\rho_0}\left(1 - \sqrt{\frac{4P_\delta S}{C^2\rho_0} + 1}\right)^{-1} \tag{4.4}$$

where P_δ is the peak shock pressure, P_s, less the initial static pressure, P_0. Since our estimates of impact heating are near the surface, we assume P_δ=P_s. Table 4.1 contains the values for constants employed in the above equations.

Within the isobaric core at depth $d_c = R(10^{a_2})v_i^{b_2}$ and radius, $r_c = R(10^{a_1})v_i^{b_1}$, the peak shock pressure is equal to P_c, and decays inversely with distance according to the formula (115; 112).

$$P_s = P_c\left(\frac{r_c}{r}\right)^{-1.84+2.61\log v_i} \tag{4.5}$$

where P_c is defined by

$$P_c = \rho_0 u_c\left(C + S u_c\right). \tag{4.6}$$

Per (114), we assume the target and impactor have the same density and the particle velocity of the isobaric core, $u_c = 0.5v_i$. Using improved estimates of depth-to-diameter ratios for impacts basins, we construct profiles for pre-relaxed lunar basins from a power-law extrapolation of 60-200 km basins [*Sori & Zuber, in prep.*]. For simplicity, we assume an initial parabolic depth profile with the maximum depth at the basin center.

4.2.2 Viscoelastic Relaxation

We employ a viscoelastic model (CitcomVE) based on a Citcom2D framework (116; 86; 87; 88) that models incompressible viscoelastic and maxwellian mantle dynamics. We

use the following governing equations of the conservation of mass and momentum, and gravitational perturbation (117) in addition to the rheological equation,

$$u_{i,i} = 0, \tag{4.7}$$

$$\sigma_{ij,j} + \rho_0 \phi_{,j} - \rho_1 g_i - \rho_o |g| u_{i,j}\, \delta_{ir} = 0, \tag{4.8}$$

$$\phi_{,ii} = -4\pi G \rho_1, and \tag{4.9}$$

$$\sigma_{ij} + \frac{\eta}{\mu}\dot{\sigma}_{ij} = -\left(P + \frac{\eta}{\mu}\dot{P}\right)\delta_{ij} + \eta(r,T)\left(u_{i,j} + u_{j,i}\right). \tag{4.10}$$

where P is the dynamic pressure, Ra is the Rayleigh number referenced to the lunar radius, T is the temperature, and $\vec{n}_r$ is normal vector in the radial direction. We use the temperature and viscosity from our convection model in Chapter 3. The above equations use Einstein notation to indicate summation over repeated indices, with a subscript comma denoting the derivative with respect to the following spatial index.

4.3 Observations & Constraints

The cooling history of the moon is still ambiguous, though there is some evidence, including recovered lunar alkalic igneous rocks, which suggest a late rapid cooling scenario for the shallow part of the moon, which may have been preceded, or overlapped, with a slow cooling phase of the deep moon (54; 83; 84). The impact basins, which dominate the lunar terrain through the Late Imbrian (107), can provide constraints on the thermal history, but require an understanding of the role of impact heating, rheology, local radioactive heating and water concentration, and subsequent modification mechanisms (e.g. (118; 119)).

4.4 Shallow Upper Mantle Water & Basin Relaxation

The existence of a water-enriched near-surface layer is predicted by the lunar magma ocean model (67). Water, would be enriched, with the incompatible elements forming a wet, radiogenically-enhanced layer (urKREEP) beneath the lunar crust (70; 61). It has been hypothesized that the layer, all or in part, may have foundered and or mixed with the other cumulates during the suspected overturn of the lunar magma ocean (120; 81). The existence of the PKT (Procellarum KREEP Terrane) on the lunar surface suggests that a urKREEP layer, possibly mixed with other cumulates, existed near the surface post-overturn (70). Herein, we investigate the influence of viscoelastic relaxation of basins, incorporating the effects of impact heating, KREEP, and water and using the Mendel-Rydberg basin for our scenarios.

The very-low-Ti glasses discovered to contain water are theorized to come from a heterogeneous mantle source, including a urKREEP component, at less than 520-km depth (65; 64; 104; 105). This suggests that there still exists some of the original urKREEP layer in the upper mantle. Our results on basin relaxation indicate a near-surface source of water-enriched, urKREEP, would have a substantial effect on the final topographic profile of a lunar basin. Unless only a small amount of urKREEP remains near the surface, the radiogenic content and water concentration would need to be determined in order to deduce any relevant information on the thermal state from the geomorphic properties of lunar basins. As determined by our results, the influence of water at the near-surface aids in viscoelastic basin relaxation and has an increasing effect with increasing radiogenic content.

4.5 Results & Discussion

We use representative lunar density and temperature profiles and evolve temperature based on Chapter 3 from the time of impact until the present. The water content is represented as a region of reduced viscosity, and radioactive heat generation is included via a thin 20-km KREEP layer containing radioactive element concentrations. Our temperature- and depth-

dependent rheology is referenced to a viscosity of 10^{20} Pa-s with a maximum viscosity variation of 10^{9} Pa-s. With the pre-relaxed basin diameter, we estimate the impact heating based on the shock-increased pressure as derived in our methodology. As our baseline, we use a dry mantle with uniform material properties and no KREEP. Within the first few million years, the crust conductively cools the excess heat from the overturn and approaches a steady-state thermal profile. We compare basins formed at 0.1, 0.3, 0.7 and 1.0 Gyr.

4.5.1 Near-Surface KREEP Layer

The inclusion of a sub-crustal layer of KREEP on the Moon may have important implications for the viscoelastic relaxation of basins. We apply temperature profiles from our convection model (Chapter 3) with varying KREEP content to determine the effect on basin relaxation. Figure 4-1 shows the present-day basin depth as a function of basin formation age. We find that for a near-surface concentration of KREEP, basin relaxation is enhanced by 10% at 100 Myr and up to 30% at 1 Gyr.

4.5.2 KREEP Component & Water

The existence of a sub-crustal KREEP layer is predicted by the lunar magma ocean model and is expected to be commensurate with an enriched zone of water. We examine the effect of water on the relaxation of basin topography by incorporating a 45-km wet layer of mantle, a minimum chosen based on numerical limitations, at a originating depth of 1670 km and 1690 km. Our results are shown in Figure 2 and indicate that a water layer commensurate with KREEP at 100 Myr increases the relaxation by over 20%, and is diminished in the absence of KREEP, yielding an increase of relaxation by less than 10%. The effect of a water layer is increasingly diminished with later impacts shown in Figure 4-2.

4.6 Summary

A water-enriched KREEP layer that retains a non-negligible portion of radioactive material, could increase the relaxation of basins in excess of 30%. Water alone will produce non-negligible increases in relaxation through 0.3 Gyr in the absence of KREEP and is extended through 0.7 Gyr in the presence of a KREEP layer, with a 50% reduction in nominal radioactive concentration(61). These results elucidate the role of KREEP and water on basin relaxation history and suggest that basins formed in the early history of the Moon could have been significantly influenced by the presence of KREEP and or water. Further, the KREEP terrane on the moon is likely to have basins that have had greater relaxation if formed early in lunar history. These results may help constrain the timing of lunar basins as well as the thermal and evolution of the Moon.

4.7 Acknowledgements

I thank Linda Elkins-Tanton for temperature and density data provided for a post-overturn lunar magma ocean, and Shijie Zhong for assistance in the Citcom2D thermal evolution model and CitcomVE viscoelastic model. This work was supported by the NASA Lunar Science Institute.

4.8 Figures

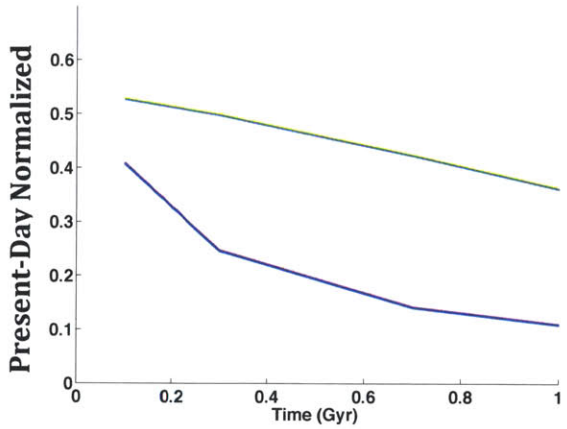

Figure 4-1: Basin Depth Normalized to Initial Basin Center Depth (Cases with varying KREEP content). Present-day depth of basins including the effect of sub-crustal KREEP concentration of 100% (blue) is compared with scenario without a sub-crustal KREEP component (green).

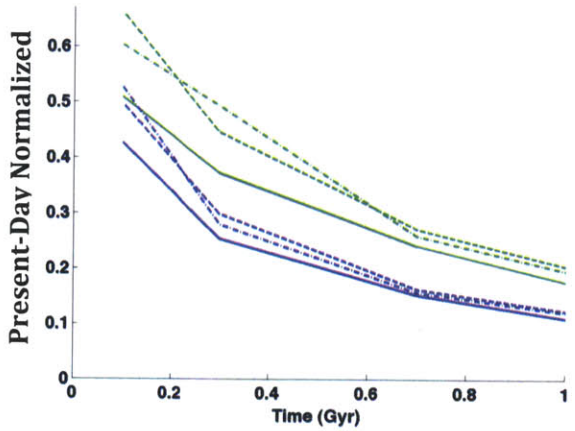

Figure 4-2: Basin Depth Normalized to Initial Basin Center Depth (Cases with Water and KREEP). Present-day depth of basins with water concentrations at varying radial positions of 1690 km (dash-dotted line) and 1670 km (dashed line). The reference (solid lines) are relaxation curves with no water for a sub-crustal KREEP concentration of 50% (green) and with no sub-crustal KREEP (blue).

4.9 Tables

Table 4.1: Parameter Values for Impact Heating & Viscoelastic Relaxation

Parameter	Value
Constant, a	-0.31
Constant, b	1.15
Constant, a_1	-0.346
Constant, a_2	-0.516
Constant, b_1	0.211
Constant, b_2	0.361
Mendel-Rydberg Rim Diameter	635 km
Slope of linear shock, S	1.20
Speed of Sound at STP, C	5.6 km/s
Vertical Projectile Velocity, v_i	15 km/s

Chapter 5

Recovery of Buried Lunar Craters

5.1 Introduction

As a result of its accretionary history, the lack of a substantial atmosphere, and absence of plate tectonics, the Moon is characterized by an extraordinarily well-preserved and mostly ancient surface. With its accessibility to orbital and landed spacecraft that has provided comprehensive global mapping as well as returned surface samples, the Moon has a unique qualitative and quantitative role in understanding and constraining the evolution of our Solar System, as well as the timing of its many major events (e.g. (121)). The contrast of low reflectance material of the lunar nearside maria against the high reflectance, anorthositic highlands crust (107; 122) can be observed from Earth with the naked eye and is one of the most recognizable features of the Moon. Geologic evidence supports the hypothesis that the maria flooded the lunar nearside between 3.8-2.5 Gya, during at least three major events (123). The emplacement of the lunar maria has obscured much of the original physiographic expression of the nearside lowlands, nearly 20% of the entire surface (123; 122), impairing our ability to fully understand this unique lunar region.

Previous workers have attempted to constrain the amount of maria emplaced on the lunar surface using radar and seismic refraction data (124; 125; 126), localized gravity recovery (127), geologic techniques relying on impact-exposed subsurface structure (128; 129), and

estimates based on partially buried (filled) craters (130; 131; 132; 123; 133). Some of these investigations have provided insight into the history, average thickness, and age of the mare flows and are summarized by (134). (135) and (136) suggest that the mare emplacement represents the onset of a secondary crust, an expected outcome of terrestrial, planetary bodies. Studies of basin mare deposits (129; 123) suggest the mare flooding of the eastern lowlands occurred in three phases with an evolving Ti-content. While lenses of basin mare fill have been approximated to be as much as 8.5-km thick (119; 133), the average mare load for the lunar nearside is generally considered to be less than 2 km (130; 131; 132)

.

In this paper, we use gravity data acquired by the dual Gravity Recovery and Interior Laboratory (GRAIL) spacecraft (137; 138; 58)in conjunction with altimetry data from the Lunar Orbiter Laser Altimeter (LOLA) investigation (139; 140) on the Lunar Reconnaissance Orbiter (141) to search for buried craters. We use this crater population in concert with partially buried craters to investigate the average depth, volume, and density of lunar maria that have been emplaced on the lunar nearside.

5.2 Data, Methodology & Modeling

5.2.1 Spherical Harmonic Localization

A real-valued, square-integrable function, $g(\Omega)$, defined on a unit sphere can be expanded as a linear combination of spherical harmonics (25) by

$$g(\Omega) = \sum_{l=0}^{\infty} \sum_{m=-l}^{l} g_{lm} Y_{lm}(\Omega), \tag{5.1}$$

and

$$g_{lm} = \int_{\Omega} g(\Omega) Y_{lm}(\Omega) d\Omega, \tag{5.2}$$

where Ω is the solid angle, Y_{lm} is the spherical harmonic basis function of degree l and order m, and g_{lm} are the corresponding spherical harmonic coefficients.

We apply a method for spatio-spectral localization on a sphere, in which data is localized to a zonal (axisymmetric) polar cap by applying a set of orthogonal spherical harmonic tapers (26; 23). We maximize the energy concentration, λ, to spatially concentrate a zonal band-limited function, $f(\theta)$, within a cap, $0 \leq \theta \leq \theta_0$, such that,

$$\lambda = \frac{\int_0^{2\pi} \int_0^{\theta_0} f(\theta)^2 sin(\theta) d\theta d\phi}{\int_\Omega f(\theta)^2 d\Omega} = \text{maximum}, \tag{5.3}$$

where $0 \leq \lambda \leq 1$. By use of Eq. (5.2), we can rewrite (5.3) as

$$\lambda = \frac{\sum_{l=0}^{L_{win}} f_l \sum_{l'=0}^{L_{win}} D_{l,l'} f_{l'}}{\sum_{l=0}^{L_{win}} f_l^2}, \tag{5.4}$$

where

$$D_{l,l'} = \int_0^{2\pi} \int_0^{\theta_0} Y_l(\theta) Y_{l'}(\theta) sin(\theta)\, d\theta d\phi, \tag{5.5}$$

and L_{win} is the bandwidth of the localization (window). For a square-integrable function expressed in spherical harmonics, its coefficients, g_{lm}, at each degree, l, receives contributions from across the range $l - L_{win} \leq l \leq l + L_{win}$ when localized. The window bandwidth restricts the localization, such that the following inequality holds for all degrees, l_{loc}, of the windowed field, $L_{win} \leq l_{loc} \leq L - L_{win}$, where L is the maximum harmonic degree of the dataset.

Equation (5.4) cam be reduced to a matrix eigenvalue equation where the eigenfunctions of a kernel given by $D_{l,l'}$ are spherical harmonic coefficients of the space-concentrated tapers (26; 22; 23). In full index notation, the reduction is

$$D_{l,l'} f_l = \lambda f_l. \tag{5.6}$$

We use the single, most optimally concentrated eigenfunction to localize the region per the method of (23).

5.2.2 Gravity Field

We use GRAIL-determined degree and order 900 potential fields to construct the free-air gravity (GRGM900B) and Bouguer (GRGM900B_BOUGUER) anomaly maps (58). The Bouguer anomaly uses an average crustal density, ρ_B, of 2560 kg m^{-3} and includes the gravitational effect of finite amplitude topography (29; 59). We expand gravity and potential fields to degree and order 600 and invoke a high-pass filter to remove degrees 15. The gravity field is referenced to a radius of 1738 km.

5.2.3 Quasi-Circular Mass Anomaly Identification

We use several approaches to visually identify quasi-circular mass anomalies (QCMAs) with minimal or no topographic expression in the free-air gravity and Bouguer anomaly. Similar to (5), we visually identify QCMAs by systematically searching the lunar nearside in the free-air gravity and Bouguer anomaly maps with shifted and stretched color-scale ranges. Admittedly, this may bias the identification to the subset of QCMAs with the largest gravity anomaly contrast and areal extent. Hence, we employ gravity gradiometry to enhance short-wavelength features in the gravity field (see Figure 5-1). Using these methods, we identify 103 QCMAs (Figures 5-2 & 5-3).

Gravity Gradiometry

Similar to (142), we employ the horizontal components of the gravity tensor, commonly referred to as the gravity gradient (143). The horizontal components of the gravity tensor are the second derivatives of the Bouguer potential, U_B,

$$\begin{aligned}
\Gamma_{xx} &= \frac{1}{r^2 \sin^2\phi}\frac{\partial^2 U_B}{\partial \lambda^2} - \frac{\cot\phi}{r^2}\frac{\partial U_B}{\partial \phi} + \frac{1}{r}\frac{\partial U_B}{\partial r} \\
\Gamma_{yy} &= \frac{1}{r^2}\frac{\partial^2 U_B}{\partial \phi^2} + \frac{1}{r}\frac{\partial U_B}{\partial r} \\
\Gamma_{xy} &= \frac{1}{2r^2}\left(\frac{1}{\sin\phi}\frac{\partial}{\partial \lambda}\left(\frac{\partial U_B}{\partial \phi}\right) + \frac{\partial}{\partial \phi}\left(\frac{1}{\sin\phi}\frac{\partial U_B}{\partial \lambda}\right)\right) + \frac{\cot\phi}{r^2 \sin\phi}\frac{\partial U_B}{\partial \lambda}
\end{aligned} \tag{5.7}$$

where r is the lunar radius, λ is the longitude in radians, ϕ is the colatitude in radians, and x and y represent the longitudinal and latitudinal directions, respectively. As prescribed by (142), we combine the horizontal gradient eigenvalues into a single value, Γ_{hh}, of the second horizontal derivative of maximum amplitude at each Cartesian grid point on the surface:

$$\Gamma_{hh} = \begin{cases} \Gamma_{11} & \text{if } \Gamma_{11} > \text{abs}(\Gamma_{22}) \\ \Gamma_{22} & \text{if } \Gamma_{11} < \text{abs}(\Gamma_{22}) \end{cases} \tag{5.8}$$

In addition, we employ a modified antieigenvalue to identify buried craters. The anti-eigenvalue, μ_0, is defined as,

$$\mu_0 = \frac{2\sqrt{\lambda_1 \lambda_2}}{\lambda_1 + \lambda_2}, \tag{5.9}$$

and is valid for a positive-definite matrix (144). Accordingly, we modify the antieigenvalue to be applicable for negative-definite matrices, with the following modification,

$$\mu = Re(\mu_0) - \frac{Re(2\sqrt{\lambda_1 \lambda_2}) + Im(2\sqrt{\lambda_1 \lambda_2})}{|\lambda_1| + |\lambda_2|} \tag{5.10}$$

This is a novel approach to examine gravity fields and provides a tool to simultaneously examine long- and short-wavelength structures without amplitude bias. We apply Eqns. 5.8-5.10, for the identification of QCMAs in the free-air gravity and Bouguer anomaly fields.

Lunar Crater Relations

Assuming an initial, pre-impact site in isostasy with the surrounding area, we invoke the following crater relation (*Soderblom et al.*, in prep.), for Bouguer anomaly as a function of crater diameter (Figure 5-5),

$$\Delta g_u = -0.2288 D_c + 9.1189 \tag{5.11}$$

where Δg_u is the average gravity anomaly of the crater floor relative to the ejecta blanket area, extending from the crater edge to 2-crater radii (145) and D_c is the crater diameter. We assume that D_c is equivalent to the diameter of the QCMA.

Using a depth-diameter relation for fresh craters (*Sori & Zuber*, in prep.), we assume that the average floor depths, d, of our filled craters are:

$$d = 2.57 D_c^{0.14} \tag{5.12}$$

Similar to (*Soderblom et al.*, in prep.), we average the Bouguer anomaly along the floor of the putative buried craters (QCMAs) using (146) and (145),

$$D_f = \begin{cases} 0.19 D_c^{1.25} & \text{for } D_c < 80 \text{ km} \\ D_c - 1.84 * D_c^{2/3} & \text{for } D_c \geq 80 \text{ km} \end{cases} \tag{5.13}$$

where D_f is the floor diameter. To prevent uplifted central peak material from influencing our measurement in the central part of the crater, we use the floor diameter less the area encompassed by the central peak diameter, D_{cp}, (147; 148),

$$D_{cp} = \begin{cases} 0.22 D_c & \text{for } D_c < 140 \text{ km} \\ 0.4 D_c & \text{for } D_c \geq 140 \text{ km} \end{cases} \tag{5.14}$$

with a central peak height, h_{cp},

$$h_{cp} = \min(3, 0.0006 D_c^{1.97}). \tag{5.15}$$

For completely buried craters, we remove the influence of rim height from the depth of the crater, as it will have a minimal influence on the gravity anomaly relative to the ejecta

blanket (see Figure 5-4).

$$h_r = 0.236 D_c^{0.399} \tag{5.16}$$

5.2.4 Loading Model

In order to calculate the effects of material filling on the lunar nearside, we derive the gravitational attraction of the mare load, Δg_m, at the surface, s, from the general form of Newton's law of universal gravitation,

$$\Delta g_s = \Delta g_u + \sum_{e=1}^{N} \frac{G \Delta \rho A_e h_e}{a_e^2} \tag{5.17}$$

where,

$$\Delta \rho = \begin{cases} \rho_B - \rho_c & \text{for } d_e < h - h_f \\ \rho_f - \rho_c & \text{for } d_e \geq h - h_f \end{cases} \tag{5.18}$$

and where ρ_c is the density of the crust, ρ_f is the density of the infill, h is the height of the pre-impact surface above the floor, and h_f is the height of the fill. Each element has an area, A_e, height, h_e, depth below the pre-impact surface, d_e, and corresponding distance, a_e, between the element and measurement point on the reference surface, s. We choose to discretize the load into a $101 \times 101 \times 101$ element grid and use a local geoid surface grid of 101×101 elements.

5.2.5 Effective Density Estimation

Based on (40), we can calculate the effective density, ρ_e, at the surface assuming a flat surface (neglecting curvature) and crust-mantle boundary (41; 45),

$$\rho_e = \frac{1 - e^{-k h_0}}{h_0} \left(\frac{\rho_0}{k} - \frac{\Delta \rho_0}{k + d^{-1}} \right) \tag{5.19}$$

where k is the wavenumber, $2h_0$ is the amplitude of topography, d is the depth of the interface, ρ_0 is the surface density, and $\Delta\rho_0$ is the density contrast across the interface. The above equation is formulated for a Cartesian grid without the finite-amplitude topography correction.

For a set of density contrasts, we may compare the result from Eq. 5.19 to the topography-induced gravity anomaly (LOLA1080_PA_MWRP) from LOLA. We compute the admittance spectrum over a localized region and compare with results from Eq. 5.19. The transfer function relating the topography-induced gravity anomaly with unit density to the Bouguer anomaly is the admittance spectrum, Z, defined as

$$Z(l) = \frac{S_{gt}(l)}{S_{tt}(l)}, \tag{5.20}$$

where S_{gt} is the cross-power spectrum of the Bouguer anomaly and topography-induced gravity anomaly and S_{tt} is the power spectrum of the topography-induced gravity anomaly (59).

5.3 Results & Discussion

5.3.1 Partially Buried Craters

We identify a population of 80 anomalously shallow craters on the lunar nearside that may be partially buried by lunar maria. We limit our crater population to those within the lunar maria region (see Figure 5-6) and with diameters of 20-200 km. Using Equation 5.11, we can remove the portion of the gravity associated with crater formation and modification (e.g. floor fracturing, mantle uplift) and use the remaining gravity anomaly to constrain the density of the infill and excavated material (see Eq. 5.17, Fig. 5-7).

For our population of partially buried craters, we find a median density contrast of 100 kg-m^{-3} (Fig. 5-7c) with a majority of the craters filled with material denser than the excavated (original) surface. As shown in Fig 5-7, the excavated and fill density of the partially buried

craters have a bi-modal distribution with peaks at approximately 2400 and 3200 kg-m^{-3} consistent with existence of two dominant mineralogies with different densities.

5.3.2 Buried Craters

We identify a population of 103 quasi-circular mass anomalies (QCMAs) on the lunar nearside that may be craters filled by lunar maria (Fig 5-2). As shown in Figure 5-8a, below 80-km diameter, a majority of the QCMAs are within one standard deviation of the Bouguer anomaly mean for lunar craters. Beyond 80 km, the QCMAs concentrate into two groups, one above and one below the average lunar crater trend.

We find the group of QCMAs above the lunar crater trend are most consistent with filled material with an average density contrast of 800 kg/m^3, while the group below the trend are best fit to a density contrast of -200 kg/m^{-3}. This bi-modal distribution is consistent with the histogram of density contrasts in Figure 5-8b.

5.3.3 Surface Depth & Volume Estimates

Using the existing lunar crater inventory for craters greater than 20 km (149) with the QCMAs found in this study, we estimate variable depths and total volume of the lunar nearside maria.

Crater-based Estimates

We focus on three main estimates using buried craters:

1. Scenario A – a depth calculation using depth differences between fresh craters and regional lunar craters (including QCMAs).
2. Scenario B – a depth calculation using depth differences between fresh craters and all buried craters.

3. Scenario C – a depth calculation using buried crater rim heights in addition to depth differences between fresh craters and partially buried craters.

Scenario A presumes that any departure in crater depth from the pre-impact surface is due to mare infill. We use the fresh crater depth-to-diameter relation (Eq. 5.12) less the rim height (Eq. 5.16) to determine the expected depth, d_e. As the putative buried craters, QCMAs, have minimal or no surface expression, we consider the craters and related rims to be buried. Thus for the QCMAs, we use only the fresh crater depth-to-diameter relation (Eq. 5.12) to approximate the mare fill height. Under this scenario, we find 3×10^7 km^3 of mare material, equivalent to a 3-km average layer, may be deposited on the lunar nearside with lenses of material greater than 5-km depth (Fig. 5-9a).

With Scenario B, we also find a mare volume estimate of 3×10^7 km^3, although this scenario has a greater uniformity in depth across the lunar nearside (Fig. 5-9b). Scenario B presumes the complete filling of craters is representative of the lunar nearside. In Scenario C, we consider the complete filling of craters as non-representative of the region and assume the major contribution of mare infill is partial crater infill and crater rim burial. For Scenario C, we find a mare volume estimate of 2×10^7 km^3, equivalent to a 2-km layer of mare across the lunar nearside region.

Localized Regional Analysis

Using localized admittance, we attempt to place constraints on the depth of mare fill for the lunar nearside. With Equation 5.19, we consider the difference in the admittance profile expected for a positive (increasing density with depth) and negative density (decreasing density with depth). contrast at depth. From Figure 5-10, we expect a positive density contrast to result in a monotonically decreasing curve and a negative density contrast to result in a monotonically increasing curve.

We examine four lunar regions with localized admittance analysis, two with and two without mare fill. In the regions without mare fill (see Figure 5-11), we observe a trend consistent with a positive density contrast and a best-fit depth of 0 km. Contrarily, the regions

with mare fill have the opposite trend (see Figure 5-12) at higher harmonic degrees (>250), with an increasing trend with harmonic degree. This is consistent with a denser layer being present at the surface. Using Equation 5.19, we attempt to find a best-fit depth, but our results are inconclusive, though would be consistent with depths of 0-8 km.

5.4 Discussion

5.4.1 Density

Our population of partially and putative buried craters provide constraints on the density of mare material on the lunar nearside. Unlike completely buried craters, the partially buried craters allow us to individually solve for the crater infill and excavated density (see Eq. 5.18). The multimodal distribution of partially buried crater excavated and fill densities with peaks at the same densities suggest that two distinct mineralogies may be present. The two peaks at approximately 2350 kg/m^{3}and 3150 kg/m^3 are consistent with fractured anorthositic highlands crust and lunar maria densities (59; 127; 150).

The density contrast for the partially buried craters, centered at 100 kg/m^3 suggests, on average, these craters tend to be filled with material of slightly denser material. This may be due to a combination of crater fill by impact ejecta and mass wasting of the crater walls. Further, this result suggests that mare fill of the anorthositic crust is rare and is unlikely to provide a representative example of maria thickness on the lunar nearside. However, we note our partially buried craters are biased toward craters along the periphery of the nearside lunar maria region and crater rims and we may be preferentially selecting regions where we are most likely to find anorthositic crustal impacts.

For our putative buried impact craters, we find that below 80-km diameter, craters have the same Bouguer anomaly-to-diameter relationship as unfilled craters. This may indicate that the majority of buried craters with less than 80-km diameter have impacted into mare, without penetrating to an underlying crust, and are subsequently filled by mare of approximately the same density. Beyond 80-km diameter, the Bouguer anomaly of the putative

craters diverge into a group with a high Bouguer anomaly, requiring an average density contrast of 800 kg/m^3, and a group with a low Bouguer anomaly, requiring a density contrast less than -200 kg/m^3. The low Bouguer anomaly group may be explained by an impact into anorthositic crust overlain by mare that was subsequently re-filled by mare with the expected post-impact inflow to be of anorthositic crust and contributing to a lower Bouguer anomaly. Additionally, the higher density of impact ejecta from a mare impact would contribute to a low Bouguer anomaly. The high Bouguer anomaly group, is consistent with a fill-to-excavated density contrast of approximately 800 kg/m^3. This is the average density contrast that we expect for an impact into anorthositic crust that was subsequently filled by mare. Accordingly, the high Bouguer anomaly group may represent the pre-mare surface of the lunar nearside. Given the error in the Bouguer anomaly-to-diameter relation, we estimate the density contrast is 800$\pm$200 kg/m^3 with a lunar mare density of 3300$\pm$200 kg/m^3.

While our estimate of the lunar mare density is consistent with recent measurements (150) of Apollo-era samples and lunar meteorites, our result may indicate slightly higher (100 kg/m^3) bulk densities for the lunar maria or that the nearside lunar crust is less dense than the average crust. This suggests that the lunar maria in buried craters may have a lower porosity than the lunar samples, which could be explained by an extensive, less Ti-rich lunar mare phase succeeding an earlier, Ti-rich phase as suggested by (123). This would require a majority of our buried crater population to be filled by the early, Ti-rich lunar mare phase.

5.4.2 Mare Depth & Volume

The divergence from the putative buried craters from the nominal Bouguer anomaly-to-diameter trend occurs for between 50-80 km in diameter and likely corresponds to penetration through lunar maria. Using (110), $D = 1.32 D_{at}^{1.086} D_{sc}^{-0.086}$ where D_{sc} represents the single-to-complex transition diameter, approximately 20 km, and the excavation depth as approximately 10% of the excavation diameter (145), the 50 to 80-km transition corre-

sponds to an excavation depth of 2.2-3.5 km. This depth may correspond to the average depth of mare on the lunar nearside. In our localized admittance analysis, of two regions on the lunar mare nearside, we find that an average depth between 2-3 km is possible, and has a slightly higher probability in our best-fit estimation.

The three different scenarios we evaluate for volume yield the same order of magnitude 2-3$\times 10^7$ km^3 of mare. Prior investigations (119; 133; 130; 131; 132), suggest that the mare loading varies extensively across the lunar nearside, would be more consistent with fill scenarios A and C. Given that each of the scenarios is consistent with the average depth that we expect from our QCMAs, each of these scenarios may be equally viable representations of the lunar nearside mare fill.

5.4.3 Other Factors

The Bouguer anomaly-to-diameter relation of *Soderblom et al.*, in prep. is based on the fracturing and mantle uplift expected to occur for lunar impacts. Given the majority of the lunar surface is represented by the anorthositic highlands crust, this estimate may not adequately reflect impacts into lunar mare regions; however, we expect any changes would preferentially affect smaller impacts which are least likely to impact a mare region without penetrating underlying crustal material. Through the impact process, the underlying crust of a crater is fractured and mare may intrude the porous space, creating an increase in density as well a localized mare upwelling underneath the crater and may result in an overestimate of the density infill for a buried basin. This may partly explain the putative buried craters with derived density contrasts greater than 1000 kg/m^3 and may yield a slightly overall higher density contrast between the mare infill and anorthositic highlands crust. Further, increased heat for lunar mare flow may allow for preferential annealing of pore space due to the increased heat flow also resulting in higher derived densities for mare infill. We also note that if the crater diameter is underestimated for the high Bouguer anomaly group and the crater diameters are approximately 300 km, a mass concentration (mascon) would be expected interior to the basin that may account for the high Bouguer

anomaly (Neumann, *et al.*, *in rev.*)

5.5 Summary

Using gravity data from the GRAIL mission, we find 103 quasi-circular mass anomalies beneath the lunar nearside maria. Below 80 km, the mass anomalies follow the same Bouguer anomaly-to-diameter trend as lunar craters, while they diverge at larger diameters, which we have interpreted as impact craters exceeding the average depth of the lunar maria. With separate analyses, using localized admittance and crater-based estimates, we constrain the average thickness of the lunar maria to 2-3.5 km, or 2-3.5$\times 10^7$ km^3 in total. The existence of such a large quantity of buried craters suggests that there is a heterogeneous distribution of lunar maria across the nearside, with craters and rim burial more than 5 km of lunar mare. In concert with 80 anomalously shallow lunar nearside craters, we find the lunar maria may have a density contrast of 800 kg/m^3 with the anorthositic highlands crust, resulting in a lunar mare density of 3300$\pm$200 kg/m^3.

5.6 Acknowledgements

This work was conducted as part of the GRAIL mission and is supported by NASAs Discovery Program and is performed under contract to the Massachusetts Institute of Technology and the Jet Propulsion Laboratory, California Institute of Technology. I thank J. Soderblom, P. B. James, Y. Tewelde, and J. Andrews-Hanna for assistance and helpful comments.

5.7 Figures

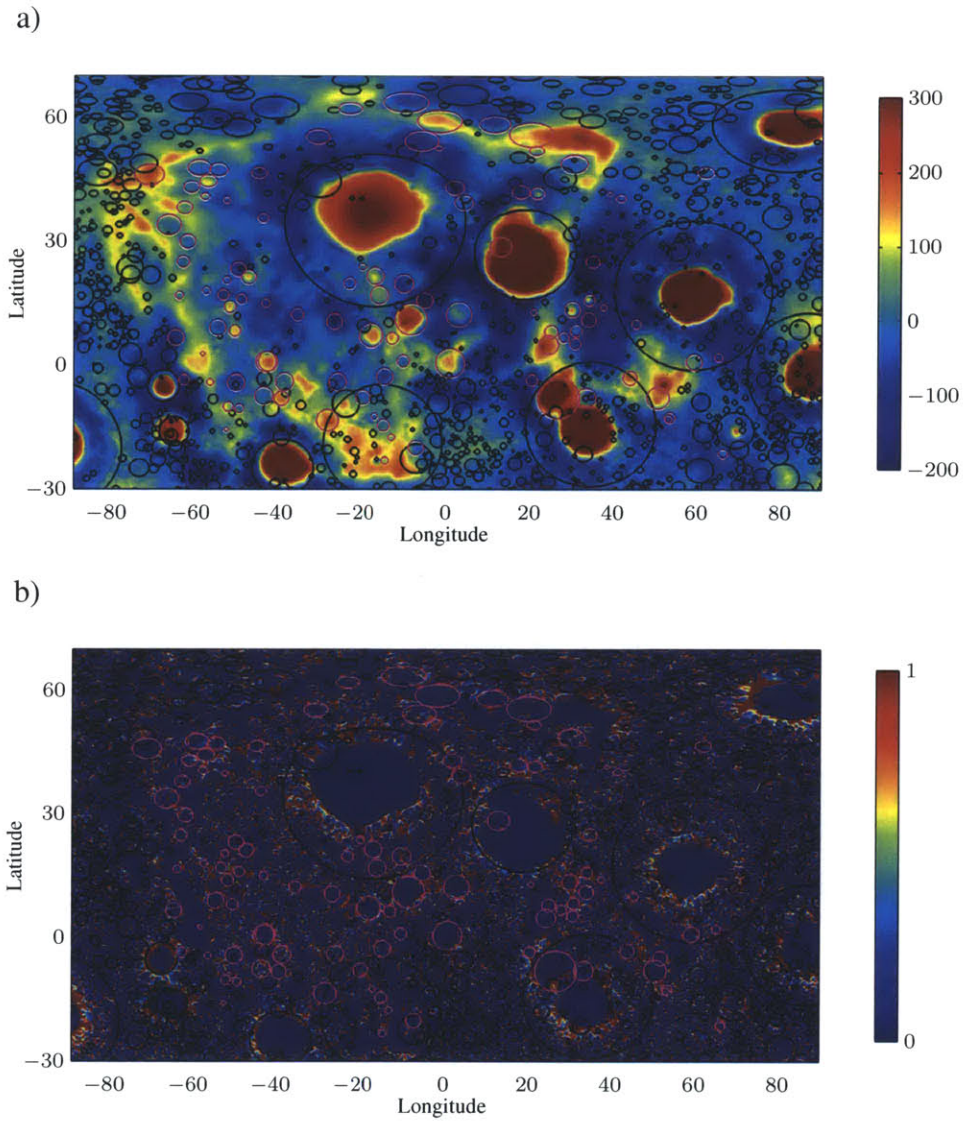

Figure 5-1: Lunar Nearside Gravity. Superimposed craters (black) and quasi-circular mass anomalies (magenta) are shown on the lunar nearside a) Bouguer anomaly and b) modified antieigenvalue maps.

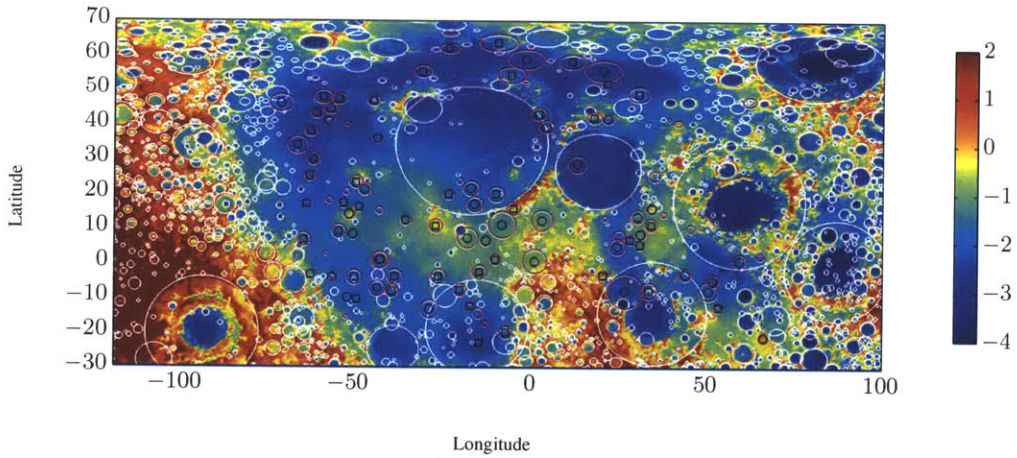

Figure 5-2: Lunar Nearside Topography (km) with Superimposed QCMAs. The image encompasses the maria-flooded, nearside region of our investigation. QCMAs (magenta) and regional lunar craters (white) are shown with circles corresponding to the diameter. QCMAs more than 25 mgal above (circle) and below (square) the average crater Bouguer anomaly v. diameter (see Eq. 5.11) are identified with black symbols.

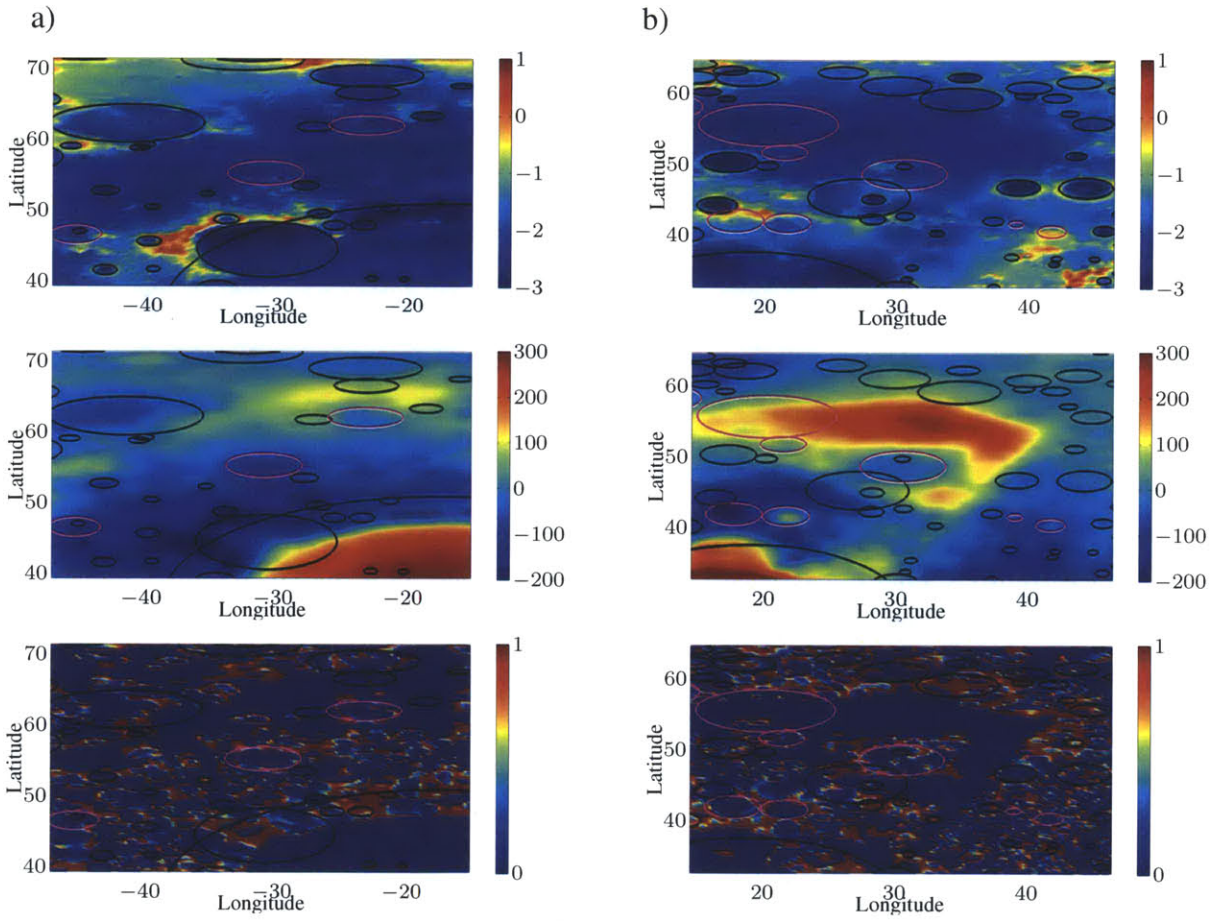

Figure 5-3: Lunar Nearside Gravity. From top to bottom, panels of topography (km), Bouguer anomaly (mgal), and modified antieigenvalue. Superimposed craters (black) and quasi-circular mass anomalies (magenta) are shown antieigenvalue maps. a) Panels northwest of Imbrium basin. b) Panels northeast of Imbrium basin.

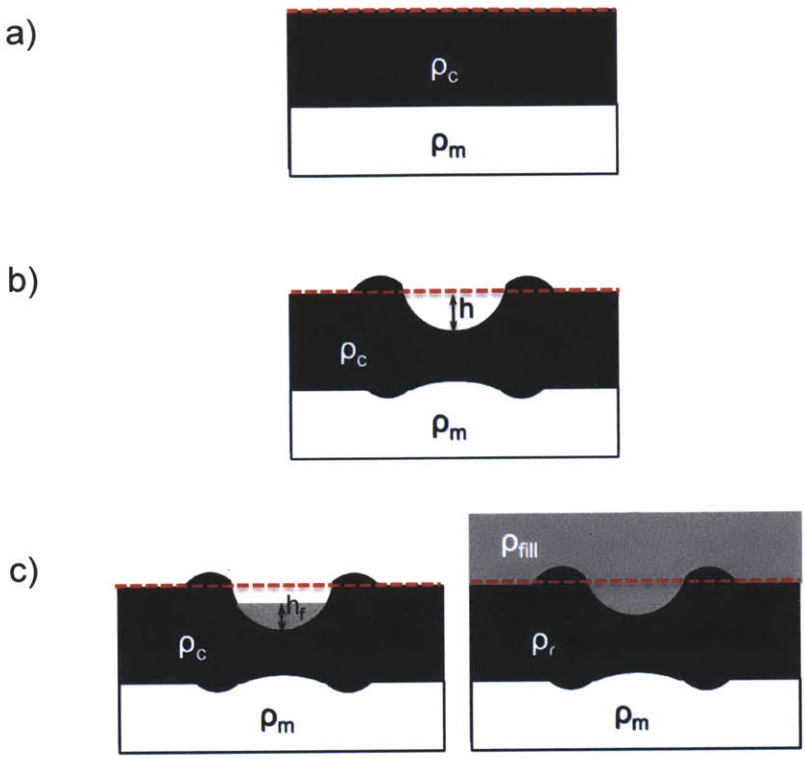

Figure 5-4: Conceptual Model (not to scale) a) Pre-Impact - The initial, pre-impact surface (red-dashed line) is assumed to be in isostasy with the surrounding area with the crustal layer (black) with density, ρ_c above the upper mantle layer (white) with density ρ_m. b) Post-impact modification, the crust is deformed leaving an unfilled crustal cavity with impact-related fracturing and possible mantle uplift below the cavity. c) The impact crater is subsequently filled partially or fully with the gray material which we presume is lunar maria of density ρ_{fill}.

a)

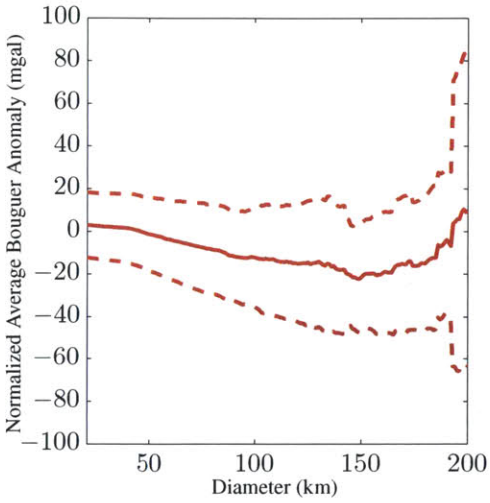

b)

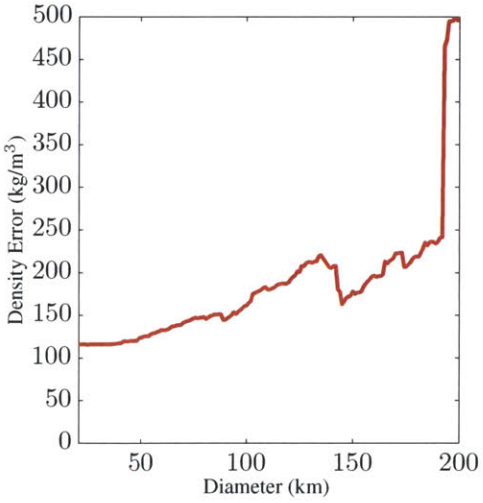

Figure 5-5: Rolling Average by Crater Diameter (km). a) The 20-km rolling average (solid line) and $\pm 1\sigma$ (dashed lines) for crater Bouguer anomaly (mgal), excluding the South-Pole Aitken basin. b) Rolling average of density error based on 1-σ error of crater Bouguer anomaly.

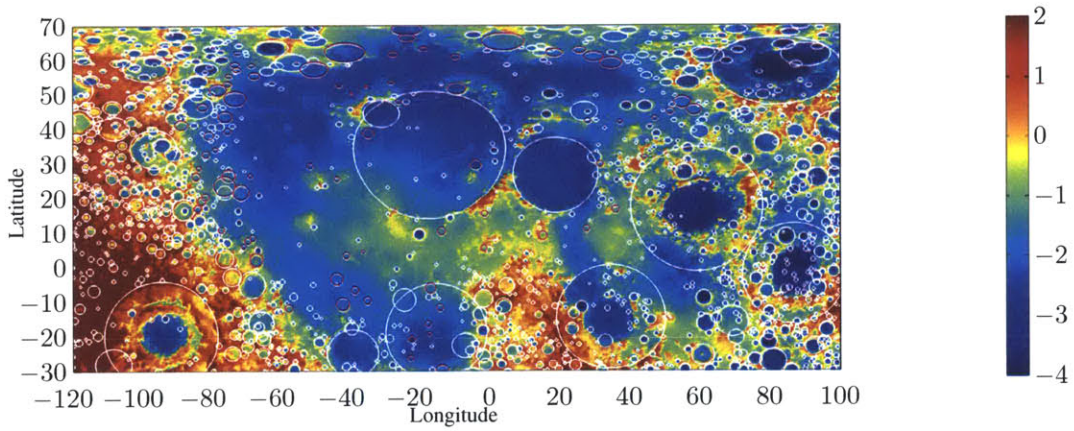

Figure 5-6: Lunar Nearside Topography (km) with Superimposed QCMAs. The image encompasses the maria-flooded, nearside region of our investigation. QCMAs (magenta) and regional lunar craters (white) are shown with circles corresponding to the diameter. QCMAs more than 25 mgal above (circle) and below (square) the average crater Bouguer anomaly v. diameter (see Eq. 5.11) are identified with black symbols.

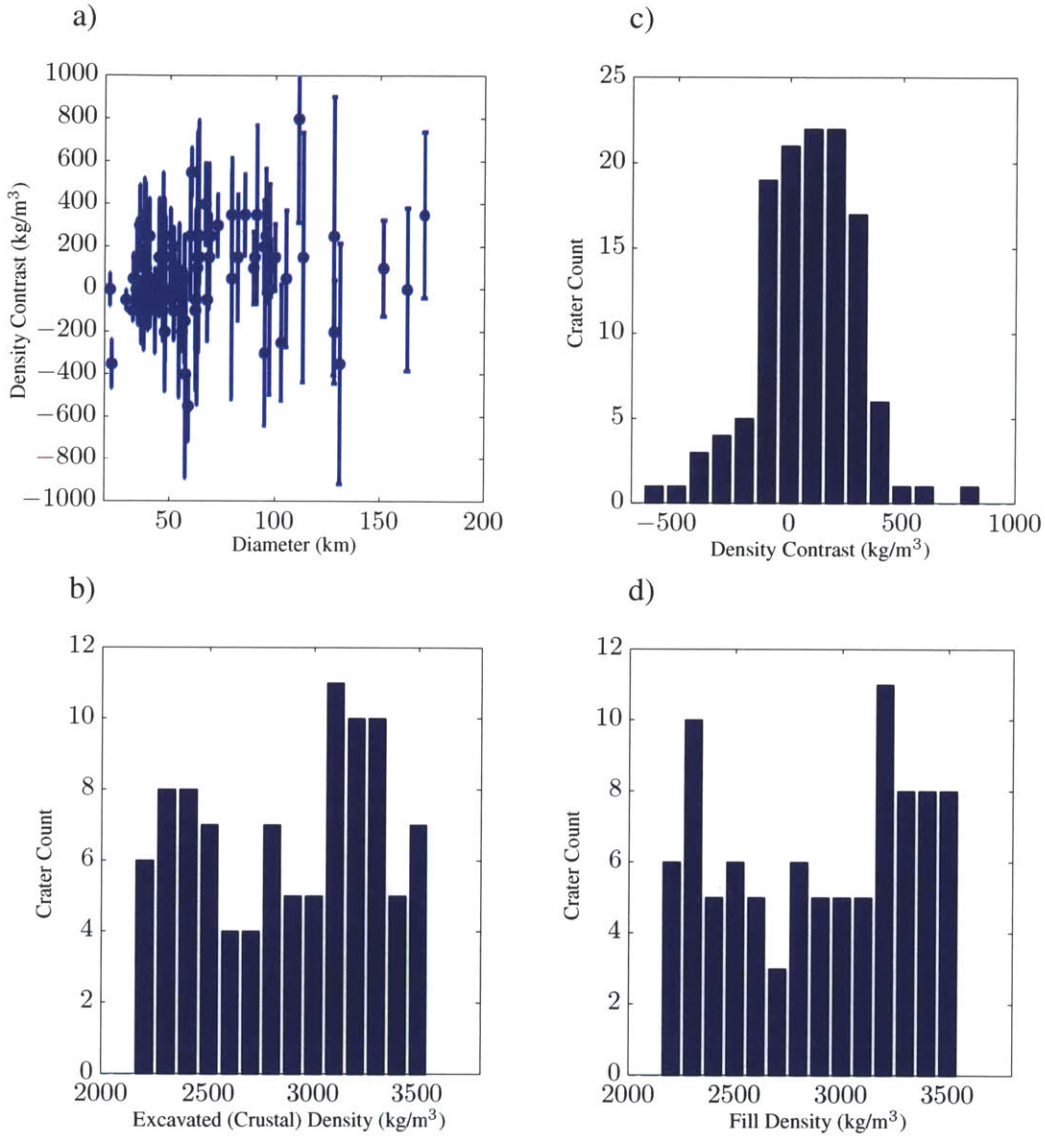

Figure 5-7: Partially-Buried Craters Densities using GRAIL Data. a). The density contrast between the infill density and the excavated (pre-impact surface) density for the excess material in partially buried crater. b) Crater count for partially-buried craters with the calculated excavated density. c) Crater count for partially-buried craters with the calculated density contrast between the infill density and the excavated density. d) Crater count for partially-buried craters across infill density.

a)

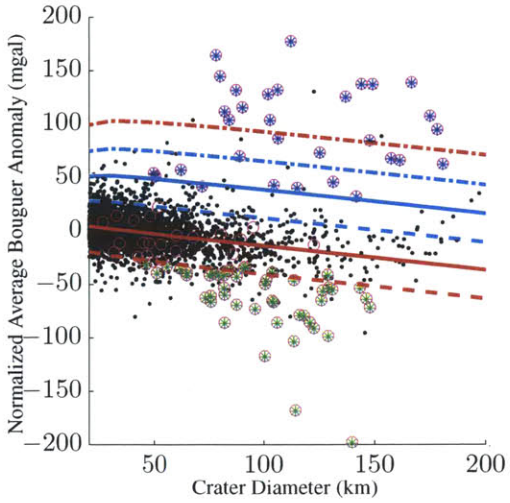

b)

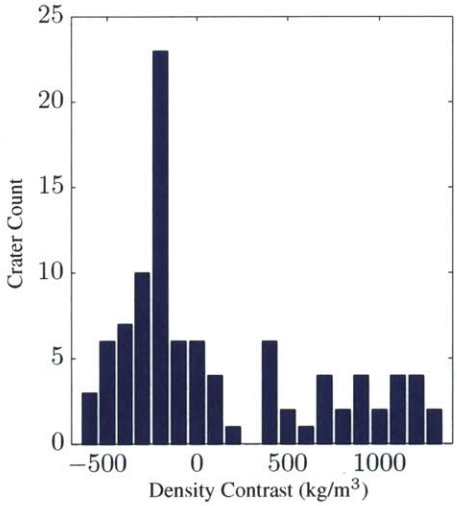

Figure 5-8: QCMA Trends using GRAIL Data. a) Normalized Average Bouguer Anomaly (mgal) v. Diameter (km). Assuming the QCMAs are buried craters, gravity anomaly is reference to the gravity anomaly within the ejecta blanket area. QCMAs (magenta circles) and lunar crater catalog (black dots) are shown with circles corresponding to diameter. QCMAs more than 25 mgal above (blue asterisks) and below (green asterisks) the normalized average crater Bouguer anomaly v. diameter. The lines are from Equation 5.17 with density contrasts of -200 (red-dashed), 0 (red solid), 200 (cyan dashed), 400 (cyan solid), 600 (cyan dashed-dot), and 800 (red dashed-dot) kg/m^3. b) Crater Count v Density Contrast (kg/m^3). The density contrast between the infill density and the excavated (pre-impact surface) density for the excess material in partially buried crater.

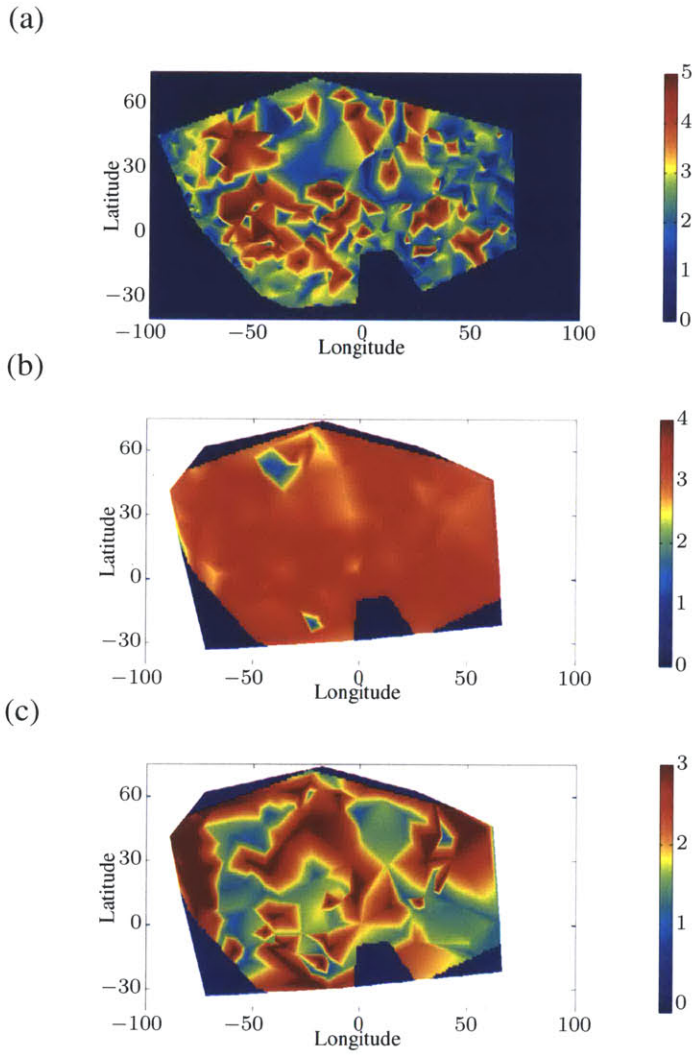

Figure 5-9: Nearside Mare Fill Depth Estimates (km). (a) Maximum Depth. This scenario is calculated based on interpolated differences of regional craters depths to reference fresh crater depths. (b) Completely and Partially Buried Crater Depth. This scenario is calculated based on interpolated differences of completely and partially buried craters depths to reference fresh crater depths. (c) Completely Buried Crater Rim Height and Partially Buried Crater Depths. This scenario is calculated based on completely buried crater rim heights and partially buried craters depths to reference fresh crater depths.

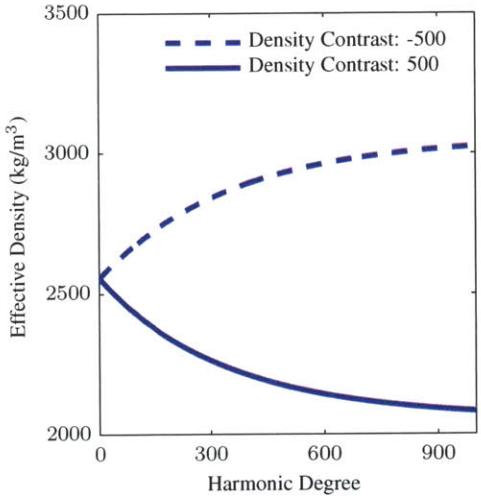

Figure 5-10: Effective Density Model. Using Equation 5.19, we calculate the theoretical profile for density contrast of 500 and -500 kg/m^3 at a depth of 6 km. A positive density contrast (denser material below surface) yields a representative monotonically decreasing curve and a negative density contrast (denser material layer at surface) yields a representative monotonically increasing curve.

a) Admittance in Non-Mare Region - 0^o, 60^oN c) Best-Fit Depths in Non-Mare Region - 0^o, 60^oN

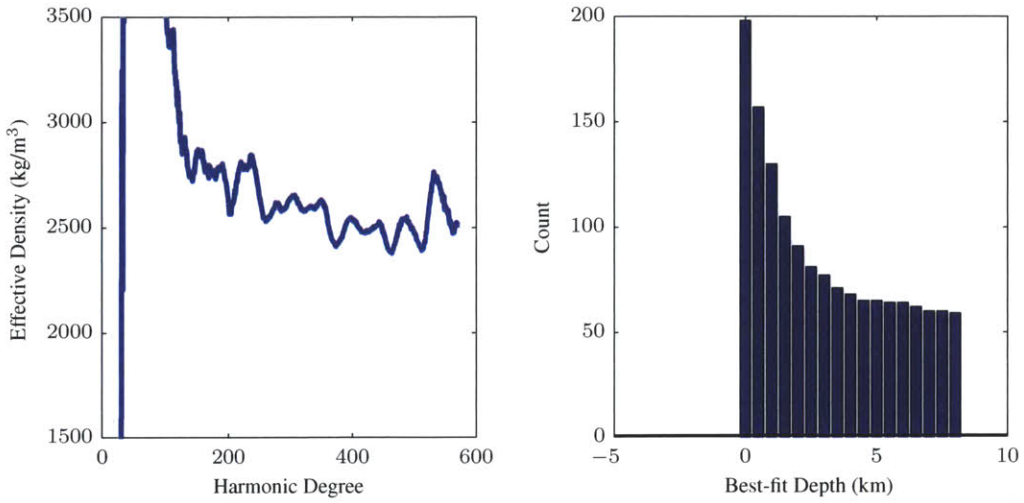

a) Admittance in Non-Mare Region - 8^oE, 62^oN c) Best-Fit Depths in Non-Mare Region - 8^oE, 2^oN

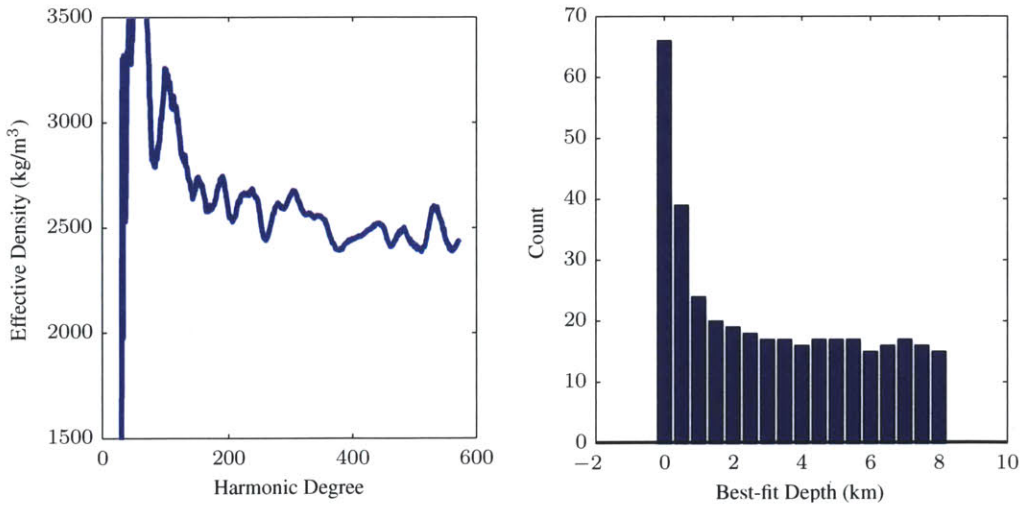

Figure 5-11: Localized Admittance (9^o spherical cap) for Non-Mare Region. Localized admittance curves for spherical cap centered at (a) 0^o, 60^oN and (b) 8^oE, 62^oN. The decreasing effective density trend between harmonic degrees 250-600 indicate a layer of decreasing density at the surface. With a range of density contrasts (1400 - 200 kg/m^3) and subsurface densities (1500 - 2800 kg/m^3), we use Equation 5.19 to calculate the count of best-fit depths (within 30% of minimum misfit) for regions (c) 0^o, 60^oN and (d) 8^oE, 62^oN.

a) Admittance in Mare Region - 40^{o}E, 46^{o}N

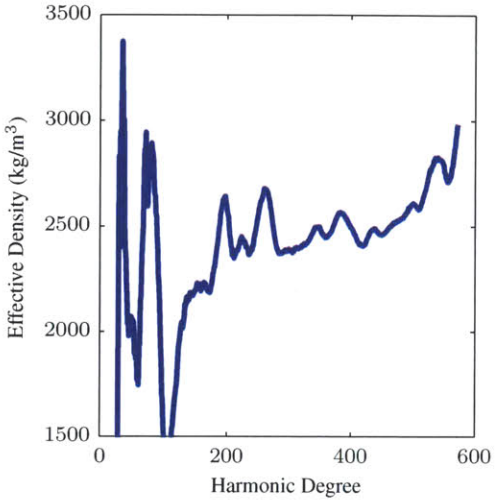

c) Best-Fit Depths in Mare Region - 40^{o}E, 46^{o}N

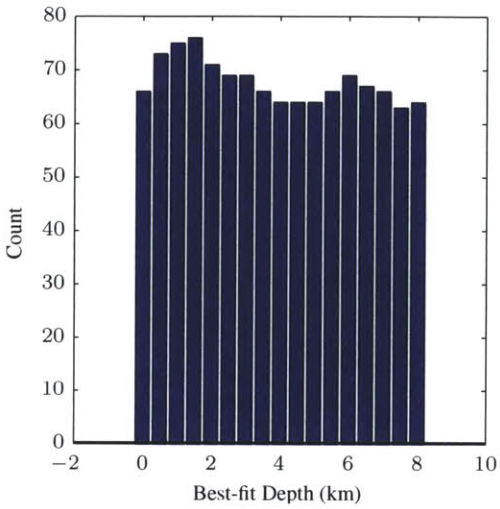

b) Admittance in Mare Region - 0^o, 50^{o}N

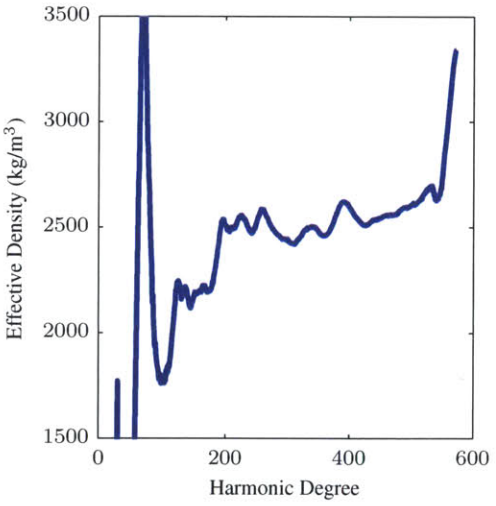

d) Best-Fit Depths in Mare Region - 0^o, 50^{o}N

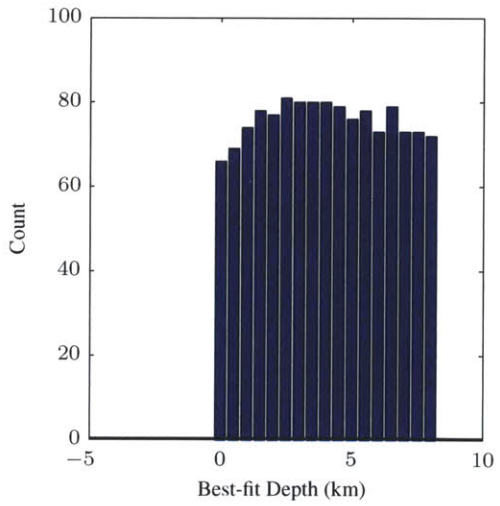

Figure 5-12: Localized Admittance (9^o spherical cap) for Mare Region. Localized admittance curves for spherical cap centered at (a) 40^{o}E, 46^{o}N and (b) 0^o, 50^{o}N. Increasing effective density trend between harmonic degrees 250-600 indicate a layer of increased density at the surface. With a range of density contrasts (1400 - 200 kg/m^3) and subsurface densities (1500 - 2800 kg/m^3), we use Equation 5.19 to calculate the count of best-fit depths (within 30% of minimum misfit) for regions (c) 40^{o}E, 46^{o}N and (d) 0^o, 50^{o}N.

Chapter 6

Future Work

6.1 A Wet Lunar Mantle: Basin Modification

The uncertainty in the initial basin depth profile we use for our lunar basin relaxation model is possibly a large contribution to the error. The hydrodynamic simulation work of Miljkovic et al., (*in revision*) may be used to constrain the uncertainty in our initial profile for a variety of thermal conditions. This would also allow the investigation of long-term viscoelastic basin relaxation modeling for nearside and lunar highland impacts. In addition to impacts within the lunar highlands, inventories of young complex craters and basins can help place constraints on viscosities and temperatures in our relaxation model as these impact structures should exhibit less relaxation compared with the remainder of the lunar basin inventory.

Using lunar elevation data, an average basin profile may be constructed and compared to my model results to find the best-fit model. A best-fit analysis may then be used to constrain the water concentration for the upper lunar mantle. This analysis may be applied the lunar impact basin inventory to identify possible lateral and temporal subsurface heterogeneities. Future work should also examine the effect of stress-dependent viscosity on basin relaxation.

6.2 Recovery of Buried Lunar Craters

The inventory for partially buried craters is anomalously shallow craters on the lunar nearside, mostly near the periphery of the lunar maria; this selection bias may skew our results. Given the lack of statistically significant peaks in excavated and fill density plots, work should be done to tailor the partially buried crater dataset to partially buried craters with infill identified by spectral or imagery analysis. An analytical approach should be used to determine the minimum infill density and depth required to uniquely attain accurate and precise densities from best-fit analyses. This analysis may then be applied to use the best crater candidates for the partially buried inventory.

Additionally, future work on this project should entail examination of the crater-size frequency distribution with the buried crater population to place limits on the age of the nearside mare region and underlying surface. This may provide further constraints on lunar maria timing as well as a maximum age for the underlying surface.

The current analysis of buried craters does not consider overburied basins, which may be a contributing factor to the lack of a characteristic density contrast peak consistent with lunar maria density. A general error analysis may be conducted to constrain the density estimate for a range of overburial values, although a best-fit analysis for a range of density contrasts of buried basins may provide a more precise estimate.

The final partially and completely buried crater databases should be compared with concentrations of FeO, Th, and TiO_2 to ascertain any correlations in crater density with surface deposits or increased heating. In general, statistical significance tests for my density and mare thickness estimates should be applied to the results.

Bibliography

[1] L. Elkins-Tanton, S. Burgess, and Q.-Z. Yin, "The lunar magma ocean: Reconciling the solidification process with lunar petrology and geochronology," *Earth And Planetary Science Letters*, vol. 304, pp. 326–336, Apr. 2011.

[2] D. H. Scott, K. L. Tanaka, and P. Geology, "Geologic map of the western equatorial region of Mars, Scale 1:15,000,000, ," *U.S. Geol. Survey Map I-1802-A.*, 1986.

[3] R. Greeley and J. Guest, "Geologic map of the eastern equatorial region of Mars," *Scale 1:15,000,000, U.S. Geol. Survey Map I-1802-B*, 1987.

[4] G. E. McGill and S. W. Squyres, "Origin of the Martian crustal dichotomy: Evaluating hypotheses," *Icarus*, vol. 93, pp. 386–393, Oct. 1991.

[5] H. Frey, S. E. Sakimoto, and J. Roark, "The MOLA Topographic signature at the crustal dichotomy boundary zone on Mars," *Geophysical Research Letters*, vol. 25, no. 24, pp. 4409–4412, 1998.

[6] D. E. Smith, "The Global Topography of Mars and Implications for Surface Evolution," *Science*, vol. 284, pp. 1495–1503, May 1999.

[7] D. E. Smith, M. T. Zuber, H. V. Frey, J. B. Garvin, J. W. Head, D. O. Muhleman, G. H. Pettengill, R. J. Phillips, S. C. Solomon, H. J. Zwally, W. B. Banerdt, T. C. Duxbury, M. P. Golombek, F. G. Lemoine, G. A. Neumann, D. D. Rowlands, O. Aharonson, P. G. Ford, A. B. Ivanov, C. L. Johnson, P. J. McGovern, J. B. Abshire, R. S. Afzal, and X. Sun, "Mars Orbiter Laser Altimeter: Experiment summary after the first year of global mapping of Mars," *Journal of Geophysical Research*, vol. 106, pp. 23689–23722, Oct. 2001.

[8] M. Zuber, S. Solomon, R. Phillips, D. Smith, G. Tyler, O. Aharonson, G. Balmino, W. Banerdt, J. Head, and C. Johnson, "Internal structure and early thermal evolution of Mars from Mars Global Surveyor topography and gravity," *Science*, vol. 287, no. 5459, p. 1788, 2000.

[9] G. A. Neumann, M. T. Zuber, M. A. Wieczorek, P. J. McGovern, F. G. Lemoine, and D. E. Smith, "Crustal structure of Mars from gravity and topography," *Journal of Geophysical Research-Planets*, vol. 109, no. E8, p. E08002, 2004.

[10] W. Kiefer, "Buried mass anomalies along the hemispheric dichotomy in eastern

Mars: Implications for the origin and evolution of the dichotomy," *Geophysical Research Letters*, vol. 32, no. 22, p. L22201, 2005.

[11] B. Hynek and R. Phillips, "Evidence for extensive denudation of the Martian highlands," *Geology*, vol. 29, no. 5, pp. 407–410, 2001.

[12] M. C. Malin, "Sedimentary Rocks of Early Mars," *Science*, vol. 290, pp. 1927–1937, Dec. 2000.

[13] R. A. Craddock, T. A. Maxwell, and A. D. Howard, "Crater morphometry and modification in the Sinus Sabaeus and Margaritifer Sinus regions of Mars," *Journal of Geophysical Research-Planets*, vol. 102, no. E6, pp. 13321–13340, 1997.

[14] R. A. Craddock and T. A. Maxwell, "Geomorphic evolution of the Martian highlands through ancient fluvial processes," *Journal of Geophysical Research-Planets*, vol. 98, no. E2, pp. 3453–3468, 1993.

[15] M. P. Golombek, J. A. Grant, L. S. Crumpler, R. Greeley, R. E. Arvidson, J. F. Bell, III, C. M. Weitz, R. Sullivan, P. R. Christensen, L. A. Soderblom, and S. W. Squyres, "Erosion rates at the Mars Exploration Rover landing sites and long-term climate change on Mars," *Journal of Geophysical Research*, vol. 111, pp. E12S10–, Dec. 2006.

[16] C. I. Fassett and J. W. Head, III, "Layered mantling deposits in northeast Arabia Terra, Mars: Noachian-Hesperian sedimentation, erosion, and terrain inversion," *Journal of Geophysical Research*, vol. 112, p. E08002, Aug. 2007.

[17] J. M. Moore, "Nature of the mantling deposit in the heavily cratered terrain of northeastern Arabia, Mars," *Journal of Geophysical Research*, vol. 95, no. B9, p. 14279, 1990.

[18] M. T. Zuber, D. E. Smith, S. C. Solomon, D. O. Muhleman, J. W. Head, J. B. Garvin, J. B. Abshire, and J. L. Bufton, "The Mars Observer laser altimeter investigation," *Journal of Geophysical Research-Planets*, vol. 97, no. E5, pp. 7781–7797, 1992.

[19] A. Albee, R. Arvidson, F. Palluconi, and T. Thorpe, "Overview of the Mars Global Surveyor mission," *Journal of Geophysical Research*, 2001.

[20] R. W. Zurek and S. E. Smrekar, "An overview of the Mars Reconnaissance Orbiter (MRO) science mission," *Journal of Geophysical Research*, vol. 112, p. E05S01, May 2007.

[21] D. L. Turcotte, R. J. Willemann, W. F. Haxby, and J. Norberry, "Role of membrane stresses in the support of planetary topography," *Journal of Geophysical Research-Planets*, vol. 86, no. B5, pp. 3951–3959, 1981.

[22] F. J. Simons, F. A. Dahlen, and M. A. Wieczorek, "Spatiospectral Concentration on a Sphere," *SIAM Review*, vol. 48, pp. 504–536, Jan. 2006.

[23] M. Wieczorek and F. Simons, "Localized spectral analysis on the sphere," *Geophysical Journal International*, vol. 162, no. 3, pp. 655–675, 2005.

[24] P. McGovern, S. Solomon, D. Smith, M. Zuber, M. Simons, M. Wieczorek, R. Phillips, G. Neumann, O. Aharonson, and J. Head, "Localized gravity/topography admittance and correlation spectra on Mars: Implications for regional and global evolution," *Journal of Geophysical Research*, vol. 107, no. 10.1029, 2002.

[25] M. Wieczorek, "The gravity and topography of the terrestrial planets," *Treatise on Geophysics*, vol. 10, pp. 165–206, 2007.

[26] F. J. Simons, "MATLAB Open Source Software," 2006.

[27] C. L. Johnson, J. W. Head, R. J. Phillips, D. E. Smith, and M. T. Zuber, "Lithospheric Loading by the Northern Polar Cap on Mars," *Icarus*, vol. 144, pp. 313–328, Apr. 2000.

[28] P. McGovern, S. Solomon, and D. Smith, "Correction to "Localized gravity/topography admittance and correlation spectra on Mars: Implications for regional and global evolution"," *Journal of Geophysical Research*, vol. 109, pp. 1–5, 2004.

[29] M. A. Wieczorek and R. J. Phillips, "Potential anomalies on a sphere: Applications to the thickness of the lunar crust," *Journal of Geophysical Research-Planets*, vol. 103, no. E1, pp. 1715–1724, 1998.

[30] A. S. Konopliv, S. W. Asmar, W. M. Folkner, Ö. Karatekin, D. C. Nunes, S. E. Smrekar, C. F. Yoder, and M. T. Zuber, "Mars high resolution gravity fields from MRO, Mars seasonal gravity, and other dynamical parameters," *Icarus*, vol. 211, no. 1, pp. 401–428, 2011.

[31] J. C. Andrews-Hanna, M. T. Zuber, and W. B. Banerdt, "The Borealis basin and the origin of the martian crustal dichotomy," *Nature*, vol. 453, pp. 1212–1215, June 2008.

[32] M. H. Carr, "Mars Global Surveyor observations of Martian fretted terrain," *Journal of Geophysical Research-Planets*, vol. 106, no. E10, pp. 23571–23593, 2001.

[33] N. K. Forsberg-Taylor, "Crater degradation in the Martian highlands: Morphometric analysis of the Sinus Sabaeus region and simulation modeling suggest fluvial processes," *Journal of Geophysical Research*, vol. 109, no. E5, pp. 1–12, 2004.

[34] M. Carr, *Water on Mars*, vol. 326. Nature, Mar. 1987.

[35] G. E. McGill, "Crustal history of north central Arabia Terra, Mars," *Journal of Geophysical Research-Planets*, vol. 105, no. E3, pp. 6945–6959, 2000.

[36] R. J. Phillips, "Ancient Geodynamics and Global-Scale Hydrology on Mars," *Science*, vol. 291, pp. 2587–2591, Mar. 2001.

[37] F. Nimmo and D. J. Stevenson, "Estimates of Martian crustal thickness from viscous relaxation of topography," *Journal of Geophysical Research-Planets*, vol. 106, no. E3, pp. 5085–5098, 2001.

[38] A. Crosby, "An assessment of the accuracy of admittance and coherence estimates

using synthetic data," *Geophysical Journal International*, vol. 171, no. 1, pp. 25–54, 2007.

[39] D. Mckenzie, "Estimating Tein the presence of internal loads," *Journal of Geophysical Research*, vol. 108, no. B9, pp. 1–21, 2003.

[40] D. W. Forsyth, "Subsurface loading and estimates of the flexural rigidity of continental lithosphere," *Journal of Geophysical Research-Planets*, vol. 90, pp. 12623–12632, Jan. 1985.

[41] D. Mckenzie, D. N. Barnett, and D.-N. Yuan, "The relationship between Martian gravity and topography," *Earth And Planetary Science Letters*, vol. 195, pp. 1–16, Jan. 2002.

[42] M. Grott and D. Breuer, "The evolution of the martian elastic lithosphere and implications for crustal and mantle rheology," *Icarus*, vol. 193, pp. 503–515, Feb. 2008.

[43] T. Hoogenboom and S. Smrekar, "Elastic thickness estimates for the northern lowlands of Mars," *Earth And Planetary Science Letters*, vol. 248, pp. 830–839, Aug. 2006.

[44] T. Watters, "Lithospheric flexure and the origin of the dichotomy boundary on Mars," *Geology*, vol. 31, no. 3, pp. 271–274, 2003.

[45] F. Nimmo, "Admittance estimates of mean crustal thickness and density at the Martian hemispheric dichotomy," *Journal of Geophysical Research-Planets*, vol. 107, no. E11, p. 5117, 2002.

[46] F. Nimmo, "Tectonic consequences of Martian dichotomy modification by lower-crustal flow and erosion," *Geology*, vol. 33, pp. 533–536, July 2005.

[47] T. R. Watters and P. J. McGovern, "Lithospheric flexure and the evolution of the dichotomy boundary on Mars," *Geophysical Research Letters*, vol. 33, no. 8, p. L08S05, 2006.

[48] S. Zhong and M. T. Zuber, "Long-wavelength topographic relaxation for self-gravitating planets and implications for the time-dependent compensation of surface topography," *Journal of Geophysical Research-Planets*, vol. 105, no. E2, pp. 4153–4164, 2000.

[49] E. M. Parmentier, D. L. Turcotte, and K. E. Torrance, "Studies of Finite Amplitude Non-Newtonian Thermal Convection With Application to Convection in the Earth's Mantle," *Journal of Geophysical Research*, vol. 81, no. 11, pp. 1839–1846, 1976.

[50] A. G. W. Cameron and W. R. Ward, "Origin of the Moon," *Lunar and Planetary Institute Science Conference Abstracts*, vol. 7, pp. 120–122, 1976.

[51] A. Cameron, "The Impact Theory for Origin of the Moon," *Origin of the Moon*, 1986.

[52] R. M. Canup and E. Asphaug, "Origin of the moon in a giant impact near the end of the Earth's formation," *Nature*, vol. 412, no. 6848, pp. 708–712, 2001.

[53] R. M. Canup, "Dynamics of Lunar Formation," *Annual review of astronomy and astrophysics*, vol. 42, pp. 441–475, Sept. 2004.

[54] B. L. Jolliff, C. Floss, I. S. McCallum, and J. M. Schwartz, "Geochemistry petrology and cooling history of 141617373 a plutonic lunar sample with textural evidence of granitic-fraction separation by silicate-liquid immiscibility," *American Mineralogist*, vol. 84, pp. 821–837, June 1999.

[55] J. A. Wood, J. S. Dickey, U. B. Marvin, and B. N. Powell, "Lunar Anorthosites," *Science*, vol. 167, pp. 602–604, Jan. 1970.

[56] J. A. Wood, "Thermal history and early magmatism in the Moon," *Icarus*, vol. 16, pp. 229–240, Apr. 1972.

[57] P. Warren, "The magma ocean concept and lunar evolution," *Annual Review of Earth and Planetary Sciences*, 1985.

[58] M. T. Zuber, D. E. Smith, M. M. Watkins, S. W. Asmar, A. S. Konopliv, F. G. Lemoine, H. J. Melosh, G. A. Neumann, R. J. Phillips, S. C. Solomon, M. A. Wieczorek, J. G. Williams, S. J. Goossens, G. Kruizinga, E. Mazarico, R. S. Park, and D.-N. Yuan, "Gravity Field of the Moon from the Gravity Recovery and Interior Laboratory (GRAIL) Mission," *Science*, vol. 339, pp. 668–671, Jan. 2013.

[59] M. A. Wieczorek, G. A. Neumann, F. Nimmo, W. S. Kiefer, G. J. Taylor, H. J. Melosh, R. J. Phillips, S. C. Solomon, J. C. Andrews-Hanna, S. W. Asmar, A. S. Konopliv, F. G. Lemoine, D. E. Smith, M. M. Watkins, J. G. Williams, and M. T. Zuber, "The Crust of the Moon as Seen by GRAIL," *Science*, vol. 339, pp. 671–675, Feb. 2013.

[60] P. C. Hess and E. M. Parmentier, "Thermal evolution of a thicker KREEP liquid layer," *Journal of Geophysical Research-Planets*, vol. 106, pp. 28023–28032, Jan. 2001.

[61] M. A. Wieczorek and R. J. Phillips, "The "Procellarum KREEP Terrane": Implications for mare volcanism and lunar evolution," *Journal of Geophysical Research-Planets*, vol. 105, pp. 20417–20430, Aug. 2000.

[62] P. Lucey, R. L. Korotev, J. J. Gillis, L. A. Taylor, D. Lawrence, B. A. Campbell, R. Elphic, B. Feldman, L. L. Hood, D. Hunten, M. Mendillo, S. Noble, J. J. Papike, R. C. Reedy, S. Lawson, T. Prettyman, O. Gasnault, and S. Maurice, "Understanding the Lunar Surface and Space-Moon Interactions," *Reviews in Mineralogy and Geochemistry*, vol. 60, pp. 83–219, 2006.

[63] K. Pahlevan and D. Stevenson, "Earth and Planetary Science Letters - Chemical fractionation in the silicate vapor atmosphere of the Earth," *Earth And Planetary Science Letters*, vol. 301, pp. 433–443, 2011.

[64] C. Shearer, P. Hess, and M. Wieczorek, "Thermal and magmatic evolution of the moon," *Reviews in Mineralogy and Geochemistry*, 2006.

[65] A. E. Saal, E. H. Hauri, M. L. Cascio, J. A. Van Orman, M. C. Rutherford, and R. F. Cooper, "Volatile content of lunar volcanic glasses and the presence of water in the Moon's interior," *Nature*, vol. 454, pp. 192–195, July 2008.

[66] E. H. Hauri, T. Weinreich, A. E. Saal, M. C. Rutherford, and J. A. Van Orman, "High Pre-Eruptive Water Contents Preserved in Lunar Melt Inclusions," *Science*, vol. 333, pp. 213–215, July 2011.

[67] L. Elkins-Tanton and T. L. Grove, "Water (hydrogen) in the lunar mantle: Results from petrology and magma ocean modeling," *Earth And Planetary Science Letters*, vol. 307, pp. 173–170, 2011.

[68] J. P. Greenwood, S. Itoh, N. Sakamoto, P. Warren, L. Taylor, and H. Yurimoto, "Hydrogen isotope ratios in lunar rocks indicate delivery of cometary water to the Moon," *Nature Geoscience*, vol. 4, pp. 79–82, Jan. 2011.

[69] A. E. Saal, E. H. Hauri, J. A. Van Orman, and M. J. Rutherford, "D/H Ratios of the Lunar Volcanic Glasses," in *Lunar and Planetary Science Conference Proceedings*, p. 2, 2012.

[70] P. H. Warren and J. T. Wasson, "The origin of KREEP," *Reviews of Geophysics*, vol. 17, no. 1, pp. 73–88, 1979.

[71] G. Hirth and D. L. Kohlstedt, "Experimental constraints on the dynamics of the partially molten upper mantle, 2, Deformation in the dislocation creep regime," *Journal of Geophysical Research*, vol. 100, no. B8, pp. 15441–15449, 1995.

[72] G. Neumann, M. Zuber, D. Smith, and F. Lemoine, "The lunar crust: Global structure and signature of major basins," *Journal of Geophysical Research-Planets*, vol. 101, no. E7, pp. 16841–16863, 1996.

[73] L. L. Hood and M. T. Zuber, "Recent Refinements in Geophysical Constraints on Lunar Origin and Evolution," *Origin of the Earth and Moon*, pp. 397–409, 2000.

[74] D. Bercovici and S.-i. Karato, "Whole-mantle convection and the transition-zone water filter," *Nature*, vol. 425, pp. 39–44, Sept. 2003.

[75] J. G. Williams, A. Konopliv, D. Boggs, R. S. Park, D. Yuan, F. G. Lemoine, S. J. Goossens, E. Mazarico, F. Nimmo, R. Weber, S. W. Asmar, H. J. Melosh, G. A. Neumann, R. J. Phillips, D. E. Smith, S. C. Solomon, M. M. Watkins, M. A. Wieczorek, J. Andrews-Hanna, J. W. Head, III, W. S. Kiefer, I. Matsuyama, P. J. McGovern, G. J. Taylor, and M. T. Zuber, "Lunar Interior Properties From the Grail Mission," *Journal of Geophysical Research*, to be submitted.

[76] I. Garrick-Bethell, B. P. Weiss, D. L. Shuster, and J. Buz, "Early Lunar Magnetism," *Science*, vol. 323, pp. 356–359, Jan. 2009.

[77] C. Cournède, J. Gattacceca, and P. Rochette, "Magnetic study of large Apollo samples: Possible evidence for an ancient centered dipolar field on the Moon," *Earth And Planetary Science Letters*, vol. 331-332, pp. 31–42, May 2012.

[78] E. K. Shea, B. P. Weiss, W. S. Cassata, D. L. Shuster, S. M. Tikoo, J. Gattacceca, T. L. Grove, and M. D. Fuller, "A long-lived lunar core dynamo.," *Science*, vol. 335, pp. 453–456, Jan. 2012.

[79] C. Suavet, B. P. Weiss, W. S. Cassata, D. L. Shuster, J. Gattacceca, L. Chan, I. Garrick-Bethell, J. W. Head, T. L. Grove, and M. D. Fuller, "Persistence and origin of the lunar core dynamo," *Proceedings of the National Academy of Sciences*, vol. 110, no. 21, pp. 8453–8458, 2013.

[80] S. K. Runcorn, "The formation of the lunar core," *Geochimica et Cosmochimica Acta*, vol. 60, pp. 1205–1208, Apr. 1996.

[81] D. R. Stegman, A. Jellinek, S. Zatman, J. R. Baumgardner, and M. A. Richards, "An early lunar core dynamo driven by thermochemical mantle convection," *Nature*, vol. 421, no. 9 January 2003, pp. 143–146, 2003.

[82] M. Le Bars, M. A. Wieczorek, Ö. Karatekin, D. Cebron, and M. Laneuville, "An impact-driven dynamo for the early Moon," *Nature*, pp. 215–218, Oct. 2011.

[83] I. S. McCallum and J. M. Schwartz, "Lunar Mg suite: Thermobarometry and petrogenesis of parental magmas," *Journal of Geophysical Research-Planets*, vol. 106, pp. 27969–27983, Jan. 2001.

[84] J. Longhi and L. D. Ashwal, "Two-stage models for lunar and terrestrial anorthosites Petrogenesis without a magma ocean," *Journal of Geophysical Research*, vol. 15, pp. 571–14, Feb. 1985.

[85] D. Kohlstedt, "The Role of Water in High-Temperature Rock Deformation," *Reviews in Mineralogy and Geochemistry*, 2006.

[86] L. Moresi and V. Solomatov, "Numerical investigation of 2D convection with extremely large viscosity variations," *Physics of Fluids*, vol. 7, no. 9, pp. 2154–2162, 1995.

[87] S. Zhong, M. T. Zuber, L. Moresi, and M. Gurnis, "Role of temperature-dependent viscosity and surface plates in spherical shell models of mantle convection," *Journal of Geophysical Research*, vol. 105, no. B5, pp. 11063–11082, 2000.

[88] J. Roberts and S. Zhong, "Plume-induced topography and geoid anomalies and their implications for the Tharsis rise on Mars," *Journal of Geophysical Research*, 2004.

[89] J. H. Roberts and S. Zhong, "Degree-1 convection in the Martian mantle and the origin of the hemispheric dichotomy," *Journal of Geophysical Research*, 2006.

[90] J. Korenaga, "Scaling of stagnantlid convection with Arrhenius rheology and the effects of mantle melting," *Geophysical Journal International*, vol. 179, pp. 154–170, 2009.

[91] S. Zhong, D. A. Yuen, and L.-N. Moresi, "Numerical methods for mantle convection," *Treatise on Geophysics*, vol. 7, pp. 227–252, 2007.

[92] S. Zhong, E. M. Parmentier, and M. T. Zuber, "A dynamic origin for the global asymmetry of lunar mare basalts," *Earth And Planetary Science Letters*, vol. 177, no. 3–4, pp. 131–140, 2000.

[93] W.-S. Yang and J. R. Baumgardner, "A matrix-dependent transfer multigrid method for strongly variable viscosity infinite Prandtl number thermal convection," *Geophysical & Astrophysical Fluid Dynamics*, vol. 92, pp. 151–195, Nov. 2000.

[94] G. Hirth and D. L. Kohlstedt, "Water in the oceanic upper mantle: implications for rheology, melt extraction and the evolution of the lithosphere," *Earth And Planetary Science Letters*, vol. 144, no. 1–2, pp. 93–108, 1996.

[95] S. J. Mackwell, D. L. Kohlstedt, and M. S. Paterson, "The Role of Water in the Deformation of Olivine Single Crystals," *Journal of Geophysical Research*, vol. 90, no. B13, pp. 11319–11,333, 1985.

[96] R. S. Borch and H. W. Green, II, "Deformation of peridotite at high pressure in a new molten salt cell: comparison of traditional and homologous temperature treatments," *Physics of The Earth and Planetary Interiors*, vol. 55, pp. 269–276, June 1989.

[97] U. R. Christensen, V. Holzwarth, and A. Reiners, "Energy flux determines magnetic field strength of planets and stars," *Nature*, vol. 457, pp. 167–169, Jan. 2009.

[98] W. Konrad and T. Spohn, "Thermal history of the Moon: Implications for an early core dynamo and post-accertional magmatism," *Advances in Space Research*, vol. 19, no. 10, pp. 1511–1521, 1997.

[99] J. G. Williams, D. H. Boggs, C. F. Yoder, J. T. Ratcliff, and J. O. Dickey, "Lunar rotational dissipation in solid body and molten core," *Journal of Geophysical Research-Planets*, vol. 106, pp. 27933–27968, Jan. 2001.

[100] C. A. Dwyer, D. J. Stevenson, and F. Nimmo, "A long-lived lunar dynamo driven by continuous mechanical stirring," *Nature*, vol. 479, no. 7372, pp. 212–214, 2011.

[101] M. Fuller and S. M. Cisowski, "Lunar paleomagnetism.," *Geomagnetism*, vol. 2, pp. 307–455, 1987.

[102] S. M. Tikoo, B. P. Weiss, J. Buz, E. A. Lima, E. K. Shea, G. Melo, and T. L. Grove, "Magnetic fidelity of lunar samples and implications for an ancient core dynamo," *Earth And Planetary Science Letters*, vol. 337–338, no. 0, pp. 93–103, 2012.

[103] A. Khan, A. Pommier, and J. A. D. Connolly, "On the Presence of a Titanium-Rich Melt Layer in the Deep Lunar Interior," in *Lunar and Planetary Science Conference Proceedings*, p. 2, 2013.

[104] C. K. Shearer and J. J. Papike, "Basaltic magmatism on the Moon: A perspective from volcanic picritic glass beads," *Geochimica et Cosmochimica Acta*, vol. 57, pp. 4785–4812, 1993.

[105] L. T. Elkins, V. A. Fernandes, J. W. Delano, and T. L. Grove, "Origin of lunar ul-

tramafic green glasses: constraints from phase equilibrium studies," *Geochimica et Cosmochimica Acta*, vol. 64, pp. 2339–2350, July 2000.

[106] R. Weber, P. Lin, E. Garnero, and Q. Williams, "Seismic Detection of the Lunar Core," *Science*, 2011.

[107] D. E. Wilhelms and J. F. McCaulay, *The Geology of the Moon*. US Geol. Surv. Prof, 1987.

[108] S. C. Solomon and J. Longhi, "Magma oceanography. I - Thermal evolution," *Lunar and Planetary Science Conference Proceedings Abstracts*, vol. 8, pp. 583–599, 1977.

[109] S. Solomon, R. Comer, and J. W. Head, "The evolution of impact basins-Viscous relaxation of topographic relief," *Journal of Geophysical Research*, vol. 87, no. B5, pp. 3975–3992, 1982.

[110] K. A. Holsapple, "The Scaling of Impact Processes in Planetary Sciences," *Annual Review of Earth and Planetary Sciences*, vol. 21, pp. 333–373, Jan. 2013.

[111] K. K. Williams and M. T. Zuber, "Measurement and Analysis of Lunar Basin Depths from Clementine Altimetry," *Icarus*, vol. 131, pp. 107–122, Jan. 1998.

[112] E. Pierazzo, A. M. Vickery, and H. J. Melosh, "A Reevaluation of Impact Melt Production," *Icarus*, vol. 127, pp. 408–423, June 1997.

[113] W. S. Kiefer, P. J. McGovern, R. Potter, and G. S. Collins, "The Collapse of Super-Isostasy: The Thermal Evolution of Large Lunar Impact Basins and a Volcanic Intrusion Model for Lunar Mascon Gravity Anomalies," *Lunar and Planetary Science Conference Proceedings Abstracts*, vol. 43, 2012.

[114] W. A. Watters, M. T. Zuber, and B. H. Hager, "Thermal perturbations caused by large impacts and consequences for mantle convection," *Journal of Geophysical Research*, vol. 114, no. E02001, pp. 1–23, 2009.

[115] T. J. Ahrens and J. D. Okeefe, "Equations of state and impact-induced shock-wave attenuation on the moon," *Impact and explosion cratering: Planetary and terrestrial implications; Proceedings of the Symposium on Planetary Cratering Mechanics*, pp. 639–656, 1977.

[116] S. Zhong, A. Paulson, and J. Wahr, "Three-dimensional finite-element modelling of Earth's viscoelastic deformation: effects of lateral variations in lithospheric thickness," *Geophysical Journal of the Royal Astronomical Society*, vol. 155, no. 2, pp. 679–695, 2003.

[117] P. Wu and W. R. Peltier, "Viscous gravitational relaxation," *Geophysical Journal of the Royal Astronomical Society*, vol. 70, no. 2, pp. 435–485, 1982.

[118] S. R. Bratt, S. C. Solomon, and J. W. Head, "The evolution of impact basins: Cooling, subsidence, and thermal stress," *Journal of Geophysical Research-Planets*, vol. 90, pp. 12415–12433, Jan. 1985.

[119] S. C. Solomon and J. W. Head, "Lunar Mascon Basins: Lava filling, tectonics, and evolution of the lithosphere," *Reviews of Geophysics*, vol. 18, no. 1, pp. 107–141, 1980.

[120] E. Parmentier, S. Zhong, and M. T. Zuber, "Gravitational differentiation due to initial chemical stratification: origin of lunar asymmetry by the creep of dense KREEP?," *Earth And Planetary Science Letters*, vol. 201, pp. 473–480, 2002.

[121] F. Tera, D. A. Papanastassiou, and G. J. Wasserburg, "Isotopic evidence for a terminal lunar cataclysm," *Earth And Planetary Science Letters*, vol. 22, no. 1, pp. 1–21, 1974.

[122] B. L. Jolliff, J. J. Gillis, L. A. Haskin, R. L. Korotev, and M. A. Wieczorek, "Major lunar crustal terranes: Surface expressions and crust-mantle origins," *Journal of Geophysical Research-Planets*, vol. 105, pp. 4197–4216, Jan. 2000.

[123] J. W. Head, "Lunar Mare Deposits: Areas, Volumes, Sequence, and Implication for Melting in Source Areas," *LPI Contributions*, vol. 234, p. 66, 1975.

[124] M. R. Cooper, R. L. Kovach, and J. S. Watkins, "Lunar near-surface structure," *Reviews of Geophysics*, vol. 12, no. 3, pp. 291–308, 1974.

[125] V. L. Sharpton and J. W. Head, III, "Stratigraphy and structural evolution of Southern Mare Serenitatis: A reinterpretation based on Apollo Lunar Sounder Experiment data," *Journal of Geophysical Research*, vol. 87, no. B13, p. 10983, 1982.

[126] T. Ono, A. Kumamoto, H. Nakagawa, Y. Yamaguchi, S. Oshigami, A. Yamaji, T. Kobayashi, Y. Kasahara, and H. Oya, "Lunar Radar Sounder Observations of Subsurface Layers Under the Nearside Maria of the Moon," *Science*, vol. 323, pp. 909–912, Feb. 2009.

[127] M. Talwani, G. Thompson, B. Dent, H.-G. Kahle, and S. Buck, "Traverse Gravimeter Experiment," *Apollo 17: Preliminary Science Report*, vol. 330, p. 13, 1973.

[128] C. J. Budney and P. G. Lucey, "Basalt thickness in Mare Humorum: The crater excavation method," *Journal of Geophysical Research*, vol. 103, p. 16855, July 1998.

[129] B. J. Thomson, E. B. Grosfils, D. B. J. Bussey, and P. D. Spudis, "A new technique for estimating the thickness of mare basalts in Imbrium Basin," *Geophysical Research Letters*, vol. 36, p. L12201, June 2009.

[130] R. A. DeHon and J. D. Waskom, "Geologic structure of the eastern mare basins," *Lunar and Planetary Science Conference Proceedings*, vol. 7, pp. 2729–2746, Apr. 1976.

[131] R. A. DeHon, "Thickness of the Western Mare Basalt," *Proceedings of the Lunar and Planetary Science Conference 10th*, pp. 2935–2955, 1979.

[132] F. Hörz, "How thick are lunar mare basalts," *Lunar and Planetary Science Conference Proceedings*, vol. 9, pp. 3311–3331, 1978.

[133] J. W. Head, "Lava flooding of ancient planetary crusts: Geometry, thickness, and volumes of flooded lunar impact basins," *The Moon*, vol. 26, pp. 61–88, Feb. 1982.

[134] H. Hiesinger, J. W. Head, U. Wolf, R. Jaumann, and G. Neukum, "Lunar mare basalt flow units: Thicknesses determined from crater size-frequency distributions," *Geophysical Research Letters*, vol. 29, no. 8, pp. 891–894, 2002.

[135] J. W. Head, III and L. Wilson, "Lunar mare volcanism: Stratigraphy, eruption conditions, and the evolution of secondary crusts," *Geochimica et Cosmochimica Acta*, vol. 56, pp. 2155–2175, June 1992.

[136] J. L. Whitten and J. W. Head, III, "Detecting volcanic resurfacing of heavily cratered terrain: Flooding simulations on the Moon using Lunar Orbiter Laser Altimeter (LOLA) data," *Planetary and Space Science VL*, in press.

[137] A. S. Konopliv, R. S. Park, D.-N. Yuan, S. W. Asmar, M. M. Watkins, J. G. Williams, E. Fahnestock, G. Kruizinga, M. Paik, D. Strekalov, N. Harvey, D. E. Smith, and M. T. Zuber, "The JPL lunar gravity field to spherical harmonic degree 660 from the GRAIL Primary Mission," *Journal of Geophysical Research-Planets*, vol. 118, pp. 1415–1434, July 2013.

[138] F. G. Lemoine, S. Goossens, T. J. Sabaka, J. B. Nicholas, E. Mazarico, D. D. Rowlands, B. D. Loomis, D. S. Chinn, D. S. Caprette, G. A. Neumann, D. E. Smith, and M. T. Zuber, "High-degree gravity models from GRAIL primary mission data," *Journal of Geophysical Research-Planets*, 2013.

[139] D. E. Smith, M. T. Zuber, G. B. Jackson, J. F. Cavanaugh, G. A. Neumann, H. Riris, X. Sun, R. S. Zellar, C. Coltharp, J. Connelly, R. B. Katz, I. Kleyner, P. Liiva, A. Matuszeski, E. M. Mazarico, J. F. McGarry, A.-M. Novo-Gradac, M. N. Ott, C. Peters, L. A. Ramos-Izquierdo, L. Ramsey, D. D. Rowlands, S. Schmidt, V. S. Scott, G. B. Shaw, J. C. Smith, J.-P. Swinski, M. H. Torrence, G. Unger, A. W. Yu, and T. W. Zagwodzki, "The Lunar Orbiter Laser Altimeter Investigation on the Lunar Reconnaissance Orbiter Mission," *Space Science Reviews*, vol. 150, pp. 209–241, May 2009.

[140] D. E. Smith, M. T. Zuber, G. A. Neumann, F. G. Lemoine, E. Mazarico, M. H. Torrence, J. F. McGarry, D. D. Rowlands, J. W. Head, T. H. Duxbury, O. Aharonson, P. G. Lucey, M. S. Robinson, O. S. Barnouin, J. F. Cavanaugh, X. Sun, P. Liiva, D.-d. Mao, J. C. Smith, and A. E. Bartels, "Initial observations from the Lunar Orbiter Laser Altimeter (LOLA)," *Geophysical Research Letters*, vol. 37, no. 18, p. L18204, 2010.

[141] G. Chin, S. Brylow, M. Foote, J. Garvin, J. Kasper, J. Keller, M. Litvak, I. Mitrofanov, D. Paige, K. Raney, M. Robinson, A. Sanin, D. Smith, H. Spence, P. Spudis, S. A. Stern, and M. Zuber, "Lunar Reconnaissance Orbiter Overview: The Instrument Suite and Mission," *Space Science Reviews*, vol. 129, no. 4, pp. 391–419, 2007.

[142] J. C. Andrews-Hanna, S. W. Asmar, J. W. Head, W. S. Kiefer, A. S. Konopliv, F. G. Lemoine, I. Matsuyama, E. Mazarico, P. J. McGovern, H. J. Melosh, G. A.

Neumann, F. Nimmo, R. J. Phillips, D. E. Smith, S. C. Solomon, G. J. Taylor, M. A. Wieczorek, J. G. Williams, and M. T. Zuber, "Ancient Igneous Intrusions and Early Expansion of the Moon Revealed by GRAIL Gravity Gradiometry," *Science*, vol. 339, pp. 675–678, Feb. 2013.

[143] G. B. Reed, "Application of kinematical geodesy for determining the short wave length components of the gravity field by satellite gradiometry.," *Reports of the Department of Geodetic Science, The Ohio State University*, Mar. 1973.

[144] K. Gustafson, "Antieigenvalues," *Linear Algebra and its Applications*, vol. 208-209, pp. 437–454, Sept. 1994.

[145] H. J. Melosh, *Impact Cratering: A Geologic Process*. Oxford Monographs on Geology and Geophysics, Oxford University Press, 1989.

[146] R. J. Pike, "Apparent depth/apparent diameter relation for lunar craters," *Lunar Science Conference Proceedings*, vol. 3, pp. 3427–3436, 1977.

[147] R. J. Pike, "Some Morphologic Systematics of Complex Impact Structures," *Meteoritics*, vol. 20, no. 1, pp. 49–68, 1985.

[148] C. A. Wood and J. W. Head, "Comparison of impact basins on Mercury, Mars and the moon ," *Lunar Science Conference Proceedings*, vol. 3, pp. 3629–3651, 1976.

[149] J. W. Head, C. I. Fassett, S. J. Kadish, D. E. Smith, M. T. Zuber, G. A. Neumann, and E. Mazarico, "Global Distribution of Large Lunar Craters: Implications for Resurfacing and Impactor Populations," *Science*, vol. 329, pp. 1504–1507, Sept. 2010.

[150] W. S. Kiefer, R. J. Macke, D. T. Britt, and A. J. Irving, "Regional Variability in the Density of Lunar Mare Basalts and Implications for Lunar Gravity Modeling," *Lunar and Planetary Science Conference Proceedings Abstracts*, 2012.